# Real-Time Feedback Control
# Of Mixing in a Heated Jet

Y. Ikeda, A. B. Cain*
Phantom Works
The Boeing Company

D. E. Parekh
Aerospace & Transportation Laboratory
Georgia Tech Research Institute

P. Moin
Center for Turbulence Research
Stanford University

J. B. Freund
Department of Mechanical and Aerospace Engineering
University of California, Los Angeles

*Currently with Integrated Application Technologies Co.; Chesterfield, MO

DTIC QUALITY INSPECTED 4

**20001020 025**

# REPORT DOCUMENTATION PAGE

AFRL-SR-BL-TR-00-

0020

| 1. REPORT DATE (DD-MM-YYYY) | 2. REPORT TYPE | 3. DATES COVERED (From - To) |
|---|---|---|
| 30 September 2000 | Final Report | From 15 May 97 to 30 Sep 00 |

| 4. TITLE AND SUBTITLE | |
|---|---|
| Real-Time Feedback Control of Mixing in a Heated Jet | **5a. CONTRACT NUMBER** F49620-97-C-0021 |
| | **5b. GRANT NUMBER** |
| | **5c. PROGRAM ELEMENT NUMBER** |

| 6. AUTHOR(S) | |
|---|---|
| Y. Ikeda, A. B. Cain, D. E. Parekh, P. Moin, and J. B. Freund | **5d. PROJECT NUMBER** |
| | **5e. TASK NUMBER** |
| | **5f. WORK UNIT NUMBER** |

| 7. PERFORMING ORGANIZATION NAME(S) AND ADDRESS(ES) | 8. PERFORMING ORGANIZATION REPORT NUMBER |
|---|---|
| McDonnell Douglas Corporation Wholly-Owned Subsidiary of The Boeing Company P.O. Box 516 St. Louis, MO 63166-0516 | 00P-0069 |

| 9. SPONSORING / MONITORING AGENCY NAME(S) AND ADDRESS(ES) | 10. SPONSOR/MONITOR'S ACRONYM(S) |
|---|---|
| Air Force Office of Scientific Research Directorate of Aerospace and Materials Sciences AFOSR/NA 801 N. Randolph Road Arlington, VA 22203-1977 | |
| | 11. SPONSOR/MONITOR'S REPORT NUMBER(S) |

**12. DISTRIBUTION / AVAILABILITY STATEMENT**
Approved for public release; distribution is unlimited.

**13. SUPPLEMENTARY NOTES**

**14. ABSTRACT**
This report describes work performed to investigate real-time feedback control of mixing in a heated jet and to demonstrate the resulting technique in a laboratory environment. Large-scale direct numerical simulations were performed for jets with various types of actuation and were useful for optimization of the actuators with regard to Strouhal number and amplitude. The integral of the squared velocity and the integral of the concentration were found to be appropriate objective functions for evaluating the performance of a given actuator. In the simulation effort evolution strategies and simulated annealing were used for optimization of the jet actuators. In an experimental study of a jet using a miniature (RAM 750) engine, use of a genetic algorithm showed that it could drive the system to undesirable states during optimization. A classical proportional-integral controller was used to provide real-time feedback control of plume temperature.

**15. SUBJECT TERMS**
Flow control, jets, stochastic optimization of jet control, jet simulations

| 16. SECURITY CLASSIFICATION OF: | | | 17. LIMITATION OF ABSTRACT | 18. NUMBER OF PAGES | 19a. NAME OF RESPONSIBLE PERSON |
|---|---|---|---|---|---|
| **a. REPORT** Unclassified | **b. ABSTRACT** Unclassified | **c. THIS PAGE** Unclassified | UL | 119 | William W. Bower |
| | | | | | **19b. TELEPHONE NUMBER** (include area code) (314) 233-2529 |

Standard Form 298 (Rev. 8-98)
Prescribed by ANSI Std. Z39.18

DTIC QUALITY INSPECTED 4

# Preface

## Table of Contents

# List of Figures

# 1.0 Introduction

Increased mixing is sometimes desired in aircraft jet exhaust to disperse hot gases quickly. Similarly, in combustors enhanced mixing increases the net reaction rate and thereby combustor efficiency. The primary objectives of this program were to investigate methods for open-loop optimization and real-time feedback control of mixing in a heated jet and to demonstrate the resulting techniques in a laboratory environment. The techniques developed in this program are applicable, for example, to C-17 plume temperature reduction. The approach to achieving the program objective has involved systems modeling, control law design, and control law implementation in a real-time laboratory-scale jet.

The systems modeling involved various levels of sophistication ranging from large-scale direct numerical simulations, which are described in Section 2.0, to an inviscid linear stability approach, which is described in Section 3.0. The direct numerical jet simulations, which accounted for effects of fluidic actuators, were used to predict the flow dynamics with various types of forcing. The mixing effectiveness was determined using potential core length and scalar concentration as metrics. The direct simulations were also used in combination with optimization methods to find the optimal actuation. In an attempt to develop a jet model which captures the relevant physics but has sufficient simplicity to provide realistic state estimates, a linear stability model of the jet was formulated. This approach used a stability scheme with a piecewise quadratic base flow for obtaining the eigenvalues that provide the instability development leading to the turbulent breakdown of the jet. It was found, however, that the computational effort for this approach made it unmanageable as a state model in a feedback control setting.

Consequently, a baseline controller was formulated in the present work by using an experimental database for a jet with pulsed excitation. Various controller design methods were evaluated which could provide the control logic for the jet mixing. These included a weak solution of the linearized flow equations with a forcing term, a linearized system model determined by the input-output relationship of the flow system, and a nonlinear inverse system model. The latter was used to construct the baseline controller and, to compensate the inversion error, an integrator was used in the feedback path. The resulting control design, which is described in Section 4.0, was delivered to GTRI for laboratory demonstration.

The laboratory implementation of the controller summarized in Section 5.0 was focused on pulsing air into the jet exhaust stream to reduce the temperature by increasing mixing of the exhaust with ambient air. The miniature engine used in the experiments (a RAM 750 manufactured by R.A. Microjets) was a single stage axial turbine and is capable of producing approximately 20 lbs. of thrust. Two actuators located at the jet exit pulsed air into the exhaust stream and could achieve frequencies up to 1200 Hz at flow rates up to 10% of the jet engine flow rate. This approach provided the important capability of simultaneously achieving both high frequency and high flow rate in a compact system. Exhaust temperature was measured at the immediate jet exit as well as downstream of the exit with a movable aspirated thermocouple. The downstream

1

centerline temperature was used as a figure of merit for the mixing and provided the single input to the controller.

In the GTRI laboratory demonstration, all data acquisition and control were performed with a personal computer using the Lab View software package. The control systems consisted of the jet engine throttle and the actuator pulsing frequency, while the measurement systems consisted of mass flow to the actuators, jet exhaust velocity, and jet exhaust temperature. Work with the Boeing-supplied control algorithm, which was based on data from a generic axisymmetric round jet, revealed that it could not be ported directly to a jet engine which has both a centerbody and some residual swirl. However, an experimental database for the jet exhaust from the RAM 750 did provide the relation between centerline temperature and actuation frequency which allowed a classical proportional-integral controller to regulate the plume temperature. This work is described in Section 5.0. In addition, an alternate approach was adopted in which a genetic algorithm was implemented to provide an automated means for optimizing actuator forcing frequency and amplitude. It was found that this technique could drive the system to undesirable states during optimization. This approach is also described in Section 5.0. Conclusions based on the overall program effort are contained in Section 6.0

# 2.0 Direct Simulation of Turbulent Jet Mixing

Numerical simulations have been used to study the dynamics of jets subject to different types of forcing and to develop tools for their optimization. The work was divided in three parts: First, direct numerical simulations of forced jets were conducted to provide a database for the identification of suitable measures/control laws for jet mixing. Then numerical simulations were combined with an optimization procedure to search for the optimal actuation with respect to jet mixing. Finally, this procedure was applied to the optimization of jet mixing at higher Reynolds number using large eddy simulation of the flow.

Large-scale direct numerical simulations of jets forced with different types of actuation were conducted to perform a detailed analysis of their dynamics. The compressible Navier-Stokes equations were solved without modeling approximations. Fluidic actuators were included in the computation by adding specially designed body force terms to the governing equations. By taking this novel approach we avoided the computational cost that would have been required to represent the actuators in detail but still were able to provide a high-amplitude, low mass flux forcing that was similar to that used in corresponding experiments. Two slot jet actuators were positioned just down stream of the nozzle, each spanning 90 degrees of the jet's circumference and blowing normal to shear layer. They were operated 180 degrees out of phase to excite flapping modes in the jet. When activated, the actuators mass flux was 3.5 percent of the jet's mass flux and the peak actuator velocity was 60 percent of the jet velocity. Details of the numerical method and the incorporation of the fluidic actuators are given in Appendix A. Three cases were simulated: one was not forced in order to provide a point of comparison while the two others were forced at Strouhal numbers $St = fD/U = 0.2$ and $St = 0.4$. In the experiments of Parekh et al. (1996), $St = 0.2$ was found to be most effective at reducing the potential core length and was picked here for that reason; $St = 0.4$ was found to be the most amplified frequency in the unforced jet. All three jets are visualized with contours of vorticity magnitude in Figure 2-1. Forcing at $St = 0.2$ excited a large a large-scale flapping of the entire jet column (Figure 2-1b) as observed in the experiments of Parekh et al. When forced at $St = 0.4$, the jet responded more rapidly and large turbulent structures appeared closer to the nozzle (Figure 2-1c). However, these instabilities appear to saturate before the end of the potential core and the overall effect on the jet was less pronounced than when it was forced at $St = 0.2$.

Several measures of mixing effectiveness were investigated. Potential core length measurements and scalar concentrations both showed that forcing at either Strouhal number dramatically increased mixing. The streamwise mass flux was significantly increased for the forced cases, with $St = 0.2$ forcing inducing marginally more entrainment than $St = 0.4$ forcing. Aside from the potential core length difference, the most dramatic difference found between the two forced cases was in the scalar dissipation and in the integral of the squared radial velocity in the jet. It was found that the single period average of the measures is very close to its longtime average, which is important for the application of these control techniques. For a detailed discussion of the jet dynamics and the various measures for jet mixing see Appendix B.

3
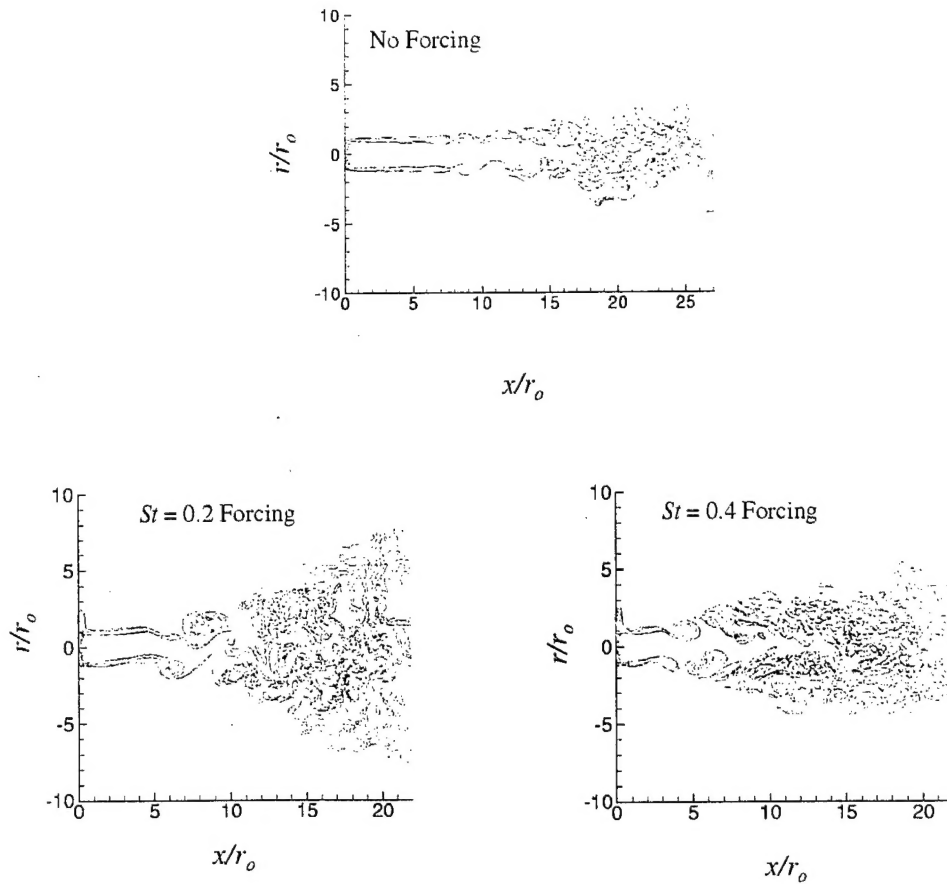
**Figure 2-1. Vorticity magnitude contours for different cases. Twenty evenly space contours between $\omega r_o / U_j = 0.6$ and 12.0 are shown.**

In the second step, the simulations were combined with optimization strategies to automatically search for the optimal actuation. Testing various optimization procedures it was found that evolution strategies are suitable for the optimization of this computationally expensive problem. Starting from a set of initial parameter vectors which contains the Strouhal numbers and amplitudes of the actuation $x = (St_a, St_h, A_a, A_h)$, new vectors were obtained by random variation. An initial population of parameter vectors is subjected to repeated mutation and selection until a sufficiently good solution is found. The advantage of evolution programs is that they are efficient, ensuring a rapid convergence of the procedure by evaluating several search trajectories in parallel. Our approach for optimizing jet mixing requires 100 – 200 numerical simulations of the jet. In order to reduce the CPU time, we made use of the observation that the jet is sensitive to the external forcing already at early stages of the simulation. Since the flow is governed by the dynamics of the large-scale structures, a coarse grid was used for the evaluation of the objective function (Appendix C).

For the test case of an incompressible jet flow at low Reynolds number $Re = 1500$, a systematic search was performed for helical and combined axial and helical forcing of the jet. The direct numerical simulation used a second order finite volume method to solve the incompressible Navier-Stokes equations on a staggered spherical grid. The actuation was imposed on the velocity profile at the inflow. A spherical coordinate system was used which is able to follow the streamwise spreading of the jet and allows a well-balanced resolution of the flow field with a reasonable number of grid points. An important result is that combined axial and helical actuation is much more efficient with respect to jet mixing than a helical actuation alone. The combined actuation leads to a large spreading of the jet, resulting in a large mixture fraction and a fast decay of the center line velocity and scalar concentration. We found the most pronounced spreading when the helical Strouhal was $St_h \approx 0.3$, which is close to the preferred Strouhal number of the jet, and for an axial Strouhal number $St_a \approx 2 \cdot St_h$. This is in very good agreement with experimental results (Parekh et al (1996)). Figure 2-2 shows a snapshot of the scalar concentration of the jet obtained for the optimal actuation found by the evolution strategy. This dual-frequency actuation leads to a large spreading. The jet column is completely dispersed near the end of the domain, indicating good mixing of the jet with the ambient fluid. In Figure 2-3 we show the centerline velocity obtained from the flapping and bifurcating jet computations. For comparison the profile for a round axisymmetric jet (standard jet) at comparable Reynolds number is included. For both the flapping and bifurcating jets the centerline starts to drop much earlier than in the standard jet. The decay rate (slope of the curve in Figure 2-3 (right)) of the flapping jet is comparable to that of the standard jet while the bifurcating jet decays much faster. For the flapping jet the decay is approximately linear, for the bifurcating jet superlinear. A description of the best actuation found for different types of forcing and the resulting jet flows is given in Appendix C.
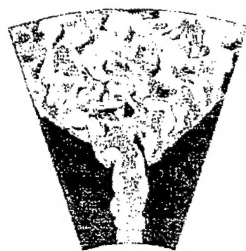


**Figure 2-2. Snapshot of the scalar concentration for a jet actuated with dual-frequency forcing and $St_a = 0.66$, $St_h = 0.31$, $A_a = 0.025$, $A_h = 0.075$.**
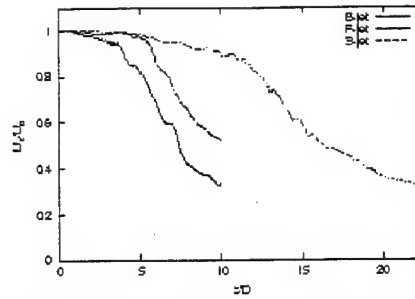
**Figure 2-3.** The averaged centerline scalar concentration for the flapping, bifurcating and standard jets, $Re = 1500$.

Finally, the optimization procedure was applied to jets at higher Reynolds *number Re = 6000* using a large eddy simulation. Including the dynamics procedure to model the small scales of the flow, the optimization procedure was used to search for the optimal actuation. Although the large eddy simulation of the jet is computationally expensive, we were able to find good solutions within reasonable time. Figure 2-4 shows a snapshot of the jet with the best mixing properties obtained for combined axial and helical actuation. The actuation leads to a large scale flapping of the jet column and a spreading rate, which is higher than that for flows at lower Reynolds numbers.



**Figure 2-4.** Snapshot of the scalar concentration for a jet at $Re = 6000$, $St_a = 0.79$, $St_h = 0.36$, $A_a = 0.025$ and $A_h = 0.075$.

In conclusion, a detailed study of forced jets was performed. Fluidic actuators were introduced that realistically model those used in experiments, and a tool was developed for the optimization of the actuation. The measures for mixing that were identified by the simulations proved to be suitable for jet flows subject to different types of actuation and are promising candidates for incorporation in a controller.

# 3.0 Eigenmode Modeling of Jet Flows

To design feedback control algorithms, it is very useful to have a simple model that accurately captures the relevant physics of turbulent jet flows. Such a model is developed in the present work using linear stability theory to model the initial development of the instabilities leading to the turbulent breakdown of a jet. A key feature of the present work is a piecewise quadratic approximation of the mean flow that permits rapid solution of the equations. The stability equations were derived by Alexander Pal in the present contract work, and their formulation is presented in Appendix D.

It is well established that the inviscid inflectional instability characterized by Kelvin and Helmholtz dominates the large-scale development of inflectionally-dominated flows even into non-linear turbulent regimes. An excellent review discussing many important aspects of this problem is given by Ho and Huerre (1984). Supporting articles covering other aspects of the problem (including the nature of nonlinear interaction and wall effects) are described in Cain and Thompson (1986) and Cain, Roos and Kegelmen (1990). The dominance of the inviscid inflectional instability in the present flow motivates the use of the incompressible inviscid stability equations as the system model.

A comparison between the prediction of linear theory and the nonlinear evolution of the jet shear layers is given by Morris et al. (1990) and Viswanathan and Morris (1992) for planar and round jets, respectively. These works derive systems comprised of parabolic equations for the mean flow development that depend upon the local instability eigenproblem for the forcing. Solution of this eigensystem is generally the most computationally-intensive aspect of generating the solution to the evolution model for the jet. The need for very rapid solutions for real-time systems modeling motivates the new approach to approximate solution of the disturbance eigenvalue problem.

Motivated by the need for rapid evaluation, piecewise linear and quadratic approximations of the velocity profiles are used to simplify the inviscid linear disturbance equations. In addition, mathematical solutions are somewhat easier to obtain for the temporal evolution problem. All the work described here will use the temporal analysis combined with Gaster's relation to approximate the behavior of the spatially evolving problem. The approach so describing an inflectionally dominated flow is given by Drazen and Reid (1981). A few examples of the piecewise linear analysis for planar flows will be presented before describing a piecewise quadratic approximation that will be used as an approximation in the round jet geometry.

## 3.1 The piecewise linear approximation for planar geometries

The simplest example of the piecewise linear approach is a three-segment representation of the plane shear layer. This approach has been shown to provide consistent and reasonable characterization of the stability behavior of this flow, and it

compares well with a more accurate (but more time consuming) analysis with a hyperbolic tangent representation of the mean velocity profile. The characterization of
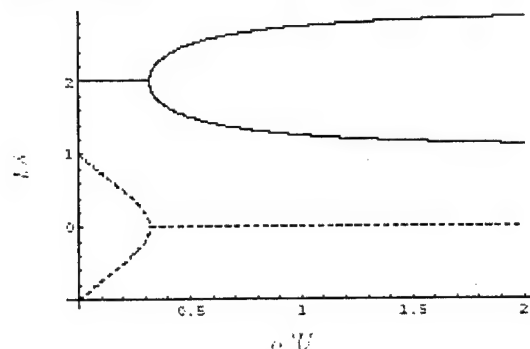


**Figure 3-1. Phase speed ____ and growth rate ----- for piecewise linear planar shear layer.**

the disturbances is given by the exponential coefficient for temporal disturbance growth rate and phase speed and is a function of the disturbance wavenumber. As shown in Figure 3-1, the phase speed computed using such an approach varies from $U$ to $3U$, where $U$ is the velocity of the slow stream. The complex wave speed comes as complex conjugate pairs, and the actual phase velocity is the mean of the two branches plotted. The imaginary part of the wave speed (which in product with the wavenumber gives the exponential grown rate) vanishes at a wavenumber slightly greater than 0.3.

The next piecewise linear flow considered is the planar jet. Figure 3-2 shows the Gaster transformed and scaled spatial growth rate and phase speed versus wavenumber for the sinuous mode of a planar jet having a potential core of 18 jet radii ($r_o$) long, a shear layer of 1 unit width, and a freestream velocity equal to 1/3 of the jet velocity $1.5U_a$, where $U_a$ is the average of the jet and co-flow velocities. Note that in this case the long wavelength (low wavenumber) disturbances have a phase speed of the freestream speed while shorter disturbances have a phase speed of the mean shear layer speed. Figure 3-3 shows the behavior of the varicose mode. Note that the varicose mode has a phase speed equal to that of the jet centerline for long wavelength disturbances and the same phase speed as the sinuous mode for shorter wavelength disturbances. When the shear layers are thin and separated by a large region of potential flow, the stability of the planar jet is nearly the same as that of the planar shear layer except at very long wave lengths. At smaller separation, disturbances of the two shear layers exhibit a strong coupling. These behaviors for both the varicose and the sinuous modes are characteristic of the actual physical system.
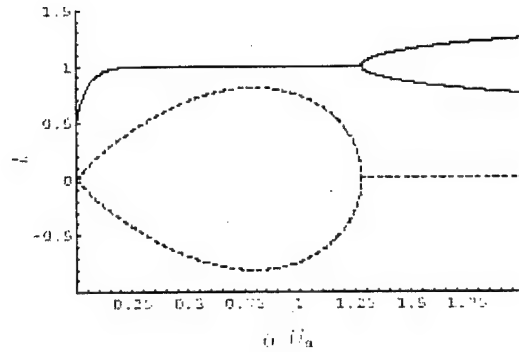
**Figure 3-2. Phase speed ____ and growth rate ----- of a sinuous mode in a piecewise linear planar jet.**
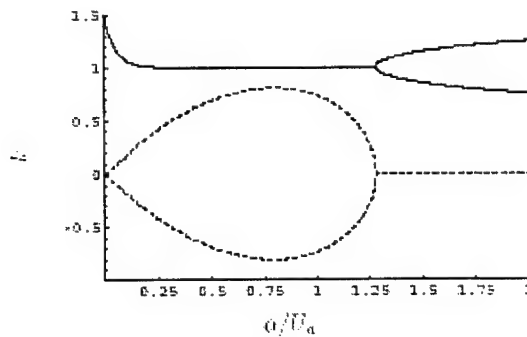


**Figure 3-3. Phase speed ____ and growth rate ----- of a varicose mode in a piecewise linear planar jet.**

## 3.2 The piecewise quadratic approximation for cylindrical geometries

A piecewise representation of the mean velocity profile simplifies the round jet stability problem to Bessel's equation. The solutions are constrained by requiring finite levels in the inner potential region and solutions that vanish at infinity in the outer potential region. These inner and outer solutions (in terms of Bessel functions) are coupled by matching conditions. The matching is achieved by a combination of the inner and outer Bessel solutions (a linear combination of Bessel functions is a valid solution within the finite thickness shear layer). This problem was formulated by Alexander Pal under the present contract work with the derivation of the governing equations given in Appendix D. In the present work the complex-valued quadratic dispersion relation was solved using Mathematica (Cain, et al. (1998)).

The behavior of the axisymmetric disturbances for a round jet with a potential core diameter of $18r_o$ and jet velocity $U_j$ with zero free stream velocity is given in Figure 3-4. Note that the appropriately scaled growth rate and phase speed behave in a manner which is qualitatively similar to the varicose mode of the analogous planar jet.

9
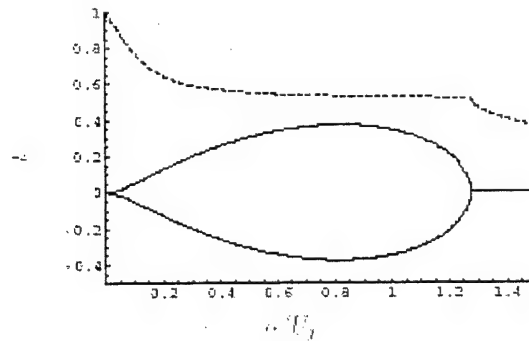
**Figure 3-4. Phase speed ---- and growth rate ____ of a varicose mode in a piecewise linear planar jet.**

The formulation of Viswanathan and Morris (1992) was implemented using the piecewise quadratic stability formulation. An example of the predicted evolution of the shear layer edges using only the $n = 0$ axisymmetric disturbance is shown in Figure 3-5. Figure 3-6 shows the locally dominant wavenumber versus downstream distance in jet radii. It is assumed that, when a disturbances saturates (due to the thickening of the shear layer), the sub-harmonic will become dominant and evolve until saturation, and so on. The results shown in Figures 3-5 and 3-6 are for an initial shear layer thickness of 1% of the jet radius, with the n = +1 and n = -1 modes assumed to grow at the same rate as the n = 0 modes.
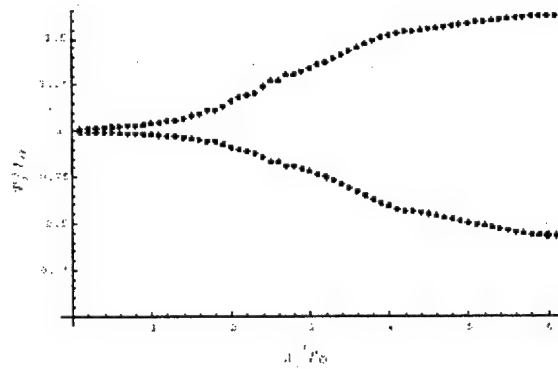


**Figure 3-5. Inner and outer shear layer edges**

10
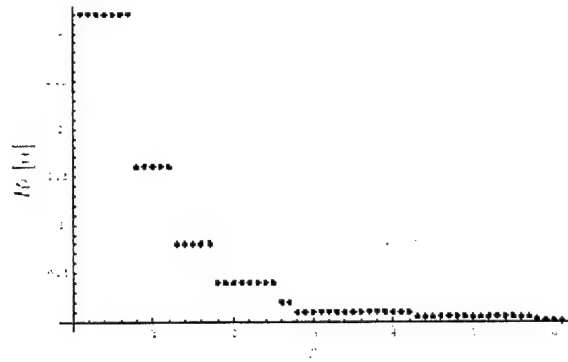
**Figure 3-6. Locally dominant instability wave number.**

In conclusion, an approximate analytic solution to the appropriate linear stability problem, and the role of this solution in the evolution of the round jet, has been investigated. The use of such a model as a state estimator in a feedback control framework must include at least the $n = \pm 1$ modes in addition to the $n = 0$ mode given here. In the case of a thin shear layer, the $n = \pm 1$ modes behave similarly to the $n = 0$ mode and may be analyzed with the $n = 0$ analysis. However, the solution for $n = \pm 1$ is required as the shear layer thickness becomes significant relative to the jet radius. For the mixing problem it is likely that the solution near the end of the potential core will be need to be calculated. After further study it was concluded that even the linear stability analysis approach was not manageable as a state model in a feedback control setting.

# 4.0 Control via Classical System Identification

The controller design objective was to construct a controller that regulates the local temperature at a specified downstream location using a fluidic actuator. For the technique to be implemented in an aircraft, the controller needs to operate in real time. During the course of this program several different controller design methods were investigated which are based on 1) a weak solution of the linearized flow equations with a forcing term (Abergel and Temam, 1990), 2) a linearized system model determined by the input-output relationship of the flow system (Ikeda, 1998), and 3) a nonlinear inverse system model.

In order to keep the computational requirements small enough to accommodate the real-time operation, the first and second methods use a linearly approximate model in spite of the fact that the actual physical flow is highly nonlinear. The third method also uses the input-output relationship of the flow, but the nonlinear inverse design method is used instead of linearization of the model. The resulting controller based on this approach does not require intense computational effort in control update. Therefore, the nonlinear inverse system model was adopted to construct the baseline controller for the laboratory implementation and demonstration.

The general description of the inverse design method can be summarized as follows:

Consider the system given by the first order ordinary differential equation $\dot{x} = f(t, x, u)$, where $x$, $u$, $t$, respectively denote the state to be controlled, admissible control, and time. For each $t$ and $x$, $f$ is assumed to be a smooth one-to-one function (at least of Class $C^1$) in $u$. Let $w$ be the right hand side of the above differential equation. That is, $w = f(t,x,u)$.

Then $u$ can be written as $u = f^{-1}(t,x,w)$.

For the sake of discussion, it is assumed that this inversion is realized perfectly, i.e., no approximation and/or rounding errors are involved. Then by linear optimal control theory, one can construct a proportional controller gain $K_p$ such that the error between the command input and the feedback states decays exponentially in time. Hence, the system can be regulated. This can be seen as follows: let $\varepsilon(t)$ be the error process given by

$$\varepsilon(t) = x(t) - x_{cmd}(t).$$

Then by referring to the diagram in Figure 4-1,

$$\dot{\varepsilon}(t) + K_p \varepsilon(t) = u(t).$$

By solving the above differential equation,

$$\varepsilon(t) = e^{-K_{p}t}\varepsilon(0) + \int_0^t e^{-K_p\sigma} u(t-\sigma)d\sigma .$$

From this it follows that the states can be driven to the desired level by a positive gain $K_p$ and the bounded input.
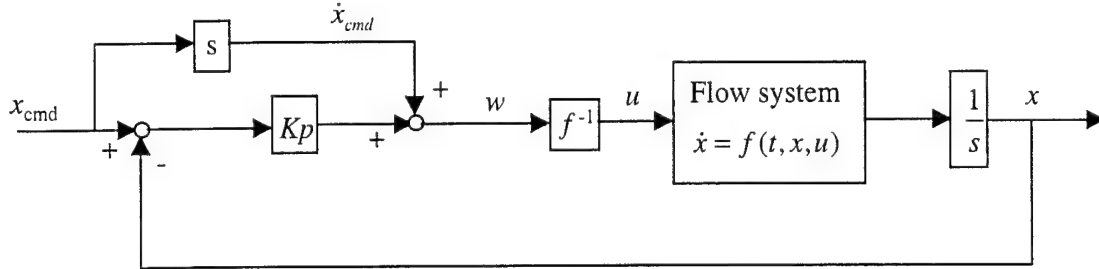


**Figure 4-1. Control structure for the inverse design method.**

In reality, however, the inversion errors must be taken into account. That is, $u = \hat{f}^{-1}(t,x,w) = f^{-1}(t,x,w) + \Delta u$, and an additional element is needed in the block diagram for error correction. This error correction can be done by a number of ways (for example, a neural-network-based on-line learning algorithm or a simple integrator).

A controller implementation strategy was then formulated. A baseline controller was designed using an experimental database for pulsed-jet excitation. In order to make the resulting controller applicable to the RAM 750 miniature engine tested at GTRI, a normalized temperature T* defined by the following relation was used:

$$T^* = \frac{t - t_\infty}{t_0 - t_\infty}, \text{ where}$$

$t_0$ : temperature at the nozzle exit

$t_\infty$ : ambient temperature

$t$ : temperature to be controlled

The baseline controller was constructed by the inverse system identification method, and an integrator was used in the feedback path to compensate the inversion error. The resulting control architecture is illustrated in Figure 4-2.

13
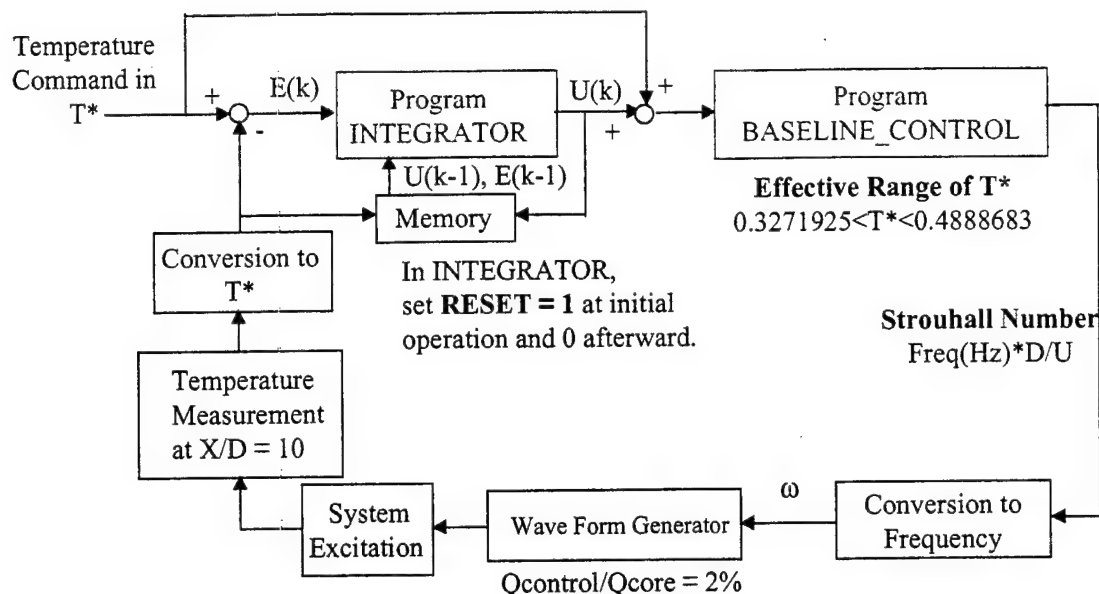
**Figure 4-2. Control architecture for active flow control of jet temperature.**

It should be noted that in the general discussion on the control structure, the system inversion model was described by a first-order differential equation. However, the actual baseline controller was designed by a zeroth order inverse system model (i.e., continuous but not differential form). The resulting control design logic was coded in FORTRAN and delivered to GTRI for laboratory evaluation. It was found in the experimental demonstration that the curve fit for the excitation frequency was not sufficiently general to describe the exhaust flow for the RAM 750 miniature engine. Consequently it was decided to explore other techniques such as evolutionary strategies as a means for controlling the temperature in the jet.

14

# 5.0 Parameter Optimization via Evolutionary Strategies

In this work we employ a new optimization strategy for the control of flows based on a class of algorithms from the discipline of "soft computing." Specifically, we consider the application of evolutionary strategies for optimization in both a simulation environment and a real-time physical experiment. The broad class of evolutionary strategies, of which genetic algorithms are a part, differ from traditional gradient search techniques in that they do not assume any knowledge of the derivatives of the function being optimized. Instead, the optimal (based on a set of preferred metrics) value of a function is obtained by a random natural selection from the available sample set of independent variables. In this application, the independent variables include actuator number, placement, frequency, phasing, and amplitude. The objective of the search in this case is to select the set of actuator parameters that maximizes the jet mixing as indicated by plume downstream temperature or velocity. From iteration to iteration (or generation to generation) a new set of parameters is selected based on a random selection process, and the value of the function for each of those parameters is compared against the function values corresponding to a previous set of parameters. The parameters that provide more optimal function values survive and are the basis for selection of a new set of parameters. Algorithms for defining the population of independent variables that form each generation can be as simple as one member per generation to numerous members that mutate and propagate a new generation of members.

The specific search strategy that we employ is a simple $1 + 1$ strategy in which only two function evaluations at a time are compared to determine the better parameter set. The initial evaluation of each set is referred to as the 'parent' and the successive evaluation as the 'child'. The specific algorithm for selection of the next parameter set for function evaluation is illustrated in Figure 5-1. This is akin to simulated annealing except that instead of using a Boltzmann distribution as the basis for the selection of successive generations, we employ a restart process after a finite number of iterations to assure that the optimization is not trapped in a local minimum.

## Algorithm

Evaluate $f(x^n)$

Evaluate $f(x^*)$,

$x^* = x^n + N(o, \sigma)$

If $f(x^n) < f(x^*)$ then

   $x^{n+1} = x^n$

else $x^{n+1} = x^*$

Vary $\sigma$ by 1/5-rule



Constraint on parameter range

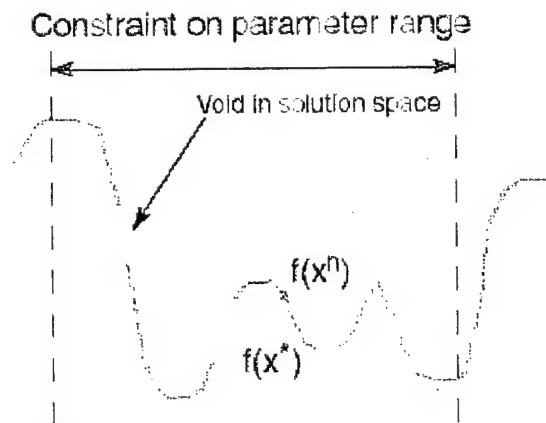Void in solution space

$f(x^n)$

$f(x^*)$

**Figure 5-1. Selection strategy for genetic algorithm.**

This approach was used successfully as a wrapper around numerical simulations for optimizing flow control parameters and is robust enough to handle various types of constraints on the parameter search space. The notion of a "wrapper" is simply that the genetic algorithm is used to select the next set of actuation parameters to be evaluated through a numerical simulation or experiment. In one case, we used this technique to select the optimal set of frequencies for maximizing jet mixing with a DNS simulation as our test bed and in the other, we focused on maximizing the spreading of a bifurcating jet by optimal selection of excitation frequency, frequency ratio, and phase with a vortex method simulation (Koumoutsakos, Freund, and Parekh, 1998, included for reference in Appendix E).

In the DNS simulation, the evolutionary algorithm varied the frequency, phase, and amplitude of three linearly combined sinusoidal excitation signals. The variation of these parameters was only constrained to a specified maximum energy for the combined signal. This avoided the trivial outcome of simply increasing the amplitude of all three signals without bound. While the initial guess distributed energy nominally equally among three separate signals, the optimized set of signals distributed almost all the energy into only one frequency, a Strouhal number around 0.2, which is very close to the optimal value found in previous experiments (see Parekh *et al.*, 1996).

In the vortex simulations, the algorithm was able to "discover" a flow state not previously observed. The bifurcating jet has a Y-shaped structure in which successive vortex rings propagate on alternate trajectories forming two branches. The angle separating those two branches is indicative of the degree of jet spreading. We expected the algorithm to select an optimal set of parameters that maximized that spreading angle but with no change to the general structure of the jet. Instead, the algorithm converged on a set of parameters that produced a bifurcating jet with a secondary bifurcation resulting in much greater spreading angles.

These two cases are illustrative of the utility of this optimization strategy both in optimizing flow development without *a priori* knowledge about the flow and in discovering new phenomenon that might easily be missed even by systematic searches through the parameter space. The following example of real-time optimization of a small-scale jet engine illustrates the utility of this approach in the presence of noise and process variability.

The laboratory demonstration involved the use of pulsed fluidic actuators at the engine nozzle exit plane for plume mixing enhancement. The miniature engine used in the experiments is a RAM 750 manufactured by R.A. Microjets. It has a single-stage centrifugal compressor and a single-stage axial turbine. It is capable of producing approximately 20 lbs. of thrust and high subsonic exhaust flows at temperatures over 700° C. Both the engine and actuator were operated under computer control with the genetic algorithm controlling in real time the frequency of the actuator based on temperature measured in the plume. Figure 5-2 shows the engine installed on the test stand with the compact actuators on opposite sides of the nozzle. The "amplitude" of the excitation was set by controlling the flow rate through the actuator.

16

Three factors contributed to the jet characteristics differing significantly from those observed in generic jet flows from axisymmetric laboratory nozzles with top-hat exit velocity profiles. First, the presence of the centerbody results in a jet exhaust that decays much more rapidly than one would expect from simply scaling generic jet data based on the engine nozzle diameter. Second, being a hobby class engine, the engine is not designed to produce uniform non-swirling flow from the exit, and the engine speed control tolerance is only good to a few percent due to it susceptibility to EMI. Additionally, in these flow control experiments, one of the actuators was turned off to simulate a failure mode. While these factors are undesirable in a canonical flow experiment, they are ideal for evaluating the general robustness of the optimization technique in the presence of realistic complexities and noise sources.
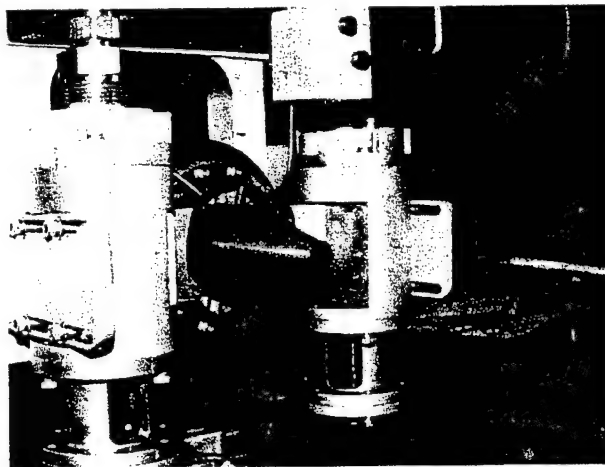


**Figure 5-2. GTRI laboratory configuration using the RAM 750 miniature engine for demonstration of turbulent jet mixing control.**

A typical experimental result is shown in Figure 5-3. Starting with a random initial guess for excitation frequency (represented nondimensionally by Strouhal number = frequency x nozzle diameter / exit velocity), the algorithm determines the next guess by random selection. The random distribution governing the "rolling of the dice" is a uniform distribution of fixed width centered about the previous guess. The function evaluation consists of measuring a short-time (up to 2 seconds) average centerline temperature at a streamwise location 4 diameters downstream of the jet exit. Whichever frequency ('parent' or 'child') corresponds to a lower temperature is selected as the 'parent' for the next iteration or 'generation'. Every ten iterations, the width of the random distribution for parameter selection is either increased or decreased based on the 1/5-rule noted above. The history of variations in terms of specified excitation frequency and the corresponding measured temperature (shown nondimensionally as the difference between measured and ambient temperature divided by the difference between jet exit and ambient temperatures) for a single experiment is shown in Figure 5-3 as a function of iteration number. The algorithm is able within a few iterations to get very close to the optimal value. As the optimization converges toward an optimal value, the width of the random distribution is automatically scaled down as is evident from the reduced

17

variations in the "child" Strouhal numbers at the latter iterations. The expected convergence value of 0.10 is different from the 0.12 value to which the algorithm converged because of the normal variability of the engine plume characteristics from run to run. This illustrates the naturally adaptive nature of the technique. Appendix F provides additional data regarding the base state and additional optimization experiments.

Genetic Algorithm Convergence (Ma = 0.15, 5% MFR, 10 Generations/cycle)
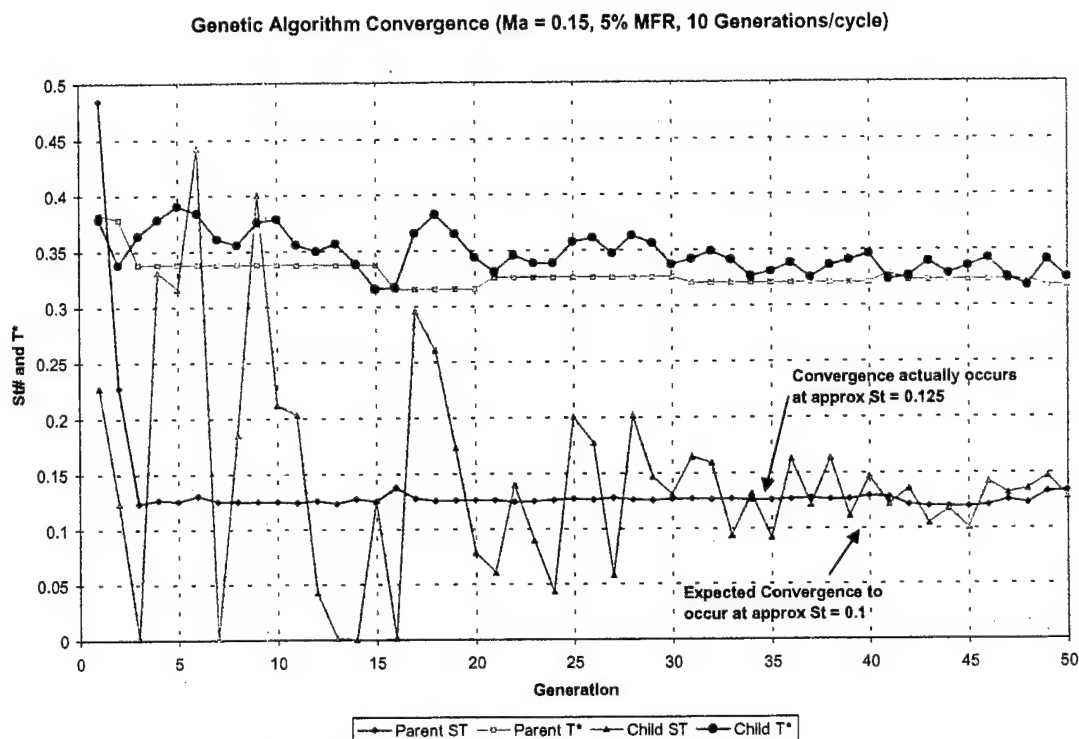


**Figure 5-3. Convergence of excitation frequency.**

The final demonstration conducted in this program involved implementing the classical control technique described in the previous section. Since the engine performance was so different from the generic axisymmetric jet used to develop the state model in the previous section, a new empirical model was derived by fitting a high-order polynomial to the data obtained on the small-scale engine (see Appendix F). This model provided an analytical approximation of the relationship between engine plume centerline temperature and the forcing frequency for a given actuator mass flow rate. Using a classical proportional-integral controller, we were able to demonstrate real-time feedback control of plume temperature. Figure 5-4 shows the performance of this controller for two values of relative gain of the integral component. During this experiment, the commanded temperature was changed at the 100th iteration of the control loop. The objective of this particular demonstration was to show how real-time feedback control could be effected with even a very simple classical control approach. Greater performance could certainly be achieved through optimization or use of more sophisticated control approaches. However, implementation on legacy systems or affordability constraints often make simpler approaches more attractive even with some sacrifice in performance.

18

When real-time feedback control is required to track commanded temperatures, the genetic algorithms are probably not appropriate since they could drive the system to undesirable states during the optimization. A better role for them would be the optimization of the gains and other parameters of a more classical feedback control technique.

**Closed Loop Temperature Control for Two Values of Integrator Gain**
**(Ma = 0.16, 5% MFR)**
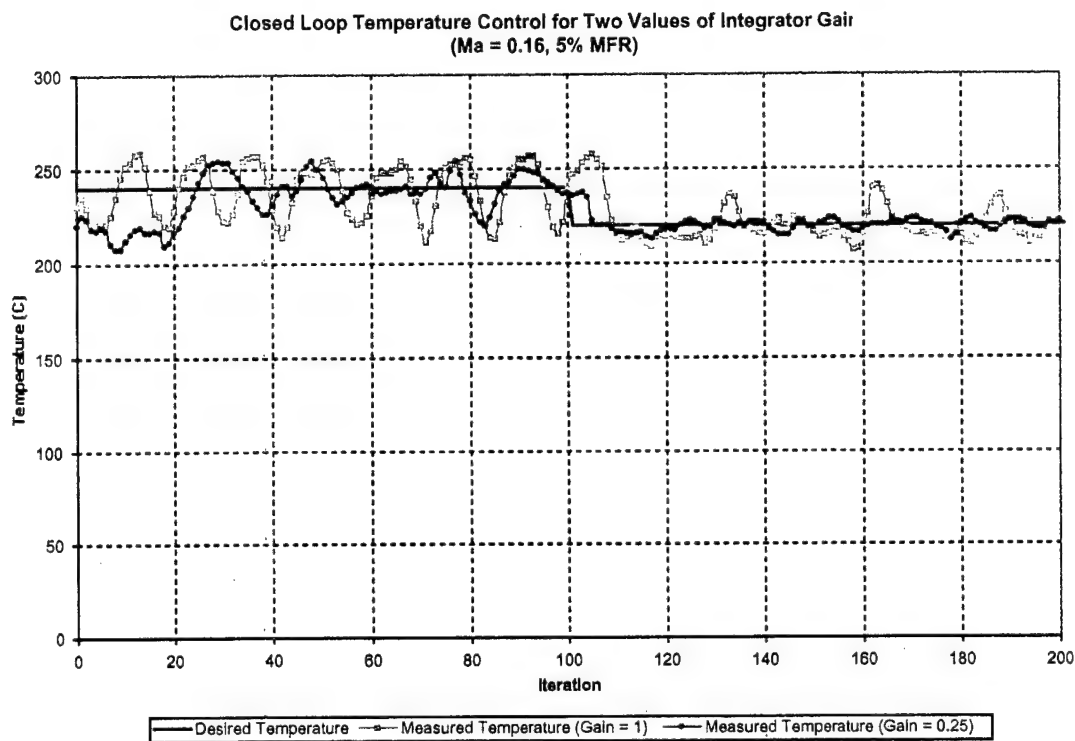


**Figure 5-4. Real-time feedback control of jet plume temperature via a classical proportional-integral controller.**

19

# 6.0 Conclusions

Large-scale direct numerical simulations performed for jets with various types of actuation proved useful for optimization of the actuators with regard to Strouhal number and amplitude. The integral of the squared velocity and the integral of the concentration proved to be appropriate objective functions for evaluating the performance of a given actuator. The simulations revealed that the spreading of the jet and the amount of mixing depend strongly on the actuator Strouhal numbers and that spreading grows with the amplitude. Stochastic optimization techniques proved very efficient for optimization of the jet actuators, in particular evolution strategies and simulated annealing. The optimization was implemented by automatically varying the actuation parameters and calculating the objective function. It was found that a combined axial and helical actuation was more efficient with regard to jet mixing than just a helical actuation alone.

It was determined that a linear stability model for a turbulent jet was not amenable to incorporation in a classical controller. However, the piecewise-quadratic representation of the base flow provides a new computational scheme for rapidly performing jet stability analyses. An experimental data base for jet mixing based on a C-17 exhaust with excitation did not have the generality for mixing control in a laboratory jet experiment using a miniature (RAM 750) engine. An experimental database for the jet exhaust from this engine was used to provide a relation between the centerline temperature and forcing frequency for a range of actuator mass flow rates. With the classical proportional-integral controller, it was possible to determine real-time feedback control of plume temperature. An evaluation of the genetic algorithm in the experimental study demonstrated that this approach could drive the system to undesirable states during the optimization. However, it would be possible to use genetic algorithms to optimize the gains and other parameters associated with the classical feedback control technique. Such an effort would be a topic for follow-on research in this area.

# 7.0 References

Abergel, F. and Temam, R. 1990, "On Some Control Problems in Fluid Mechanics," *J. Theoretical and Computational Fluid Dynamics,* 303-325.

Cain, A. and Thompson, M., 1986, "Linear and Weakly Nonlinear Aspects of Free Shear Layer Instability, Roll-Up, Subharmonic Interaction and Wall Influence," *AIAA Paper 86-1047,* AIAA/ASME 4th Fluid Mechanics, Plasma Dynamics and Lasers Conference, Atlanta, May.

Cain, A., Roos, F., and Kegelman, J., 1990, "Computational and Experimental Observations on Near Field Characteristics of an Excited Free Shear Layer," Presented at the Twelfth Symposium on Turbulent Flows, Rolla, MO, Sept.

Cain, A., Bewley, T., Freund, J., and Colonius, T., 1998, "An Approach to Systems Modeling for Real-Time Control of Jet Flows," Proceedings of the 1998 Summer Program, Center for Turbulence Research, 133-139, November.

Drazen, P. G. and Reid, W. H., 1981, *Hydrodynamic Stability,* Cambridge Univ. Press

Freund, J. B. and Moin, P., 1998, "Mixing Enhancement in Jet Exhaust Using Fluidic Actuators: Direct Numerical Simulations," *ASME FEDSM98-5235.*

Gaster, M., 1962, "A Note on the Relationship between Temporally Increasing and Spatially Increasing Disturbances in Hydrodynamic Stability," *J. Fluid Mech.* 14, 222-224.

Ho, C. M. and Huerre, P., 1984, "Perturbed Free Shear Layers," *Ann. Rev. Fluid Mech.* 365-424.

Ikeda, Y., 1998, "Real-Time Active Flow Control Based on Modern Control Theory," *AIAA Paper 98-2911,* Presented at the AIAA Fluid Dynamics Meeting, Albuquerque, NM.

Morris, P. J., Giridharan, M. G., and Lilley, G. M., 1990 "On the Turbulent Mixing of Compressible Free Shear Layers," *Proceedings of the Society of London A.* 431, 219-243

Parekh, D. E., Kibens, V., Glezer, A., Wiltse, J. M., and Smith, D. M., 1996, "Innovative Jet Flow Control: Mixing Enhancement Experiments," 34th Aerospace Sciences Meeting and Exhibit, *AIAA Paper 96-0308.*

Viswanathan, K. and Morris, P. J., 1992, "Predictions of Turbulent Mixing in Axisymmetric Compressible Shear Layers," *AIAA J.* 30(6), 1529-1536.

# Appendix A

## Mixing Enhancement in Jet Exhaust
## Using Fluidic Actuators: Direct Numerical Simulations

**A. Hilgers, P. Moin, and J. B. Freund**

# Appendix A

## Mixing enhancement in jet exhaust using fluidic actuators: direct numerical simulations

**NOMENCLATURE**

$a$ Speed of sound
$D$ Jet diameter
$e$ Fluid total internal energy
$r$ Jet radial coordinate
$r_o$ Jet radius
$St_D$ Strouhal number $= fD/U_j$
$T_a$ Actuator fluid temperature
$T_j$ Jet exhaust fluid temperature
$T_\infty$ Ambient fluid temperature
$U_a$ Peak actuator fluid velocity
$U_j$ Jet exit centerline velocity
$u_x$ Axial velocity
$v_r$ Radial velocity
$v_\theta$ Azimuthal velocity
$x$ Jet axial coordinate measured from nozzle
$\theta$ Jet azimuthal coordinate
$\rho$ Fluid density
$\xi$ Scalar concentration

# INTRODUCTION

This work is part of a larger project which is exploring means to control free shear flows to enhance mixing or reduce acoustic emission. Presently, these are separate goals because increased mixing will often increase noise. Increase mixing is sometime desired in aircraft jet exhaust to disperse hot gases quickly. Similarly, in combustors enhanced mixing increases the net reaction rate and thereby combustor efficiency. Suppression of acoustic emission has obvious application in the civilian aircraft industry where noise reduction is a key design goal for both present day subsonic and proposed supersonic aircraft. Presently, we distinguish mixing augmentation and noise reduction as separate goals because enhanced mixing will often increase noise.

Previous studies of jet forcing have been conducted in laboratory experiments. Parekh *et al.* (1996) excited the jet shear layer adjacent to the jet nozzle exit with both high frequency piezoelectric actuators and fluidic actuators. We will focus on the fluidic actuators which act on the jet by blowing fluid toward or pulling fluid away from the shear layer. Fluidic actuators, particularly those that are purely blowing, show promise for application in real jet engines because of the availability of high pressure in the compressor. Naturally the 'cost' of control will depend upon how much mass flow and at how much pressure is needed to effect the desired response in the jet. In small scale experiments, Parekh *et al.* (1996)

found that remarkably little mass flow (1%) could dramatically increase the mixing and change the overall behavior of the jet downstream. In one configuration they placed thin slot jet actuators blowing normal to the shear layer on opposite sides of the jet (see Fig. .1). When forced at a Strouhal number, $St_D = 0.2$ and with mean injection velocity of $0.27U_j$, the length of the potential core was reduced from 4 to 2 jet diameters. The jet, which was axisymmetric in the mean without forcing, was seen to flap violently in the plane of the actuators. This was reflected in the mean velocity profiles downstream which became very broad in the plane of the actuators.

It is desirable from a control theory perspective to develop a simple model for the jet and its response to forcing. Linear analysis may offer such a model, but its applicability is uncertain in this case because the actuator forcing amplitude is quite high. For example, the forcing used by Parekh *et al.* (1996) has a root-mean-squared value of the same order as the turbulent kinetic energy in the absence of forcing. The suggestion that linear methods may be applicable is due to the remarkable success they have seen in unforced free shear flows (*e.g.* Morris *et al.* 1990) in the presence of high amplitude disturbances. In the language of control theory, direct simulation of the complete system offers an excellent means of evaluating estimates for its state and response to control. Direct simulations also offer a detailed description of the dynamics which is unavailable by other means.

The present study explores the possibility of direct numerical simulation of forced jets and develops appropriate techniques for their computation. There are several key issues that need to be addressed. Boundary conditions, particularly those capable of providing very thin shear layers near the nozzle exit, are important. If the shear layers are too thick, the receptivity of the layer will change dramatically and so will the response of the jet to the forcing. Incorporation of the actuators themselves is also important and must be accomplished in a robust fashion that does not compromise their effects. From a practical standpoint, it is also necessary that the inclusion of the actuators not require a large number of mesh points. Solutions to these problems, along with the particulars of the flow are discussed in the following section. This is followed by a discussion of some results, including a comparison with experiments.

# PRELIMINARIES

## Flow description

The subject of the present study is a Mach 0.8 round jet exhausting into quiescent ambient fluid. The jet temperature ratio was $T_j/T_\infty = 2$. Fluidic actuators in the form of slot jets were located on opposite sides of the initial jet shear layer near the nozzle exit (see Fig. .1). This geometry is similar to that of Parekh *et al.* (1996). The temperature of the actuator fluid was $T_a/T_\infty = 1.5$. The actuators were forced out of phase with each other at $St_D = 0.2$ with exit velocities sinusoidally varying between 0 and $0.35U_j$. The jet and actuator fluids were marked separately with passive scalars ($\xi_1$ and $\xi_2$ respectively) which diffused with Schmidt number $Sc = 1$. The Prandtl number was $Pr = 0.7$ and the Reynolds number was limited to $Re_j = \rho_j U_j D_j/\mu_j = 800$. This is significantly lower than in the experiments of Parekh *et al.* and orders of magnitude smaller than in actual jet engines, but it is well known that many global characteristics of free shear flows are independent of Reynolds
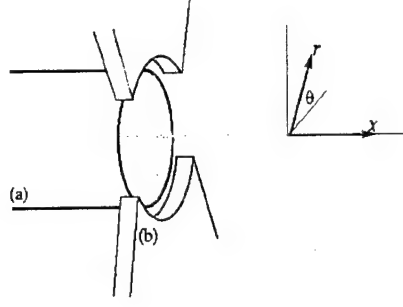
24

*Appendix A*



Figure .1: Geometry schematic showing the jet nozzle (a) and the actuators (b).

number. In jets at similar Mach number, it has been found that decreasing the Reynolds number tends to increase the potential core length but otherwise the mean velocity profiles are very similar at different Reynolds numbers (Stromberg *et al.* 1980). At low Reynolds numbers, the jet shear layer takes longer to transition to turbulence (this causes the longer potential cores), but this does not seem to effect the present study where the forcing excites a single mode which then dominates the flow above any turbulent fluctuations.

## Numerical Methods

The fully compressible Navier-Stokes equations and two passive scalar transport equations were solved in cylindrical coordinates without modeling assumptions. Here we give only a summary of the method, details are given in Freund *et al.* (1997) where the same code was used to study turbulence in compressible mixing layers. Sixth order compact finite differences (Lele 1992) were used in the streamwise ($x$) and radial ($r$) directions and a Fourier spectral method was used in the azimuthal direction ($\theta$). Time advancement was accomplished with an explicit fourth order Runge Kutta algorithm. At the $r = 0$ coordinate singularity, the equations were solved in Cartesian coordinates. To maintain a reasonable numerical time step given the restriction imposed by the Runge Kutta algorithm, higher Fourier modes in $\theta$ were not used near $r = 0$. They were omitted systematically so that the effective azimuthal resolution remained nearly constant with radial location. The computational mesh was $320 \times 180 \times 96$ points in the axial, radial, and azimuthal directions respectively and points were compressed in the radial direction around $r = r_o$.

The boundary conditions, the jet nozzle, and the actuators were all included in the calculation by modifying the equations in localized regions of the computational domain. For the boundary conditions, terms were added to the equations in a zone surrounding the physical portion of the domain. The purpose of these terms was to reduce the effect of truncating the computational box at a finite distance and to form an appropriately thin jet shear layer as an inflow condition. Taking $\mathbf{N}(\mathbf{q}) = 0$ to be the governing equations in conservative form, where $\mathbf{q} = [\rho, \rho u, \rho v_r, \rho v_\theta, e, \rho\xi_1, \rho\xi_2]^T$ is a vector of the conservative variables, the modified equations are

$$\mathbf{N}(\mathbf{q}) = -\sigma(\mathbf{q} - \mathbf{q}_{\mathrm{g}}) - U_c \frac{\partial \mathbf{q}}{\partial x} \tag{.1}$$

where $\mathbf{q}_{\mathrm{g}}$ is the quiescent target state to which the solution is driven. These terms are
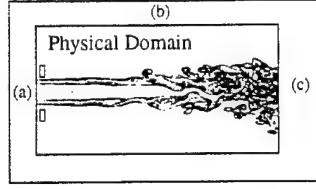
25

Figure .2: Computational domain schematic showing the "physical domain" and the boundary zones: (a) inflow zone, (b) far-field zone, and (c) outflow zone. The small boxes indicate the approximate location of the actuators.

non-zero only in the boundary zones shown schematically in Fig. .2. The physical portion of the domain was $25.5r_o$ long and extended to $6r_o$ in the radial direction. Zone (a) shown in Fig. .2 was $2r_o$ wide, zone (b) was $1.3r_o$ wide, and zone (c) was $2.5r_o$ wide.

The flow was driven toward a thin jet shear layer in zone (a) to mimic the effect of a nozzle. The value of $\sigma$ in this zone was $2a_\infty/r_o$ and the target axial velocity flow was

$$u_{x_g} = \frac{U_j}{2}\left(1 - \tanh\left[\frac{1}{\beta}\left(r - \frac{1}{r}\right)\right]\right), \tag{.2}$$

with $\beta = 0.06$. The density and scalar profiles were similarly specified. Taking $\chi = u_{x_g}/U_j$, the density profile was $\rho_g = (1 - \chi)\rho_\infty + \chi\rho_j$ and the scalar profile was $\xi_{1_g} = \rho_g\chi$. These profiles correspond to momentum thickness of approximately $\delta_m = 0.02r_o$. The complete target condition was then $\mathbf{q}_g = [\rho_g, \rho_g u_{x_g}, 0, 0, e_g, \rho_g\xi_{1_g}, 0]^T$, were $e_g$ is the total energy. To calculate $e_g$, we assume that the static pressure at the nozzle exit is equal to the ambient pressure. Away from the 'nozzle', the inflow non-reflecting boundary condition of Freund (1997) was applied.

In the outer radial boundary zone (b), $\sigma$ was

$$\sigma(r) = \left(\frac{r - 6r_o}{1.3r_o}\right)^3 \frac{a_\infty}{r_o} \tag{.3}$$

and $\mathbf{q}_g$ was set to the ambient conditions. The outflow boundary condition (c) was exactly as specified in Freund (1997). In (c), $\mathbf{q}_g$ was estimated by assuming self-similar incompressible flow (the centerline Mach number is significantly reduced as the right side of the domain is approached) and extrapolating from inside the domain. The flow well upstream of the boundary was found to be insensitive to the particular outflow boundary conditions. It will be seen that the flow changes dramatically when forced, and work is currently underway assessing how best to adjust the boundary conditions for this.

To provide a seed for the turbulence, random velocity fluctuations were added to the flow. This was done with a $\sigma$-term as in (.1) acting at the first mesh point inside the inflow boundary. We found that $\sigma = 2.8$ and $\mathbf{q}_g = [\rho, \rho\phi_{rnd}, \rho\phi_{rnd}, \rho\phi_{rnd}, e, \rho\xi_1, \rho\xi_2]^T$, where $\phi_{rnd}$ are random numbers $\phi_{rnd} \in (-1, 1)$, provided a sufficient seed for the turbulence. Each mesh point and velocity component was assigned a new random number every time step. The actuators extended from $x_1 = 0.26r_o$ to $x_2 = 0.92r_o$ in the axial direction and from $r_1 = 1.24r_o$ to $r_2 = 3.51r_o$ in the radial direction. In this region, $\sigma = 2a_\infty/r_o$ and $\mathbf{q}_g = [.75\rho_\infty, 0, -.75\rho_\infty v_a, 0, e_a, 0, .75\rho_\infty]^T$ with $e_a$ calculated from $.75\rho_\infty$, $v_a$, and the ambient

26
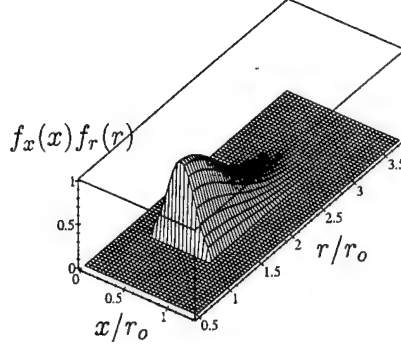
Figure .3: The $x$–$r$ shape of the actuation velocity.

pressure. Pure $\xi_2 = 1$ marked the actuator fluid. The instantaneous actuator target velocity was

$$v_a = U_a f_x(x) f_r(r) f_\theta(\theta) f_t(t). \tag{.4}$$

Its amplitude was set at $U_a = .44 U_j$, but the actual peak $v_r$ at the actuator typically only reached $.35 U_j$. The spatial and temporal dependencies of $v_a$ were

$$f_x(x) \qquad\qquad = e^{-\alpha_x(x-0.5(x_1+x_2))^2} \tag{.5}$$

$$f_r(r) \qquad\qquad = e^{-\alpha_r(r-r_1)^2} \tag{.6}$$

$$f_\theta(\theta) \quad = \exp[-\zeta(\theta)^{8e^{-\zeta(\theta)^2}+2.8}] + \exp[-(\zeta(\theta)-4)^{8e^{-(\zeta(\theta)-4)^2}+2.8}] \tag{.7}$$

$$f_t(t) \qquad\qquad = 0.5[1 + \sin(2\pi St_D U_j t/D)\mathrm{sgn}(\sin\theta)], \tag{.8}$$

where $\alpha_x = 20.4$, $\alpha_r = 1.34$, and $\zeta(\theta) = 8\theta/2\pi - 2$. The $x$–$r$ shape of $v_a$ is plotted in Fig. .3 and the azimuthal dependence is plotted in Fig. .4. The 'sgn' term in (.8) makes the actuators act out of phase.

## RESULTS

The velocity field in a $x$–$r$ plane region around an actuator near peak blowing is shown in Fig. .5. To make viewing of the vectors easier, only every other mesh point in the axial direction and every fourth mesh point in the radial direction are shown. There are only 9 mesh points across the actuator in the streamwise direction and those in the middle of the actuator, where the Gaussian axial distribution peaks, carry most of the mass flux. The vectors show that fluid is blown out of the actuator and into the jet shear layer with a pattern that resembles an asymmetric stagnation point on a wall. Also like a stagnation-point flow, there is a region of elevated pressure near the stagnation point just below the actuator. This causes the main jet flow to deflect slightly downward. The bulk of the

27

Figure .4: The $\theta$ shape of the actuation velocity.

actuator fluid is turned downstream by the main jet flow, but a small amount also turns upstream. This will also be shown below where a passive scalar is used to track the actuator fluid.

The downstream development of the unforced and forced shear layers are shown in Figs. .6 and .7 respectively. In the unforced case, the shear layer spreads slowly downstream and it eventually pinches off the poten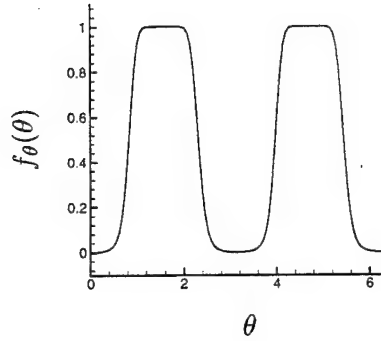tial core at around 18 jet radii from the 'nozzle' exit. Instabilities in the mixing layers grow slowly and, though structures are apparent, no mode appears dominant. In the forced case, the single mode forced by the actuators dominates the flow. After the potential core closes, the jet spreads very quickly in the plane containing the actuators, while in the plane perpendicular to it the jet spreads slowly. The rapidly spreading portion of the jet reaches the boundaries of the computational domain in only a short distance.

It is of interest to track the jet and actuator fluids with passive scalars. Figure .8 shows concentration contours of both jet and actuator fluids. The actuator fluid is pulled downstream by the jet flow and quickly mixes into the jet shear layer. Again there is evidence that a small amount is also sent upstream toward the 'nozzle', but the nearby pretense of the inflow boundary zone prevents on from reaching any conclusions regarding how far upstream it does travel. By the point where the potential core closes, the actuator fluid is very diffuse and its mixture fraction is below $\xi_2 = 0.05$ at all points downstream. Contours of jet fluid concentration show evidence of large scale structures near the end of the potential core which send fluid in mushroom like ejections away from the centerline of the domain. Jet fluid clearly accounts for the bulk of the flow downstream and the ratio of jet fluid to actuator fluid in the whole domain is 30:1. Though their mass flux is small, these actuators have significantly higher mass flux relative to the jet than do the experiments of Parekh *et al.* (1996). It is desirable to make the actuators smaller and the jet shear layers thinner to be in better accord with those experiments, but to do this would require more mesh points. To reduce the size of the actuators, it may also be necessary to increase the Reynolds number so that viscosity does not overwhelm their action. Increasing the Reynolds number would also increase the resolution requirements for the entire turbulent portion of the flow and this may quickly become prohibitively expensive with direct numerical simulation. So, the
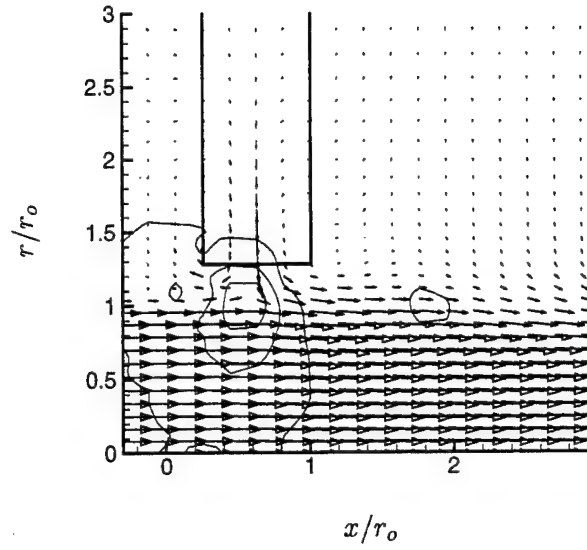
28

Figure .5: Actuator velocity field at $\theta = \pi/2$. The boxed region shows region of non-zero forcing. Contours show pressure at $(p - p_\infty)/\rho_j u_j = 0.006, 0.043$ and $0.079$.
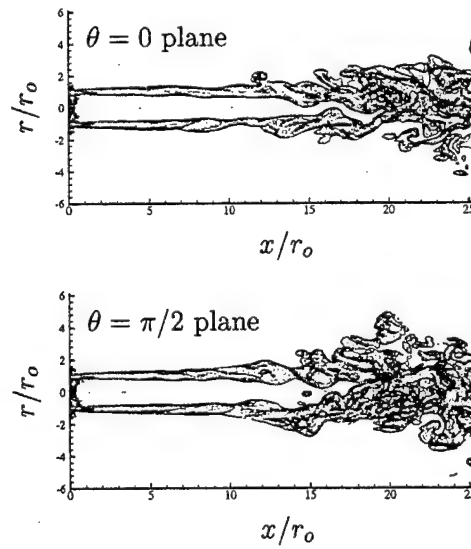


Figure .6: Vorticity magnitude contours for the unforced case. There are 40 evenly spaced contours with maximum $\omega r_o/u_j = 8.43$.
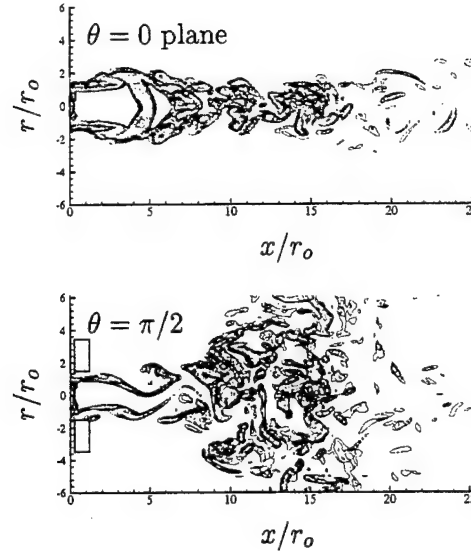
Figure .7: Vorticity magnitude contours for the forced case. Rectangles indication the actuator locations. There are 40 evenly spaced contours with maximum $\omega r_o/u_j = 8.43$.

effect of reducing the actuator mass flow while maintaining the peak actuator velocity is not known. However, it was straightforward to increase the actuator mass flux. Increasing it by roughly a factor of 3 only further reduced the potential core length slightly ($\sim 15\%$). Though these simulations have only run for a short time, the statistical sample was sufficient to estimate the mean axial velocity. Figure .9(a) shows the centerline velocity for the forced and unforced cases. The curves are not smooth because of the small statistical sample available. In the forced case, the centerline profile drops abruptly a short distance from the nozzle. If we define the end of the potential core as the point where $\bar{u}(r = 0)$ starts to drop, then we see that its length is halved by the forcing. These results are very similar to those of Parekh *et al.* (1996) who also observed a factor of 2 drop in the potential core length. Velocity profiles at 19 radii downstream from the nozzle are shown in Fig. .9(b). The peak velocity drops dramatically between the forced and unforced cases. Surprisingly, the mean flow becomes nearly uniform across the entire computational domain in the $\theta = \pi/2$ plane. Similarly flat profiles were observed by Parekh *et al.* The profile in the $\theta = 0$ plane has the same Gaussian shape as the unforced case. Reversed flow is observed for the forced case in the $\theta = 0$ plane. This is believed to be either a transient associated with the startup of the actuators or an effect of the boundary conditions. Work is underway to resolve this.

The goal of the actuation was to increase downstream mixing. To quantify this further, we will estimate the total amount of heat radiation from the jet. If we assume that every point acts as a black body radiator, then the total radiated energy is proportional to

$$\int_V (T^4 - T_\infty^4)dV \qquad (.9)$$

where take $V$ is the physical portion of the computational domain. Using this very simple

30

*Appendix A*
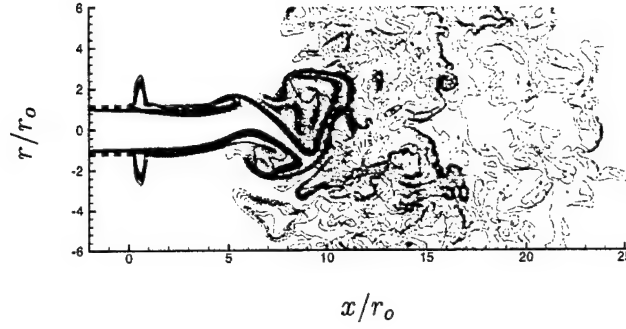


Figure .8: Scalar concentration. The dark contours show actuator fluid with levels 0.05 to 0.25 and spacing 0.05 and level 1.0 is pure actuator fluid. The light contours show jet fluid with levels 0.05 to 0.95 with 0.05 spacing and 1.0 is pure jet fluid. The 'nozzle' location is indicated by the heavy dashed lines.
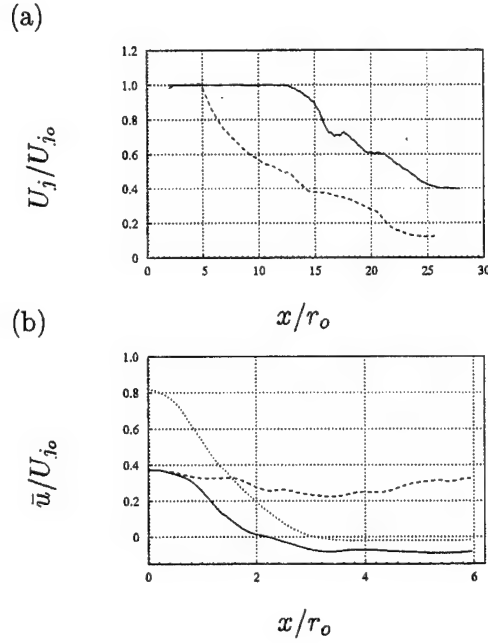


Figure .9: (a) Jet centerline velocity for the unforced —— and forced ---- cases. (b) Mean axial velocity at $x = 19r_o$ for the unforced jet ········ ; the forced jet in the $\theta = 0$ plane —— ; and the forced jet in the $\theta = \pi/2$ plane ---- .

31

estimate, the total radiated energy drops by a factor of 2 due to the actuation.

## CONCLUSIONS

Direct numerical simulations of forced jets have been performed which match qualitatively with the experiments of Parekh *et al.* (1996). New techniques for generating thin shear layer jet inflow boundary conditions and for including small actuators into the computations were successfully developed. It was found that the actuators need only slightly perturb the thin jet shear layer near the nozzle to cause a dramatic change in the overall flow development downstream. Mixing, as measured by an estimate of the total energy radiation from hot jet gases, was suppressed by a factor of 2 due to the actuation. The potential core was similarly shortened by a factor of 2.

Work continues to study aspects of the forcing which are difficult to analyze experimentally and a project is presently underway to calculate the optimum temporal profile for forcing. It will also be useful to test how well linear modal analyses may predict the observed reaction of the jet to forcing. Acoustics are difficult to study experimentally because it is hard to simultaneously measure the acoustic sources and the sound field. Simulations may offer insight into means of reducing acoustic emission by forcing near the nozzle.

## REFERENCES

J. B. Freund, 'A proposed inflow/outflow boundary condition for direct computation of aerodynamic sound', *AIAA J.* **35**, 4, 1997.

J. B. Freund, P. Moin, and S. K. Lele , 'Compressibility effects in a turbulent annular mixing layer', Technical Report TF-72, Stanford University, Mechanical Engineering, Flow Physics and Computation Division, September 1997.

S. K. Lele, 'Compact finite difference schemes with spectral-like resolution', *J. Comp. Phys.* **103**, 16, 1992.

P. J. Morris, M. G. Giridharan, and G. M. Lilley, 'On the turbulent mixing of compressible free shear layers', *Proc. Royal Soc. Lond. A* **431**, 219, 1990.

D. E. Parekh, V. Kibens, A. Glezer, J. M. Wiltse, and D. M. Smith, 'Innovative jet flow control: mixing enhancement experiments', 34th Aerospace Sciences Meeting and Exhibit, *AIAA* Paper 96-0308, 1996.

J. L. Stromberg, D. K. McLaughlin, and T. R. Troutt, 'Flow field and acoustic properties of a Mach number 0.9 jet at a low Reynolds number', *J. of Sound and Vib.* **72(2)**, 159, 1980.

# Appendix B

## Jet Mixing Enhancement by High Amplitude Fluidic Actuation

A. Hilgers, P. Moin, and J. B. Freund

# Appendix B

## Jet mixing enhancement by high amplitude fluidic actuation

**Summary**

Recent experiments have shown that properly designed high amplitude, low mass flux pulsed slot jets blowing normal to a jet's shear layer near the nozzle can significantly alter the jet's development (Parekh *et al.*, AIAA Paper 96-0308). In contrast to commonly used low amplitude forcing, this strong excitation appears to overwhelm the turbulence, having nearly the same effect at high and low Reynolds numbers. It can therefore be studied in detail by direct numerical simulation. In this study, direct numerical simulations of Mach 0.9, Reynolds number 3600 jets exhausting into quiescent fluid are conducted. Physically realistic slot jet actuators are included in the simulation by adding localized body-"force" terms to the governing equations. Three cases are considered in detail: a baseline unforced case and two cases that are forced with flapping modes at Strouhal numbers 0.2 and 0.4. ($St = 0.4$ was found to be the most amplified frequency in the unforced case.) Forcing at either frequency causes the jet to expand rapidly in the plane parallel with the actuators and to contract in the plane perpendicular to the actuators, as observed experimentally. It is found that the jet responds closer to the nozzle when forced at $St = 0.4$, but forcing at $St = 0.2$ is more effective at spreading the jet further downstream. Several different measures of mixing (scalar dissipation, volume integrals of jet fluid mixture fraction, and point measurements of mixture fraction) are considered, and it is shown that by most, but not all, measures forcing at $St = 0.2$ is the more effective of the two at mixing.

## Nomenclature

$a$     = speed of sound
$D$     = jet diameter
$\mathcal{D}$     = planar integral of $|\nabla \xi|$
$e$     = total energy
$\mathcal{J}$     = volume integral of $\xi^n$
$\mathcal{M}$     = planar integral of $\xi^n$
$r$     = radial coordinate
$r_o$     = jet nozzle radius
$St$     = forcing Strouhal number $= fD/U_j$
$T$     = temperature
$U_a$     = peak actuator fluid velocity
$U_j$     = jet exit velocity
$v_x$     = axial velocity
$v_r$     = radial velocity
$v_\theta$     = azimuthal velocity
$x$     = axial coordinate
$\theta$     = azimuthal coordinate
$\rho$     = fluid density
$\xi$     = jet fluid mixture fraction
$\omega$     = vorticity magnitude

# Introduction

There are several technological applications where enhanced jet mixing can lead to improved efficiency, reliability, or safety. For example, enhanced jet mixing can reduce temperatures on in-plume aerodynamic surfaces, such as the blown flap on a C-17 aircraft, and thus provide greater flexibility in the choice of materials for their construction. Similarly, the mixing efficiency of fuel jets in combustors is an important factor in their overall performance, with size and weight reductions possible if mixing is improved. In the present work we focus on free jets, with the principle objective being plume temperature reduction.

In general, attempts to control jets can be divided into two categories: active and passive. Examples of passive control are tabs located at the nozzle exit,[1,2] crown shaped nozzles,[3] and various other tailorings of the nozzle exit.[4–6] This list is far from exhaustive. Passive control is attractive because in many cases it entails only simple design modifications, a change in nozzle geometry for example. Also its simplicity typically makes the resulting hardware less subject to failure. However, active control, where nozzle conditions are continuously updated, has greater flexibility and therefore greater potential to modify the jet flow. In this study we analyze a recently proposed method for active control of high Reynolds number jets.[7]

In the past, active excitation has been used extensively to understand the dynamics of free shear flows, particularly the dynamics of the largest turbulent flow structures. Studies up to the mid 1980's are summarize by Ho & Huerre[8] and relatively more recent efforts are discussed by Koch et al.[9] and Ho et al.[10] Here, the excitation used was typically low amplitude, often serving only to seed instability waves in the flow in order to phase correlate coherent structures. Unfortunately, it seems that to modify the flow significantly at high Reynolds numbers, low amplitude forcing is ineffective because the applied perturbations are overwhelmed by the turbulence. Thus, control by low amplitude excitation is not practical in many flows of engineering interest.

Recently, a scheme has been developed to control high Reynolds number jets, such as the exhaust flow from jet engines, by forcing with actuation velocities greater than the local turbulence intensity. This approach was tested by Parekh et al.[7] who designed slot jets that blew normal to the jet shear layer adjacent to the nozzle (as in figure 0.1). When pulsed 180° out of phase from one another with peak blowing at approximately one third the jet velocity (and approximately 2 percent of the jet mass flux), they excited large-scale oscillations in the jet that reduced the potential core length by over a factor of two. Recent test results have shown mixing enhancement using this technique on a full-scale engine.[11] Similar results have been obtained using zero net mass flux "synthetic jets".[7,12,13] It appears that these active control approaches have been more successful at increasing mixing at high Reynolds numbers than any attempts by passive control approaches. Obviously the direct numerical simulations used in this effort are incapable of addressing high Reynolds number flows, but we shall see that the behavior of the simulated forced jets is similar to that observed at high Reynolds numbers, and new insights are provided.

Thus far, the forcing parameters in these experiments have been picked beforehand, as in an "open-loop" control strategy. "Closed-loop" control, where the jet flow would be continuously monitored and its state used to update the control parameters, may offer improved performance. To implement this approach a practical measure of the performance (an objective or "cost" function) is needed. An objective of the present effort is to study metrics for mixing and provide a database for direct comparison of different metrics. The choice of a metric for a particular application will depend not only upon its relevance for the given mixing objective but also on practical aspects of its implementation. Here we concentrate only upon the metrics themselves.
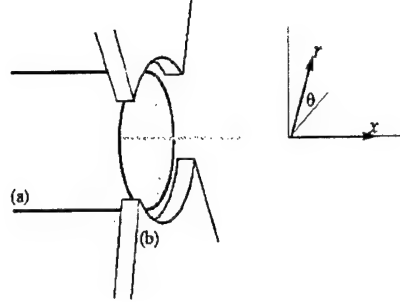
Figure 0.1: Geometry schematic showing the jet nozzle (a) and the actuators (b).

## Flow parameters

The focus of this paper is a round jet at Mach 0.9. The jet Reynolds number, based upon centerline flow conditions at the nozzle exit, is 3600, and the stagnation temperature of the jet is constant. These parameters match those studied experimentally by Stromberg *et al.*[14] and a baseline, unforced case has been validated against their data.[15] Direct comparison shows that mean Mach number profiles (and the overall sound pressure levels on an arc at 60 radii from the nozzle) agree to within 5 percent. Unfortunately, the precise nozzle conditions were not measured, but spectra show that the initial jet shear layers were laminar, as expected at this Reynolds number. To model appropriate nozzle conditions a rounded 'top-hat' velocity profile was specified in the present simulations (see *Appendix A*). Small amplitude ($v' < 0.01U_j$) random velocity fluctuations were added to this in order to seed the turbulence. The consequence of not adding random perturbations was a prolonged region of laminar flow near the nozzle, but the flow downstream was not particularly sensitive to the nature of these disturbances provided that they contained a range of frequencies and wavenumbers.

Slot jets pictured in figure 0.1 were used to excite the flow in a manner similar to the experiments of Parekh *et al.*[7] Each slot extended 90° around the jet and blew normal to the shear layers just downstream of the nozzle. The techniques for including these actuators in the simulations and their exact specifications are outlined with the numerical method in *Appendix A*. The individual slot jets blew 180° out of phase from one another to excite a flapping mode in the jet and their velocity varied sinusoidally between 0 and $0.6U_j$. The net mass-flow fraction of the actuators was $\dot{M}_{\mathrm{act}}/\dot{M}_{\mathrm{jet}} \approx 0.035$. Two forced jets where computed. The first was forced at Strouhal number $St = 0.2$, which had been found experimentally to be very effective at spreading the jet.[7] The other case was forced at $St = 0.4$, which was the most amplified frequency of the unforced jet, as found both by the simulations and the cited experiment.[14]

## Results

### Visualizations

Figure 0.2 shows a vorticity magnitude visualization of the unforced case. The initial jet shear layers are seen to be laminar. By $x = 5r_o$ instability waves appear which develop into Kelvin-Helmholtz rollers by $x = 10r_o$. Their passing frequency is $St = 0.4$, in accord with the experiments of Stromberg *et al.*[14] who found that $St = 0.44$ was the peak Strouhal number in the early development of their jet, subject to $\pm10\%$ day-to-day variation in their facility. At the instant shown the potential core extends to approximately $x = 17r_o$. Near the end of the potential core a transition to turbulence occurs which is corroborated by Reynolds stress statistics that will be reported
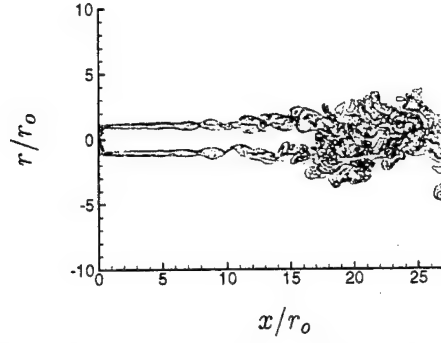
Figure 0.2: Vorticity magnitude contours for the unforced case in an $x$–$r$ plane. There are 40 evenly spaced contours with maximum $\omega r_o/U_j = 8.43$.
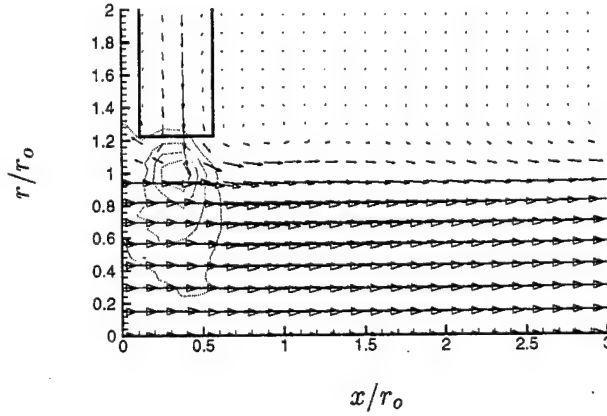


Figure 0.3: Actuator flow impinging on the jet shear layer. Every other mesh point in $x$ and every sixth mesh point in $r$ is shown. The solid rectangle indicated the extent of the actuator. Light contours show $(p - p_\infty)/\rho_j U_j^2$ at evenly spaced intervals (min = 0.0333, max = 0.133).

elsewhere.[15]

Figure 0.3 shows a close-up of an actuator near its peak blowing condition. (The $St = 0.2$ case is shown, but the $St = 0.4$ case is similar.) There were only 8 mesh points across the modeled actuator in the streamwise direction and those near the center of the actuator, where the Gaussian axial velocity distribution peaks (see *Appendix A*), carry most of the momentum flux. A region of increased pressure just below the actuator is also shown with contours in the figure. The initial effect of the forcing on the jet is seen just downstream of the actuator where the primary jet flow is slightly deflected. The bulk of the fluid exiting the actuator appears to be turned downstream as it encounters the jet, however a portion of it is also turned upstream, giving the appearance of a stagnation point flow. The pressure rise in this region is also reminiscent of a stagnation point flow.

The result of the forcing downstream is visualized in figures 0.4 and 0.5 for the $St = 0.2$ and 0.4 cases respectively. It is clear for the $St = 0.2$ case that the actuators excite the jet significantly and that it spreads rapidly in the $\theta = \pi/2$ plane. In the $\theta = 0$ plane, the spreading is suppressed. A single mode appears to dominate the early development of the jet as evidenced by the large structures visible before $x = 10r_o$. The instantaneous visualization in figure 0.4 shows the potential core closing at approximately $x = 9r_o$. Downstream of this region, the vorticity magnitude field

37

Figure 0.4: Vorticity magnitude contours for the cased forced at $St = 0.2$. Twenty evenly spaced contours between $\omega r_o/U_j = 0.6$ and 12.0 are shown.

shows an eruption of small-scale turbulence. A surprising feature of the visualization is the apparent symmetry near $x = 7r_o$ in the $\theta = 0$ plane. This is the characteristic feature of the large-scale coherent structures seen in the $\theta = \pi/2$ visualization as they intersect the $\theta = 0$ plane.

When the jet is forced at $St = 0.4$ (figure 0.5), the large-scale structures are smaller but appear earlier, which is not surprising because this is the most amplified frequency in the unforced jet. However, the downstream effect of the forcing is now quite different. The structures disappear or are obscured by small scales almost immediately and the jet spreads less in the plane of the actuators ($\theta = \pi/2$). Though the shear layers appear thicker early in the development, they slow their spreading and merge only at around $x = 13r_o$, beyond where they merge in the $St = 0.2$ case. The visualization in the $\theta = 0$ plane is similar to the $St = 0.2$ case, with similar symmetries at small $x$ due to the coherence of the excited structures, but a longer potential core.

Figure 0.6 shows a series of instantaneous visualizations of the jet fluid mixture fraction as it adjusts to forcing at $St = 0.2$. The time series starts from the unforced jet and the actuators turn on at $t = 0$. By $t = 10r_o/U_j$, there is clear evidence of large coherent structures distorting the scalar field. As expected, these travel at approximately $0.65U_j$, appearing at $x \approx 10r_o$, the horizontal midpoint of the region shown, at $t \approx 15r_o/U_j$. The scalar field takes considerably longer to develop further downstream where decreasing velocities slow advection. For computing statistics,

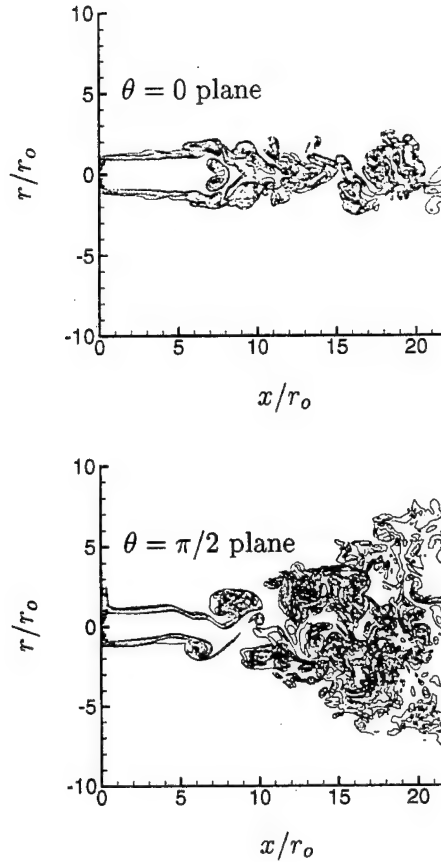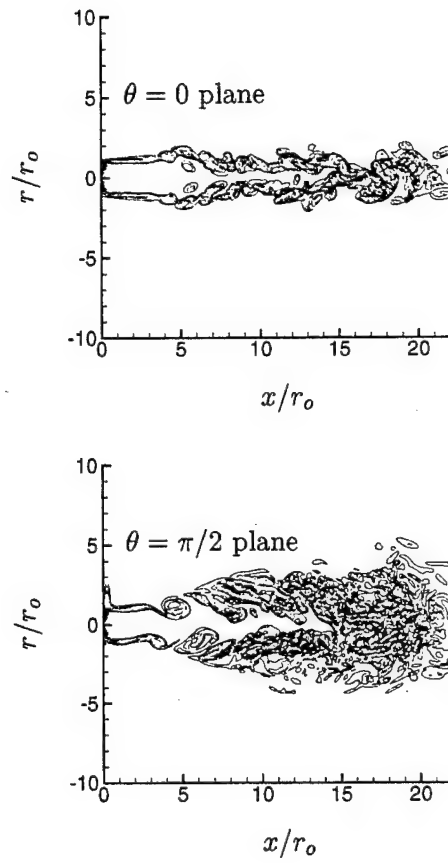Figure 0.5: Vorticity magnitude contours for the case forced at $St = 0.4$. Twenty evenly spaced contours between $\omega r_o/U_j = 0.6$ and $12.0$ are shown.

$t = 0r_o/U_j$                    $t = 5r_o/U_j$



$t = 10r_o/U_j$                   $t = 15r_o/U_j$



$t = 20r_o/U_j$                   $t = 25r_o/U_j$



$t = 30r_o/U_j$                   $t = 35r_o/U_j$



Figure 0.6: Development of the scalar field in the $\theta = \pi/2$ plane once $St = 0.2$ forcing is turned on at $t = 0$. Black is pure jet fluid, white is pure ambient fluid.

the forced jets were assumed to be fully developed only after $t = 80r_o/U_j$. The simulations were run to approximately $t = 150r_o/U_j$.

Figure 0.7 shows the corresponding set of images for the jet forced at $St = 0.4$. Again we see that at this forcing frequency, large structures appear closer to the nozzle than in the $St = 0.2$ case. The mixed regions in the jet shear layers thicken rapidly, but a tongue of pure fluid persists along the domain centerline. The flapping of the jet column is also less pronounced.

## Mean flow

Mean axial velocity ($\bar{v}_x$) provides a more quantitative measure of the effect of the forcing on the jet development. Approximately 700 fields spaced in time by $\Delta T_{\text{ave}} = 0.2r_o/U_j$ were averaged to compute the mean. Symmetries were exploited to increase the statistical sample. We see that the jet spreads as expected (see figure 0.8), first slowly where the shear layers are laminar, and then more quickly near the end of the potential core where the flow goes through transition. If $\bar{v}_x/U_j = 0.9$ is used to designate the end of the potential core, in this case the potential core closes at $x = 17r_o$, which is further downstream than would be expected for high Reynolds number jets,

40
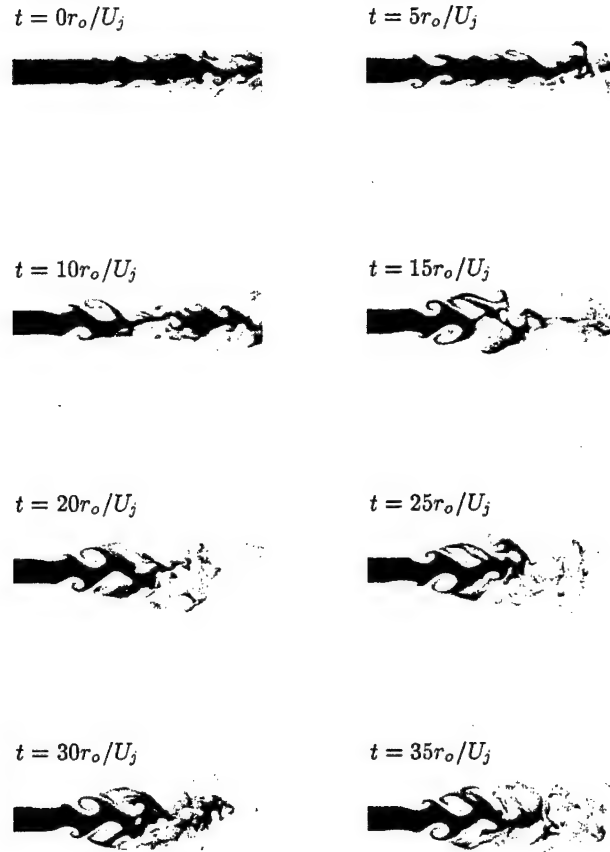
Figure 0.7: Development of the scalar field in the $\theta = \pi/2$ plane once $St = 0.4$ forcing is turned on at $t = 0$. Black is pure jet fluid, white is pure ambient fluid.
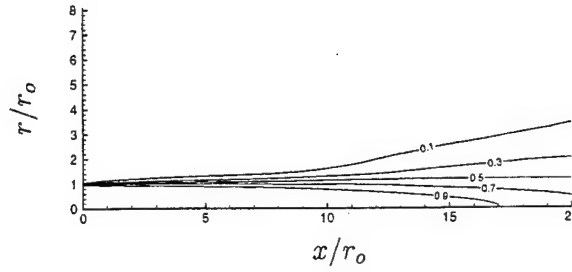
Figure 0.8: Mean axial velocity $(\bar{v}_x/U_j)$ for the unforced jet.
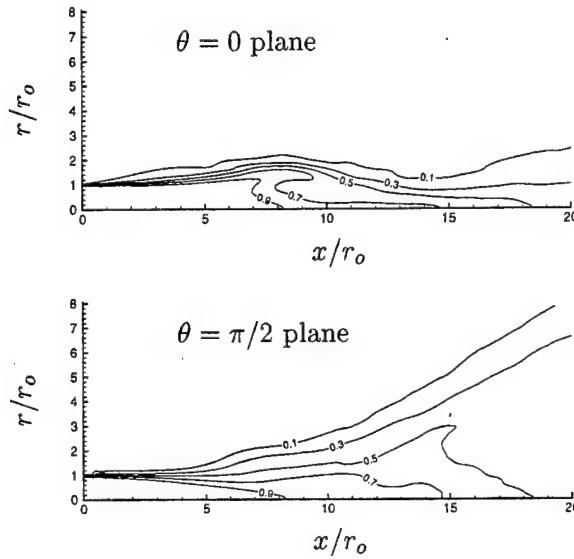


Figure 0.9: Mean axial velocity $(\bar{v}_x/U_j)$ for $St = 0.2$ forcing.

because the shear layers are initially laminar and therefore spread slowly.

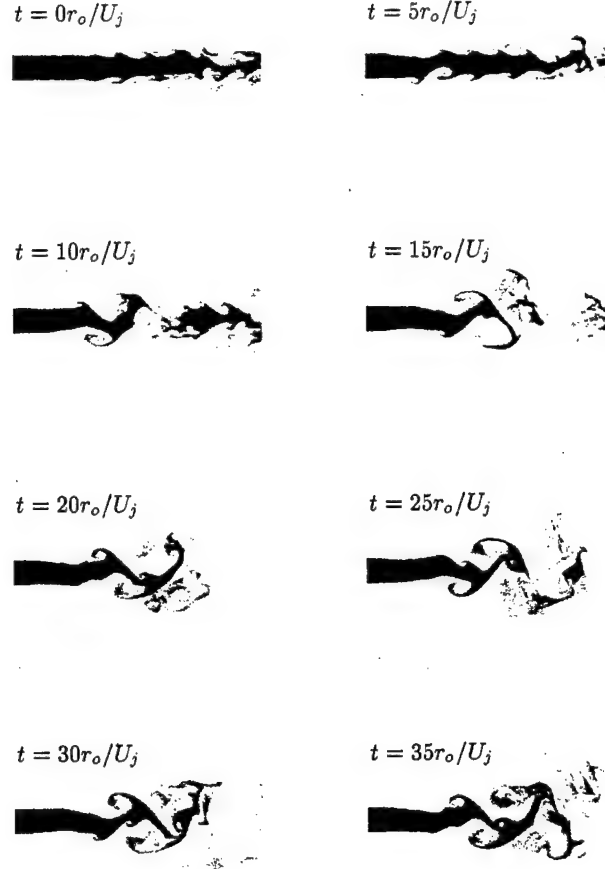Forcing at $St = 0.2$ dramatically alters the mean flow (figure 0.9). In the plane perpendicular to the action of the actuators ($\theta = 0$) the jet at first spreads more rapidly than the unforced case, but then this is reversed starting at the end of the potential core ($x = 8r_o$). Only near $x = 20r_o$ does the 10 percent velocity contour extend to the same radial distance as at $x = 8r_o$. The contours have an unusual thumb shape at $r = r_o$, $x = 8r_o$ that is caused by the large-scale structures seen in figure 0.4. Based on visualizations (*e.g.* figure 0.4), these structures first intersect the $\theta = 0$ plane near $r = 0$, and thus they bring lower velocity fluid into that region before the region near $r = r_o$. So at this downstream location the velocity is higher near $r = r_o$ which causes the appearance of the 'thumb'. In the $\theta = \pi/2$ plane, the jet is seen to spread rapidly starting near $x = 8r_o$ and this continues until the end of the computational domain at $x = 20r_o$. Parekh *et al.*[7] showed very similar results for forcing at this same frequency.

When the jet is forced at $St = 0.4$ (figure 0.10), the mean flow is markedly different. In the $\theta = 0$ plane, the jet only spreads until around $x = 5.5r_o$ before spreading is reversed. It does this significantly closer to the nozzle than in the $St = 0.2$ case. There is again an unusual shape to
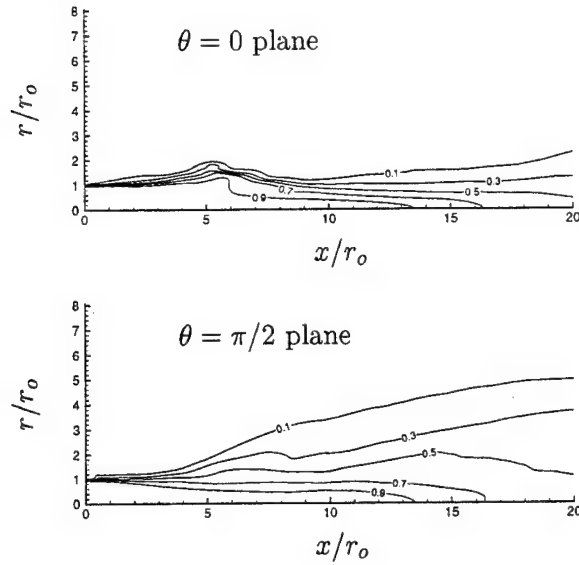
Figure 0.10: Mean axial velocity ($\bar{v}_x/U_j$) for $St = 0.4$ forcing.

the contours at this point, but at this forcing frequency it is less pronounced. Though spreading in the $\theta = 0$ plane is reversed at smaller $x$ than it was for $St = 0.2$ forcing, the potential core is now longer, extending to $x = 13.5 r_o$. In the $\theta = \pi/2$ plane, the jet spreads rapidly starting at around $5.5 r_o$, but spreading slows downstream and the jet does not grow as much radially as in the $St = 0.2$ case (figure 0.9).

## Unsteady response of the jet

To optimize the forcing, by either an open- or closed-loop approach, it is necessary to develop a measure of its effectiveness. Naturally, the choice of a definition for mixing effectiveness will depend upon the specific objective of the application. Here we will consider several metrics that are of potential use in temperature abatement or combustion applications.

### Point measurements of $\xi$

We first consider point measures of jet fluid mixture fraction ($\xi = 1$ for pure jet fluid and $\xi = 0$ for pure ambient fluid) on the jet axis. If the jet were hot, the concentration of jet fluid (mixture fraction) would closely correspond to temperature. Extensive centerline measurements have been made in forced jets and have been used to estimate the mixing enhancement of various forcings.[7] Figure 0.11 shows time histories of $\langle \xi \rangle$ on the jet axis ($r = 0$) and at $x = 5, 10, 15$ and $20 r_o$. The angle braces $\langle \rangle$ indicate an average over a single period of the forcing: $T_a = 9.9 r_o/U_j$ for $St = 0.2$ and $T_a = 4.9 r_o/U_j$ for $St = 0.4$. Despite this average, there is still considerable oscillation in the measure due to the chaotic nature of turbulence. Averaging for longer periods would, of course, smooth the profiles, but for closed-loop control applications it is important to be able to quickly measure the response of the jet to changes in the forcing. Longer averages would slow the response of the metric to the changes in the forcing.

We see in figure 0.11 that before forcing is initiated at $t = 0$, the flow is pure jet fluid at $x = 5 r_o$ and $x = 10 r_o$. At $x = 15 r_o$ there is slight mixing with ambient fluid and at $x = 20$,

43
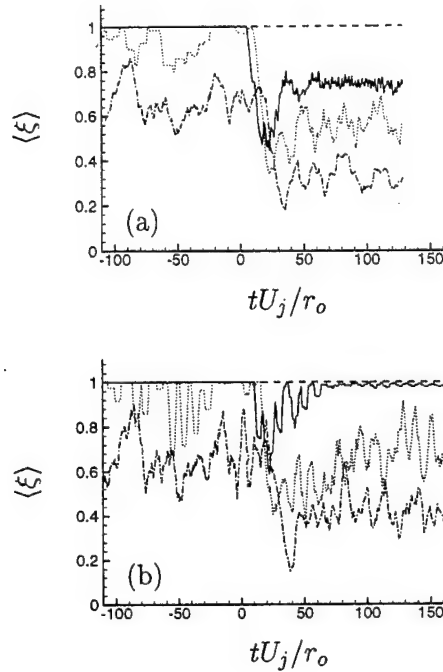
Figure 0.11: Time histories of scalar on the jet axis: ---- $x = 5r_o$; —— $x = 10r_o$; ········ $x = 15r_o$; and —·— $x = 20r_o$. (a) $St = 0.2$; (b) $St = 0.4$. Each curve shows a time average over one forcing period.

the mixture fraction hovers around its long-time (if forcing were not initiated) mean $\bar{\xi} = 0.65$. As expected from observations of the potential core length, the mixture fraction at $x = 5r_o$ is unaffected by the forcing at either Strouhal number. At $St = 0.2$ (figure 0.11 a), the mixture fraction at $x = 10r_o$ is the first to respond to the forcing. It initially decreases to $\langle \xi \rangle = 0.5$, but rises again and remains near the mean $\bar{\xi} = 0.75$ for $t > 60r_o/U_j$. The period averaged values at $x = 15r_o$ and $20r_o$ also seem to overshoot initially before they settle to hover around their apparent long-time mean values of $\bar{\xi} = 0.6$ and $\bar{\xi} = 0.3$ respectively. The small statistical sample size makes these values and the point where they are reached somewhat imprecise. Forcing at $St = 0.4$ also causes a greater reduction in centerline mixture fraction initially (figure 0.11 b). The curve at $x = 10r_o$ initially dips, but recovers to nearly its unforced, pure jet fluid level by $t = 70r_o/U_j$. The curves at $x = 15r_o$ and $20r_o$ hover around their mean values of $\bar{\xi} = 0.7$ and $\bar{\xi} = 0.4$. It is unclear why this case takes longer to equilibrate than the lower frequency forcing.

The initial overreaction of the jet to the forcing can be explained qualitatively with a simple model where the large-scale structures are assumed to be linear instability waves. Given this model, turbulent structures will grow, stabilize, and decay as the layer spreads. If the jet spreads slowly, as in the unforced case, there is a long region of growth before decay. So, given a significant initial forcing amplitude, the structures can become quite intense by a linear mechanism. However, high amplitude disturbances will also increase the spreading rate of the layer and thereby reduce the distance over which subsequent disturbances can amplify. Hence, by this model the first forced structure "sees" a slowly spreading layer and thus can grow more than subsequent disturbances that "see" a more rapidly spreading layer, which explains the observed overshoot.

This model can also explain the greater response of the jet to $St = 0.2$ forcing than forcing at its natural frequency $St = 0.4$. Instability analysis shows that for thicker shear layers, as would be
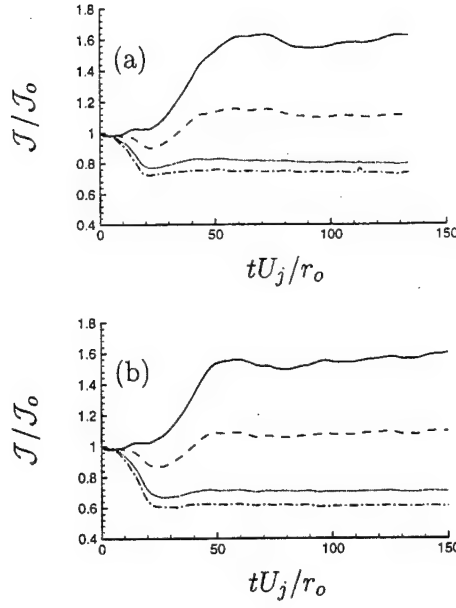
Figure 0.12: Integrals of $\xi^n$ with $n = 1$ ——— ; $n = 2$ ---- ; $n = 4$ ········· ; $n = 6$ —·— . (a) $St = 0.2$ forcing; (b) $St = 0.4$ forcing.

present in forced jets, the most amplified instability waves will have a longer wavelength and lower frequency.[16] Therefore, it is not surprising that $St = 0.2$ is more successful. Unfortunately, linear stability predictions can only loosely model the quantitative behavior of turbulence. An accurate quantitative prediction using linear stability analysis is therefore not likely to be successful in conjunction with the high amplitude forcing used in the present study.

*Volume integrals of $\xi^n$*

Volume integrals of $\xi^n$ can also provide a measure of mixing effectiveness. For $n \approx 4$ to 6 this will provide a crude model, assuming $\xi \propto T$, of the infrared signature of the jet. Time histories of

$$\mathcal{J} = \int_{\Omega_c} \xi^n \, dV, \tag{0.1}$$

where $\Omega_c$ is the physical domain ($x < 20r_o, r < 10r_o$), are shown in figure 0.12. No time averaging was necessary to smooth curves in this case. We see that the volume integrals of $\xi^1$ and $\xi^2$ both increase when the jet is forced. For both cases, the $\xi^1$ curve shows that there is 60 percent more jet fluid in the domain. Despite this increase, $\xi^4$ and $\xi^6$ decrease thus indicating improved mixing. The $\xi^6$ curve decreases from its unforced value $\mathcal{J}_o$ to $\mathcal{J} = 0.7\mathcal{J}_o$ for the $St = 0.2$ case and $\mathcal{J} = 0.6\mathcal{J}_o$ for the $St = 0.4$ case. It is somewhat surprising that the $St = 0.4$ case shows better mixing by this measure because the opposite was predicted based upon centerline measurements (figure 0.11). It may also seem counter to the visualizations and mean flow data which show greater spreading for $St = 0.2$ forcing. Because (0.1) depends on the axial dimension of the computational box, it is therefore important to also estimate downstream mixing based upon the available data. (Note that the finite radial dimension does not affect the result because $\xi \to 0$ by $r = 10r_o$, the radial box size.)

We can make such an extrapolation by computing mixedness as a function of downstream

45
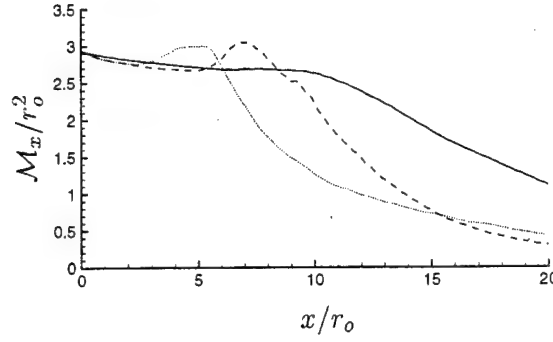
Figure 0.13: Planar integrals of $\xi^6$ from (0.2): —— unforced; ---- $St = 0.2$; ······· $St = 0.4$.

distance. Figure 0.13 shows the planar contributions to $\mathcal{J}$ as a function of $x$ for $t > 80r_o/U_j$:

$$\mathcal{M}_x(x) = \int_0^{2\pi} \int_0^{10r_o} \xi^6 \, r \, dr \, d\theta. \qquad (0.2)$$

It now becomes clear that the apparent advantage of $St = 0.4$ forcing is primarily a result of the jet's more rapid response to the forcing. At the outflow boundary we see that the $St = 0.2$ forced jet is actually mixed better (by this measure) and $\mathcal{M}_x$ has a steeper slope (rate of mixing) than the jet forced at $St = 0.4$. Though it is not possible to make firm judgments about the subsequent downstream mixing, based on the level and slope of $\mathcal{M}_x$ at $x = 20r_o$ it appears that the $St = 0.2$ case might be better if more downstream fluid could be included in (0.1). Both forced cases are clearly better than the unforced case also shown in the figure.

The asymmetry of the jets is seen in figure 0.14 which shows planar integrals of $\xi^6$ at constant $\theta$,

$$\mathcal{M}_\theta(\theta) = \int_{-20r_o}^{20r_o} \int_0^{10r_o} \xi^6 \, dr \, dx. \qquad (0.3)$$

For both forced cases, this metric peaks in the $\theta = \pi/2$ plane, the plane of the actuators. For both Strouhal numbers, this peak is roughly 1.75 times as high as the minimum values. Somewhat surprisingly these minima do not occur at $\theta = 0$ (see figure 0.14) which is perpendicular to the actuators. $\mathcal{M}_\theta$ is 20 percent higher at $\theta = 0$ than at its minima. Nearly everywhere $\mathcal{M}_\theta$ is suppressed below its value in the unforced case, more so in the $St = 0.4$ case. It should be noted that the details of these results also depend upon the box size. Because the forced jets are still highly asymmetric at the outflow boundary, the numerical differences between the peaks in valley would increase if more downstream data were available.

*Streamwise mass flux*

The net entrainment of the jet can be studied by computing the streamwise mass flux. Because $v_x$ is negligible at $r = 10r_o$, this is equivalent to

$$\mathcal{F}(x) = \int_0^{2\pi} \int_0^{10r_o} \overline{\rho v_x} \, r \, dr \, d\theta, \qquad (0.4)$$

which is plotted in figure 0.15. The mass flux in the unforced case grows slowly at first, where the shear layers are laminar and disturbances are small, and then grows more rapidly starting at

46
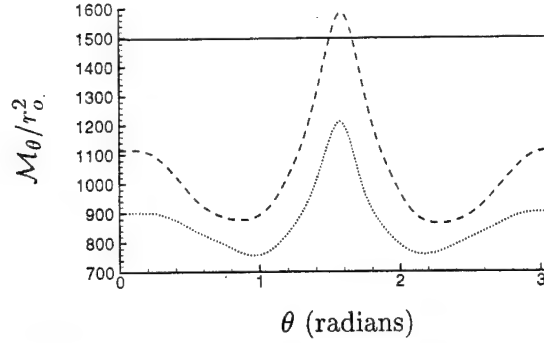
Figure 0.14: Planar integrals of $\xi^6$ from (0.3): —— unforced; ---- $St = 0.2$; ········ $St = 0.4$.
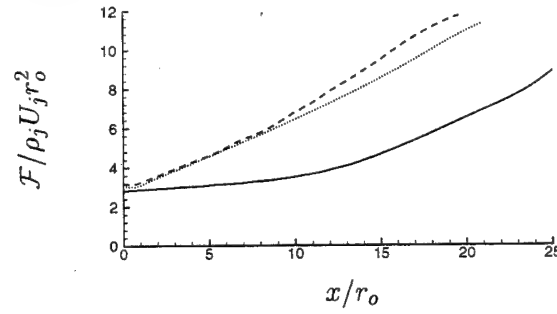


Figure 0.15: Streamwise mass flux from (0.4): —— unforced; ---- $St = 0.2$; ········ $St = 0.4$.

around $x = 14r_o$ where the potential core closes. The mass fluxes in the forced cases both grow rapidly from the start and are over twice at high by $x = 20r_o$. Forcing at $St = 0.2$ is only mildly more effective at increasing the mass flux than forcing at $St = 0.4$. It is seen that the fluxes are slightly different for the three cases at $x = 0$. This is because of the fluid added by the actuators and entrainment caused directly by their action.

*Scalar dissipation*

The rate of scalar dissipation can also provide an important measure of mixing which is particularly relevant in combustion applications. In figure 0.16, we consider planar integrals of $|\nabla \xi|$ as a function of downstream distance,

$$\mathcal{D}(x) = \int_0^{2\pi} \int_0^{10r_o} |\nabla \xi|\, r\, dr\, d\theta. \tag{0.5}$$

$\mathcal{D}(x)$ for the $St = 0.4$ case starts to rise closer to the nozzle, but the curve for $St = 0.2$ forcing follows only $2r_o$ further downstream and becomes 50 percent greater by the right side of the domain. The total dissipation in the computational domain is clearly larger for $St = 0.2$ forcing. Based on the data at $x = 20r_o$, this trend is likely to continue downstream.

# Conclusion

Simulations of jets forced with high amplitude actuation reproduced experimental observations of similarly forced jets. Visualizations showed dramatic effect of this forcing on the jet. Forcing at
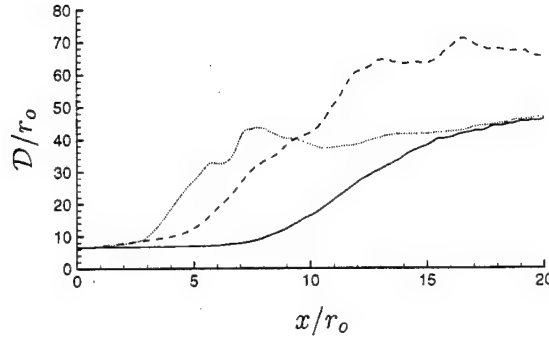
Figure 0.16: Planar integrals of $|\nabla\xi|$ from (0.5): —— unforced; ---- $St = 0.2$; ········ $St = 0.4$.

$St = 0.2$ excited the jet column into a distinct flapping mode. When forced at $St = 0.4$, the most amplified frequency in the unforced jet, the large structures appeared closer to the nozzle. However, despite the rapid initial spreading of this jet, forcing at $St = 0.4$ was not as effective at spreading the jet and mixing it (by most measures) with the ambient flow downstream. Mean axial velocities showed that the jet becomes highly non-axisymmetric in both forced cases and that the potential core length was reduced more by $St = 0.2$ than $St = 0.4$ forcing.

Mixing was quantified by several different metrics. Point measurements of scalar concentration on the jet axis showed that forcing at $St = 0.2$ was more effective at reducing centerline scalar concentration. However, volume integrals of $\xi^n$ over the computational domain (for $n = 4$ or $6$) were smaller when the jet was forced with $St = 0.4$. This was primarily due to the faster response of the jet to forcing at this frequency. Consideration of planar integrals of $\xi^6$ and $|\nabla\xi|$ as a function of $x$ suggested that forcing at $St = 0.2$ would be more effective for mixing further downstream. Forcing at both Strouhal numbers increased streamwise mass flux considerably over the unforced case, with $St = 0.2$ forcing performing marginally better in this regard than $St = 0.4$ forcing.

# Bibliography

[1] M. Samimy, K. B. M. Q. Zaman and M. F. Reeder, "Effect of tabs on the flow and noise field of an axisymmetric jet," AIAA J. **31**, 609 (1993).

[2] M. F. Reeder and M. Samimy, "The evolution of a jet with vortex generating tabs: real-time visualization and quantitiative measurements," J. Fluid Mech. **311**, 73 (1996).

[3] E. K. Longmire, J. K. Eaton and C. J. Elkins, "Control of jet structure by crown-shaped nozzles," AIAA J. **30**, 505 (1992).

[4] R. W. Wlezien and V. Kibens, "Influence of nozzle asymmetry on supersonic jets," AIAA J. **26**, 27 (1988).

[5] A. Krothapalli, J. McDaniel and D. Baganoff, "Effect of slotting on the noise of an axisymmetric supersonic jet," AIAA J. **28**, 2136 (1990).

[6] K. M. B. Q. Zaman, "Spreading characteristics of compressible jets from nozzles of various geometries," J. Fluid Mech. **383**, 197 (March 1999).

[7] D. E. Parekh, V. Kibens, A. Glezer, J. M. Wiltse and D. M. Smith, "Innovative jet flow control: mixing enhancement experiments," AIAA Paper 96-0308 (1996).

[8] C.-M. Ho and P. Huerre, "Perturbed free shear layers," Ann. Rev. Fluid Mech. **16**, 365 (1984).

[9] C. R. Koch, M. G. Mungal, W. C. Reynolds and J. D. Powell, "Helical modes in an acoustically excited round jet," Phys. Fluids A **1**, 1429 (1989).

[10] C.-M. Ho, Y. Zohar, J. K. Foss and J. C. Buell, "Phase decorrelation of coherent structures in a free shear layer," J. Fluid Mech. **230**, 319 (1991).

[11] G. McKinney, Air Force Office of Scientific Research Publication: Research Highlights, Sept./Oct 1998 (also http://ecs.rams.com/afosr/afr/afo/any/text/any/afrrhoct.htm).

[12] B. L. Smith and A. Glezer, "The formation and evolution of synthetic jets," Phys. Fluids **10**, 2281 (1998).

[13] B. L. Smith and A. Glezer, "Vectoring and small-scale motions effected in free shear flows using synthetic fet actuators," AIAA Paper 97-0213 (1997).

[14] J. L. Stromberg, D. K. McLaughlin and T. R. Troutt, "Flow field and acoustic properties of a Mach number 0.9 jet at a low Reynolds number," J. of Sound and Vib. **72**, 159 (1980).

[15] J. B. Freund, "Noise sources in a low Reynolds number turbulent jet at Mach 0.9," submitted *J. Fluid Mech.* (1999).

[16] A. Michalke, "A survey on jet instability theory," Progress in Aerospace Sciences **21**, 159 (1984).

[17] J. B. Freund, P. Moin and S. K. Lele, "Compressibility effects in a turbulent annular mixing layer," Technical Report TF-72, Stanford University, Mechanical Engineering, Flow Physics and Computation Division (1997).

[18] S. K. Lele, "Compact finite difference schemes with spectral-like resolution," J. Comp. Phys. **103**, 16 (1992).

[19] T. Colonius, S. K. Lele and P. Moin, "Boundary conditions for direct computation of aerodynamic sound generation," AIAA J. **31**, 1174 (1993).

# Appendix C

## Optimization of Turbulent Jet Mixing

**A. Hilgers, P. Moin, and J. B. Freund**

# Appendix C
## Optimization of Turbulent Jet Mixing

**Summary**

We introduce an approach for controlling jet mixing that combines direct numerical simulation of an incompressible jet flow with stochastic optimization procedures. The jet is excited with helical and combined helical and axial actuations at the orifice. An objective function that measures the spreading of the jet evaluates the performance of the actuation parameters. The optimization procedure searches for the best actuation by automatically varying the parameters and calculating their objective function value. Solutions that lead to a pronounced spreading of the jet are found within reasonable time, although the evaluation of the objective function, the DNS or LES of the jet, is expensive. For a jet flow at low Reynolds number the performance of different search algorithms (simulated annealing and evolution strategies) is evaluated. We compare various objective functions based on radial velocity and the concentration of a passive scalar, including functions that penalize actuation with high amplitudes. We find that a combined axial and helical actuation is much more efficient with respect to jet mixing than a helical actuation alone.

# Introduction

The control of turbulent jet flows has applications in various fields such as combustion, aerodynamic noise and jet propulsion. In combustion processes it is important to enhance the turbulent mixing of the chemical species to make the process more efficient and reduce the concentration of pollutants. Acoustic emissions by aircraft jet engines can be reduced by controlling flow unsteadiness that produces noise. One aim of enhanced mixing in jet propulsion applications is to decrease the plume temperature and suppress infrared radiation.

The mixing rate of a turbulent jet can be significantly altered by applying a suitable excitation at the jet orifice. Since the external forcing interacts with the natural modes of the jet in a nonlinear way, it is not possible to predict which kind of actuation is optimal to increase mixing. Various experiments have been carried out that study the reaction of jets to the nozzle geometry (passive control [1]) and to external forcing (active control [2, 3, 4]). Different types of actuators such as piezoelectric devices and synthetic jets, have been tested [5, 6]. It has been shown that a large spreading of the jet can be achieved with a small mass flow actuation if suitable frequencies are chosen [6].

Numerical simulations of compressible and incompressible jet flows have been carried out that confirm many observations made in experiments with periodically forced jets [7, 8, 9, 10]. So far it is difficult to carry out a systematic search for the optimal forcing because the simulations are very computationally intensive. Evolution strategies have been first applied to the optimization of actuation parameters in jet mixing by Koumoutsakos et al. [11]. This work showed that evolution strategies are capable of finding suitable actuations for a vortex model and direct numerical simulations of compressible jets.

In this paper we perform a systematic search for helical and combined axial and helical forcing of a jet that maximize mixing, as determined by various cost functions. We combine automatic search strategies with direct numerical simulation (DNS) and large eddy simulation (LES) of a round jet. Varying the actuation at the orifice, we search for the forcing that maximizes the spreading of the jet. Large spreading corresponds to efficient mixing of a passive scalar, transported by the flow, with the surrounding air. The phase space of possible actuation parameters is searched automatically by a stochastic optimization strategy. While classical approaches like gradient methods converge rapidly, there is a risk of premature convergence to a local optimum. Stochastic methods avoid this by allowing steps in seemingly unfavorable directions with a certain probability. They are therefore useful for the optimization of multimodal functions. Among the stochastic methods proposed in the literature [12], simulated annealing and evolution strategies have been used for a large number of engineering optimization problems [13]. Simulated annealing [14, 15], also known as Monte Carlo annealing, is a serial procedure which is very efficient and straight forward. Evolution programs is the name for a group of strategies which make use of the principles of evolution - reproduction, mutation and selection - to find an optimal solution [16, 17, 18, 19]. They are easy to implement, efficient and inherently parallel. Examples for the application of evolution strategies to problems in fluid mechanics and first results for the optimization of jet mixing have been presented in [20]. In this paper, we will give a detailed description of the optimization procedure and compare the performance of different search strategies for the optimization of jet actuation. A fast convergence of the procedure is indispensable since the numerical simulation, which evaluates a given actuation,

is very computationally expensive. In order to compare the different strategies we have chosen a simple test case, a jet at low Reynolds number, for which the optimal solution is known.

## Direct Numerical Simulation of the Jet

The numerical solver simulates a free round jet issuing from a circular orifice of diameter $D$ in a solid wall. The incompressible Navier-Stokes equations and the transport equation for a passive scalar are solved in a spherical coordinate system, with $(r, \theta, \phi)$ denoting the radial, tangential and azimuthal directions (Fig. 1). Spatial derivatives are calculated on a staggered spherical grid. The time integration is carried out with a second order Adams-Bashforth method. More details of the numerical scheme can be found in Boersma [21]. The computational domain shown in Fig. 1 results from the intersection between the shell defined by the surfaces $r = 5D$ and $r = 15D$ and the cone starting from the center of the sphere with an opening angle of $36^o$. This geometry covers a domain with a streamwise extent of $10D$ and a spanwise diameter of $4D$ for the inflow section and $10D$ for the outflow section. Such a discretization is able to follow the streamwise spreading of the jet and to allow a well-balanced resolution of the flow field with a reasonable number of grid points.

At the inflow section, the following mean streamwise velocity profile is imposed

$$V_{z0}(r_c) = \frac{V_0}{2}\left(1 + tanh\left[0.25D/\Theta_0(D/(4r_c) - 4r_c/D)\right]\right),\tag{1}$$

where $V_0$ is the centerline velocity and $r_c$ is the radius in a *cylindrical system* $(z, r_c, \phi)$. The initial momentum thickness was $\Theta_0 = D/60$ in our simulations.

At the lateral boundary, the total normal stress is set to zero, which allows fluid exchange across the boundary. This condition properly simulates the entrainment of ambient fluid in the spreading jet flow. A so-called convective boundary condition (Orlanski [22]) is used to evacuate the vortex structures through the downstream boundary. This condition is numerically stable but physically not very realistic in elliptic flows like the jets described here. However, the convective nature of the homogeneous jet flow ([23]) allows the eventual removal of spurious disturbances.

For the DNS of a jet with Reynolds number $Re = 1500$, based on orifice velocity $V_0$ and diameter $D$, the spherical grid consists of $192 \times 128 \times 96$ points in the radial, tangential and azimuthal directions respectively. Typical CPU times for the calculation of a fully developed jet are 1200 node hours on an Origin 2000, using the Message Passing Interface (MPI). The optimization requires the simulation of approximately 150 jets for different actuation parameters. We will show in in this paper how we have reduced the CPU time during the optimization process.

In unforced jets, large coherent structures are observed that are related to the instability modes of the jet. The dominant modes are the axisymmetric or varicose mode and helical modes. The axisymmetric mode causes the shear layer to roll up into vortex rings. By applying axial forcing to the shear layer, the frequency of vortex ring generation and the pairing of the vortex rings may be altered. The initial shear layer is able to amplify a large range of frequencies. The frequency $f$ which leads to the maximum amplification of the initial shear layer is called the natural frequency. It can be obtained by linear spatial instability analysis (Michalke [24], Ho and Huerre [25]). For an axisymmetric jet with the initial velocity profile given in Eqn. (1) it is $St_{\Theta_0} = f\Theta_0/V_0 = 0.018$. The frequency $f_p$ of the axial perturbation that produces the largest total amplification is called

the preferred mode of the jet. It corresponds to the frequency of vortices at the end of the potential core. This frequency has been determined by Crow and Champagne to be $St_p \approx 0.3$ [26]. However, other studies have found the preferred Strouhal number to vary between 0.25 and 0.5 [27, 28]. Mankbadi [28] observed for a round jet under axisymmetric forcing that mixing is enhanced if the forcing Strouhal number is equal to about twice the jet's preferred mode. It was also found that at high Strouhal numbers the momentum thickness is reduced along the jet.

Mixing can be increased significantly if axial and helical forcing are combined [2, 3, 6]. In the following we will denote the Strouhal numbers of axial and helical forcing with $St_a$ and $St_h$. Large spreading angles (up to 80°) have been observed for certain ratios $\beta$ of the Strouhal numbers $St_a$ and $St_h$ [4]. In particular, the jet splits into two branches for $\beta = 2$ (bifurcating jet) and into three branches for $\beta = 3$. For non-integer ratios $1.6 < \beta < 3.2$, vortex rings are shed in different directions (blooming jet). It has been discussed by Parekh et al. [4] that these flow patterns appear for both low and high Reynolds numbers.

In our simulation the actuation of the shear layer was achieved by superposing periodic disturbances on the initial velocity profile. We have used two kinds of actuation. For the first, the total inflow velocity in the $z$ direction of a cylindrical coordinate system $(z, r_c, \varphi)$ is

$$V_z(r_c, \varphi, t) = V_{z0}(r) \left[ 1 + A_h sin \left( 2\pi St_h \frac{V_0}{D} t \right) cos(\varphi) \frac{2r_c}{D} \right]. \tag{2}$$

$A_h$ is the amplitude of the actuation which is phase-locked in the plane $\varphi = 0$. It corresponds to the superposition of two counter-rotating helical modes of the same frequency. It has been observed in simulations and experiments that this type of actuation causes the jet to perform a flapping motion in the plane of actuation. The second type of actuation is a superposition of axial and helical modes

$$V_z(r_c, \varphi, t) = V_{z0}(r) \left[ 1 + A_a sin \left( 2\pi St_a \frac{V_0}{D} t \right) + A_h sin \left( 2\pi St_h \frac{V_0}{D} t + \alpha \right) cos(\varphi) \frac{2r_c}{D} \right]. \tag{3}$$

Here $A_a$ and $A_h$ are the amplitudes of the axial and helical mode and $St_a, St_h$ are the respective Strouhal numbers. We have again chosen the helical part of the actuation to be phase locked in the plane $\varphi = 0$. The angle $\alpha$ determines the plane of spreading. The actuation Eqn. (3) with $\beta = St_a/St_h = 2$ has been used before to model bifurcating jets [21]. To simplify the notation, we will refer to jets obtained with the dual-frequency actuation Eqn. (3) as bifurcating jets if $\beta$ takes on a value that is approximately two. In the following sections we will investigate which parameter vector $\mathbf{x} = (St_a, St_h, A_a, A_h)$ maximizes the spreading of the jet.

## Optimization Strategies

The optimization problem is described by a vector of parameters that are varied during the procedure, and an objective function that evaluates the performance of the parameters. In the following, we will use the terminology of evolution programs. We will refer to the objective function as fitness function, to its value after evaluation as fitness value, and to the surface that describes the fitness value as a function of the parameters as fitness landscape. We will call the sequence of parameter vectors that are evaluated during the optimization procedure a search trajectory. For our optimization problem, the parameter vector consists of the Strouhal numbers and amplitudes of the

actuation. The objective function measures the spreading of the jet by performing a direct numerical simulation of the jet flow. The fitness landscape hence describes how jet spreading depends on the frequencies and amplitudes of the actuation.

For problems with unimodal fitness landscapes, classical optimization strategies like the gradient method are very efficient. For problems with multimodal fitness landscape however there is a risk for deterministic methods to converge to a local optimum (so-called premature convergence). Stochastic methods do not always follow the gradient during the optimization process, but instead allow large search steps as well as steps in directions that may have a worse fitness value with a certain probability. This enables the search trajectory to leave a local optimum. On the other hand, these methods usually require large numbers of iterations when compared with deterministic gradient-based methods. The dynamic behavior of the jet is determined by the nonlinear interaction of different modes. This is likely to cause a complicated dependence of the jet development on the actuation parameters. We therefore expect the objective function to be multimodal, which suggests that stochastic procedures are the method of choice for optimization of jet mixing.

Our approach of optimizing jet mixing implies that for each search step a direct numerical simulation of the jet flow has to be performed, which is very expensive. Even when various approximations to reduce the CPU time and parallel processing of the jet code are used, the total number of jet flow calculations that can be achieved is of the order $100 - 200$. For most optimization problems, typical numbers of objective function evaluations are of the order of $10^3 - 10^5$. A rapid convergence of the search is therefore indispensable.

We will compare the following optimization procedures: a simulated annealing algorithm, implemented by Goffe *et al.* [29], a single-membered and a multi-membered evolution strategy with Covariance Matrix Adaption of the steplength [30], both implemented by Koumoutsakos and Müller [20]. The single-membered evolution strategy corresponds to a simple stochastic search, which only accepts steps that lead to an improved fitness value, while the simulated annealing algorithm allows uphill movement to some extent (for a minimization problem). Both methods are serial and use step length adjustment based on the fraction of successful steps. The multi-membered evolution strategy operates on larger populations of individuals and evaluates multiple trajectories in parallel. It includes a refined step length adaption scheme which makes use of the whole search path rather than just the number of successful trials.

## Evolution strategies

Evolutionary computation techniques employ operations inspired by biological principles such as a reproduction cycle, natural selection and diversity by variation, to identify the optimal solution. Examples are genetic algorithms [16], evolutionary programming [18] and evolution strategies (ES) [19]. It has been shown by Koumoutsakos et al. [11] that evolution strategies are well suited for the optimization of jet actuation.

Evolution strategies operate on populations of individuals which represent possible solutions of the given problem. Each individual consists of a vector $\mathbf{x}$ containing $n$ parameters and an associated vector $\mathbf{s}$ containing $n$ mutation steplength. The number of parents in each generation is $\mu$, the number of offspring is $\lambda$, with $\lambda > \mu$. Starting from an initial generation of $\mu$ parents, the

offspring are generated by mutation

$$\mathbf{x}_o^{i+1} = \mathbf{x}_p^i + \mathbf{s}_p^i N(0,1).$$ (4)

Here, the indices $p$ and $o$ denote parent and offspring and $i$ is the number of the generation. $N(0,1)$ is a normal distributions with zero average and unit variance. We impose certain limits to the $n$ parameters. The amplitudes must be positive and the Strouhal numbers should be within a certain interval (see below). In our optimization, a mutation step that leads to a value outside the allowed range is considered unsuccessful and repeated until allowed values are obtained. If several repetitions of the mutation step fail, the parameters are defined randomly within the given limits.

After $\lambda$ offspring have been generated, their fitness values are determined and the best $\mu$ individuals are selected. The steplengths of the mutation are decreased if the offspring are better than the parents, otherwise they are increased. The $\mu$ best individuals, i.e. the vectors of the best parameters and the corresponding mutation steplengths are used as parents for the next generation. The best individuals are chosen among the offspring (($\mu, \lambda$) strategy) or among the $\mu + \lambda$ parents and offspring (($\mu + \lambda$) strategy) [31]. The $\mu$ best individuals, i.e. the vectors of the best parameters, may also inherit their associated mutation steplength. The simplest and earliest version of the evolution strategy [19] describes a population consisting of just one parent and one offspring and is referred to as $(1 + 1)$ strategy. It corresponds to a stochastic search which accepts a new solution only if it has a better objective function value than the previous. It uses a step length adjustment based on the ratio of the number of successful to the total numbers of trials. The use of several search trajectories allows the simultaneous evaluation of different optima and therefore can speed up the search significantly. Hansen et al. [30, 32] have shown that higher convergence rates can be achieved using the Covariance Matrix Adaptation scheme (CMA). With this method, the step sizes are adapted by considering the length of successful mutation steps not only of the last but rather of a number of previous generations. The CMA of step sizes makes use of correlations between consecutive steps. If successive mutation steps are positively correlated, they should be replaced by one larger step. If the correlation is negative, the steps partly cancel and should be replaced by a shorter step. The procedure is thus most efficient if there is no correlation between consecutive steps, which means that they are orthogonal. In order to achieve this, an evolution path is calculated as the sum of weighted steplength. From the evolution path a covariance matrix is obtained, which is used to turn the mutation vector in the most promising direction. The adaption of the evolution path takes place on a rather large time scale. In order to allow fast changes of the step lengths, a global step length is introduced which changes on a short time scale. A further speed-up is achieved by combining the CMA-ES with an intermediate recombination that averages the variable vector elements of some of the parents [30]. Details of the CMA-ES strategy can be found in [30]. The search is terminated if either the improvement made during the search gets smaller than a certain value or if a maximum number of function evaluations is reached.

## Simulated Annealing

Simulated annealing is based on the analogy between the annealing of solids, i. e. the way in which a solid cools and freezes into a crystalline structure with minimal energy, and the problem of solving large optimization problems. The algorithm, first proposed by Kirkpatrick *et al.* [14] is easy to

57

implement and very efficient. It employs a random search which does not only accept changes that improve the objective function $f$, such that $\Delta f = f(\mathbf{x_{n+1}}) - f(\mathbf{x_n}) < 0$ in a minimization problem. It also accepts an increase $\Delta f > 0$ with probability

$$p = \exp\left(-\frac{\Delta f}{T}\right),\tag{5}$$

where $T$ is the 'system temperature' which is high in the beginning of the annealing process and approaches zero towards its end. Eqn. (5), known as the Metropolis criterion [33], determines the amount of uphill movement that is allowed. The optimization procedure consists of a sequence of 'temperatures' $T$. At each $T$, a random search with a fixed number of search steps (a Markov chain of certain length) is generated, where new parameter vectors are obtained similar to Eqn. (4). If no better solution has been found at the end of the chain, the start parameters of the search are kept as initial points for the search at the next $T$. The parameter $T$ ensures that at the beginning of the search steps are possible that lead to a worse objective function value, which enables the trajectory to leave a local optimum. At the end of the search, when the vicinity of the global optimum is reached, the probability of accepting a worse solution is very low to ensure rapid convergence to the optimum. As rule for decrementing the temperature, the so-called annealing schedule, we have chosen an exponential cooling scheme [14]. The initial temperature was set such that the average probability for accepting a worse parameter vector is about 0.7 [34]. The steplength is again adjusted according to the successful number of trials.

## Jet Optimization

In this section, we describe the optimization procedure and compare the performance of the different algorithms. We have to choose an objective function which provides an effective measure of the spreading of the jet and which is sufficiently sensitive to changes in the actuation parameters. It is important to ensure that the evaluation of the objective function is possible within reasonable CPU times. We introduce two approximations that lead to a reduction of the CPU time: The evaluation of the objective function at an early stage of the jet simulation and the use of a coarse grid for these calculations. We investigate a test case, a jet at low Reynolds number $Re = 1500$, for which the phase space can be examined. First results for jets at higher Reynolds number, $Re = 6000$, are presented.

### Optimization Parameters

The actuation of the jet is described by the parameter vector $\mathbf{x}$. If the single-frequency actuation Eqn. (2) is chosen, the vector is two-dimensional and consists of the Strouhal number and amplitude $\mathbf{x} = (St, A_h)$. For the dual-frequency excitation Eqn. (3) the vector consists of two Strouhal numbers and two amplitudes $\mathbf{x} = (St_a, St_h, A_a, A_h)$, or $\mathbf{x} = (St_a, \beta, A_a, A_h)$ if the ratio of frequencies $\beta = St_a/St_h$ is used. The limits of the parameters have been chosen as follows. In laboratory experiments, bifurcating jets have been observed for $0.4 < St_a < 0.65$, $\beta = 2$ [4]. In experiments by Parekh et al. [6] that used an actuation similar to Eqn. (2) it was found that the most pronounced flapping of the jet appears for approximately $St_h = 0.2$. A large amplification of

signals was also observed for $St \approx 0.27$ and $St \approx 0.4$. Numerical simulations by Freund and Moin [8] have shown that flapping jets appear for $St_h = 0.2$ and $St_h = 0.4$, and that the lower Strouhal number is more efficient for jet mixing. This Strouhal number has also been found in the first attempts to find optimal actuation of a compressible jet with an evolution strategy [11]. We have varied the Strouhal numbers in a somewhat wider range $0.1 < St_h < 0.55$ for the single-frequency, and $0.1 < St_a < 1.2$ for the dual-frequency excitation. For the latter case, the ratio of Strouhal numbers was $1.6 < \beta < 3.2$.

In laboratory experiments jets are perturbed by acoustic forcing, in recent experiments and applications by piezoelectric devices or by suction and blowing of fluid near the jet orifice (synthetic jets). While acoustic actuation with high amplitude cannot be easily achieved, blowing and suction with a large mass flow is not practical and should therefore be avoided. In order to match this situation we need to search for an actuation that leads to a large spreading of the jet while maintaining a sufficiently low mass flow. In part of our optimization runs we have included this constraint by imposing an upper limit $A_h < 0.06$ and by introducing a suitable penalty term in the objective function.

## Choice of the Objective Function

The objective function measuring the spreading of the jet is based on quantities available by the DNS simulation: the velocity field, the scalar concentration and the pressure. The dependence of the radial velocity on the actuation parameters is pronounced, while the variation of the axial and azimuthal velocity is small and difficult to quantify. We have therefore maximized the integral of the radial velocity (in the cylindrical system)

$$f(\mathbf{x}, t_0) = \int_V v_{r_c}^2(r, \theta, \varphi, t_0)\, dV' \tag{6}$$

where $V$ is the computational domain as shown in Fig. 1. The integral of $v_{r_c}^2$ is time dependent. A suitable time $t_0$ must be chosen in the jet simulation for the evaluation of the objective function.

Besides (6) we have tested other objective functions. The distribution of the passive scalar corresponds directly to the amount of mixing in the jet. We have used the integral of the scalar transported to the outer part $\theta > \theta_0$ of the computational domain as an objective function

$$f(\mathbf{x}, t_0) = \int_V C(r, \theta, \varphi, t_0)\, dV' \tag{7}$$

where $C$ is the concentration of the scalar. We have also changed (6) by limiting the integral of $v_r^2$ to this subdomain. The best parameter vector produced by the optimization does not differ significantly for these different objective functions. On the other hand, if we calculate the integral of $v_r^2$ over the subdomain $10D < r \leq 15D$, the result differs from that found for the whole domain. The maximum of the objective function value is now located at lower Strouhal numbers. For low Strouhal numbers the mode that determines the creation of vortices saturates and is replaced by its subharmonic further downstream. The first pairing of vortices, which is the onset of the jet spreading, therefore happens further away from the orifice for small Strouhal numbers. The corresponding actuation leads to a lower fitness value when the whole domain is used for the integration of $v_r^2$.

Another possible objective function is the centerline velocity. While the integral of $v_r^2$ changes as a function of the parameter values early in the DNS, the centerline velocity does not show clear variations at that stage. Different objective functions have been investigated by Freund and Moin [8]. They showed that volume integrals of moments of the scalar concentration and integrals of the scalar dissipation are suitable metrics to quantify mixing in a jet.

Our computations have shown that the optimization strategy tends to choose at least one of the amplitudes to be as large as possible within the given limits. Since an actuation with very large amplitudes is not desirable, we have kept one of the amplitudes, usually $A_a$, constant for the dual-frequency actuation (3) and varied the ratio of amplitudes $A_h/A_a$. For the excitation with one frequency (2), we have introduced a penalty function

$$f(\mathbf{x}) = \int_V v_{r_c}^2 \, dV' - C \, A_h^2, \tag{8}$$

which seeks to maximize the spreading of the jet while minimizing the amplitude $A_h$. The constant $C > 0$ is chosen such that the two terms in (8) are of the same order of magnitude. If $C$ is very large the second term dominates the objective function such that the search results in very small amplitudes. If $C$ is on the other hand very small the effect of the penalty is negligible.

## Shape of the fitness landscape

The performance of optimization procedures is in general evaluated by applying them to well known test functions. In order to provide a suitable test function, we have chosen the case where the two Strouhal numbers were varied while the amplitudes were kept fixed. We were able to numerically obtain an image of the fitness landscape for a jet at low Reynolds number $Re = 1500$. For this purpose we calculated the fitness value on an equidistant grid in $(St_a, \beta)$ space (with $\beta = St_a/St_h$). As mentioned earlier, the typical CPU time for a full jet simulation is 1200 node hours. Since at least 200 evaluations of the objective function are necessary to identify the fitness landscape, the time for each evaluation needs to be reduced drastically.

Figure 2 shows how the objective function (6) evolves with time for the single-frequency actuation (2). The three curves correspond to different values of the axial Strouhal number at constant amplitudes $A_a = 0.025$, $A_h = 0.05$ and at $\beta = 2$. The time scale is the normalized scale of the jet simulation. (For comparison, the time scale of an excitation with $St_a = 0.7$ is $T = D/(StV_0) = 0.23$. The time for the DNS of a fully developed jet is approximately $t = 7$.) A comparison of the early stages of the simulation with the fully developed jets has shown that pronounced jet spreading corresponds to a large value of the objective function at these early times. We have therefore determined the fitness value of the parameter vector at time $t_0 = 1.6$ where the objective function values already clearly differ. Fig. 2 shows the objective function for the Strouhal number $St_a = 0.7$ that leads to a high value at $t = 1.6$ and for $St_a = 0.2$ and $St_a = 0.9$ that result in much lower values. The time scale shown in Fig. 2 is not proportional to the CPU time needed for the simulation. Note that the time integration of the DNS proceeds much faster at the beginning of the simulation, starting from a laminar flow. Calculating only the early stages of the jet development therefore leads to a large increase of the optimization speed.

In order to decrease the computational time, we have used a coarse grid for the optimization procedure. A comparison of calculations on different grids has shown that most of the small

scale structures are resolved on a $128 \times 96 \times 64$ or finer grid. The overall behavior of the jet, in particular at early stages of the simulation, however is captured by simulations on a coarser grid. The objective function shows a very similar behavior for early time $t < t_0$ on coarse and fine grids. We note that under-resolved simulations can only be used for a rough estimate of the jet dynamics, but since the jet flow is controlled by large scale structures, the overall dynamic is preserved by this approximation. Fig. 3 shows sketches of the fitness landscape, which have been obtained by calculating the objective function value, i.e. the value of (6) at time $t = t_0$, for an equidistant grid in $(St_a, \beta)$-space. This calculation has been performed in order to compare the fitness landscape for different grid size and to provide a test case for the optimization schemes.

In Fig. 3 a), the DNS was performed on a $128 \times 96 \times 64$ grid. The landscape shows a pronounced global maximum, which appears at the parameter values $(St_a, \beta) \approx (0.68, 2.0)$, as well as local maxima with lower amplitude at $(St_a, \beta) \approx (0.9, 2.8)$ and $(St_a, \beta) \approx (1.1, 3.5)$. These maxima are located on a straight line $\beta \approx 3 \cdot St_a$, which corresponds to a helical Strouhal number $St_h \approx 0.33$. In fact, most fitness values along this line are significantly higher than those in their vicinity. Another range of higher values can be seen for $St_a \approx 0.5$ and $\beta > 2$. For Fig. 3 b), a coarse grid $64 \times 64 \times 32$ has been chosen. Although the extrema are not as pronounced as in figure a), the landscape roughly has the same shape for simulation on this coarse grid. The global optimum appears again at $(St_a, \beta) \approx (0.7, 2.0)$ and there is a range of high values along the line $St_h \approx 0.3$. Using the approximations described in this section, the CPU time necessary for one evaluation of the objective function is approximately 3 node hours on a SGI-ORIGIN 2000. In fact, the optimization leads to good results while keeping the computational time within reasonable limits.

In the next section, we will use our knowledge of the fitness landscape to compare the performance of the different optimization procedures. Since the numerical estimation of the fitness landscape is computationally expensive, we have not repeated this procedure for other cases that were optimized – different parameters, different objective functions and higher Reynolds numbers. Instead, we assume that the test case chosen is representative for our optimization procedure.

## Results of the optimization

In this section we describe the results obtained by optimizing the objective function (6) for different actuation parameters. We present results for actuation using helical actuation at the jet orifice. Since we only varied one parameter, we used the simple $(1 + 1)$ evolution strategy. A combined axial and helical forcing has been optimized with simulated annealing and with a multi-membered evolution strategy. Using our knowledge of the fitness landscape described in the previous section, the performance of the optimization strategies is compared.

### One-frequency actuation

First, we varied only the Strouhal number of the actuation (2) and kept the amplitude fixed at $A_h = 0.05$. The optimization was done with the objective function (6) and the $(1 + 1)$ evolution strategy. Starting from an initial value $St_h = 0.5$, the evolution path was found to approach an optimum in the 27th generation (28 evaluations of the fitness function) at $St = 0.36$. We repeated

the calculation with an objective function that integrates $v_r^2$ only in the subdomain $10D < r \leq 15D$. This neglects spreading in the part of the computational domain close to the orifice and, therefore, favors lower Strouhal numbers. As a result of the optimization, we found $St = 0.28$. While Parekh *et al.* found the most intense motion of the jet for $St \approx 0.2$, they also observed efficient mixing at $St \approx 0.27$, which is close to our result, and at $St \approx 0.4$.

As mentioned in the previous section, the simultaneous optimization of Strouhal number and amplitude $A_h$ results in the maximum possible amplitude within the given limits. In order to keep the amplitude low we repeated the optimization with the function (8) that penalizes large amplitudes. The factor describing the weight of the penalty was chosen as $C = 5$ and the allowed range for the amplitude was $0.02 < A_h \leq 0.12$. Starting with the initial parameter vector $\mathbf{x} = (0.37, 0.05)$ for Strouhal number and amplitude, we found the maximum fitness value at $\mathbf{x} = (0.29, 0.08)$. If we choose a larger factor $C$, smaller amplitudes are preferred. For $C = 15$, the optimum is found at $\mathbf{x} = (0.30, 0.045)$. The Strouhal number is approximately the same for both values of $C$. In the literature of evolution programs sophisticated ways of dealing with multi-objective optimization problems have been proposed [35]. However, we have chosen the objective function as shown in Eqn. (8) for simplicity.

For the results described so far, the jet simulation was started at time $t = 0$ from the initial laminar flow at the orifice. The optimization has been repeated with an initial non-laminar velocity field, which was obtained from a jet simulation with small axial and random forcing. The parameter vector found by the evolution strategy did not differ significantly.

## Two-frequency actuation

It has been shown in many experiments that the combination of axial and helical actuation can lead to a high mixture fraction in the jet [2, 3, 9]. We will now present results that we obtained by optimizing the parameters of the dual-frequency actuation (3). Although this actuation contains four parameters, we varied only three of them in order to reduce the dimension of the search space. For most runs we kept the axial amplitude constant at $A_a = 0.025$ and optimized the parameter vector $\mathbf{x} = (St_a, \beta, A_h)$, $\beta = St_a/St_h$. Since we expected the search to be more difficult than for the variation of just one parameter, we used a $(\mu + \lambda)$ strategy with $\mu = 2$ parents and $\lambda = 5$ offspring and an adaption of the step length with the covariance matrix adaption scheme. Although this still corresponds to a small population, it increases the efficiency of the search while keeping the CPU time needed for the evaluation of each generation within reasonable limits. The limits for the parameters were chosen as described in section 2. In particular, we have set the upper limit for the helical amplitude to $A_h = 0.075$. Starting from the parameter vector $\mathbf{x}_{0,1} = (0.7, 2.2, 0.05)$ which corresponds to an objective function value $f(\mathbf{x}_{0,1}) = 2.19$ the best parameter vector $\mathbf{x}_{best} = (0.66, 2.1, 0.075)$ with fitness value $f(\mathbf{x}_{best}) = 3.12$ was obtained after 25 generations. We repeated the simulation with different limits for the helical amplitude $0.0075 \leq A_h \leq 0.075$ and a different start vector $\mathbf{x}_{0,2} = (0.5, 2.5, 0.0175)$ with $f(\mathbf{x}_{0,2}) = 1.38$, and reached the same optimum after 40 generation which corresponds to 201 evaluations of the objective function. For comparison, the objective function value of a jet simulation without actuation (laminar flow) is $f(\mathbf{0}) = 0.50$.

We have calculated the objective function value in the vicinity of the global optimum to estimate the sensitivity of the result to changes of the parameter vectors. We found that the objective function value drops to 98% if the parameters are changed by $\Delta St_a = 0.01$ and $\Delta\beta = 0.15$ (The

value of 98% has been calculated with respect to the total range of the objective function value found in our optimization, $f(\mathbf{x}) \in [0.50, 3.12]$.) Therefore errors larger than a few percent should be avoided in applications.

The results of the optimization described so far suggest that the search strategy always chooses the maximal allowed helical amplitude. While the objective function value grows with the amplitude, variations of $A_h$ do not have a large influence on the *shape* of the fitness landscape. In order to confirm this assumption we have repeated the calculation with the parameter vector $(St_a, \beta)$ and kept the amplitudes fixed at $A_a = 0.025$, $A_{h,1} = 0.075$ and $A_{h,2} = 0.05$ respectively. We found the global optima at $\mathbf{x}_{best,1} = (0.65, 2.0)$ and $\mathbf{x}_{best,2} = (0.66, 2.1)$, in agreement with the previous results. This confirms that the frequencies are the relevant parameters for the maximization of jet spreading for the amplitude range considered in this study. However, it has been shown in [28] that for axial forcing Strouhal numbers that enhance mixing are different at very low ($A < 0.01$) and at high forcing levels.

In order to test the interdependence of the two actuation frequencies, we tried to optimize the objective function separately for the two frequencies. We found that the location of the maximum differs in this case and that the corresponding fitness value is lower. The Strouhal numbers are thus not independent and should be optimized simultaneously. This result is not surprising because the spreading pattern of the jet is due to the interaction of the various modes in the jet.

Apart from the function (6) we used the integral of the scalar concentration (7) as objective function. We also changed the objective function by extending the integral of $v_r^2$ or the scalar not to the whole domain, but only to the outer part $\theta > \theta_0$. For all these choices the same optimal Strouhal numbers $(St_a, \beta) \approx (0.66, 2.1)$ were found. This shows that our optimization does not depend critically on the choice of the quantity (radial velocity, scalar concentration) measured by the objective function.

## Comparison of the optimization procedures

In order to compare the different search strategies for our test case, the optimization of the objective function (6) for the dual-frequency actuation (3) with two parameters $\mathbf{x}_0 = (St_a, \beta)$ and fixed amplitudes, we have started the optimization at different points in phase space. We determined whether the global optimum was found and the number of fitness function evaluations necessary to reach it. The optimization was done for our test case, the dual-frequency actuation (3) with two parameters $\mathbf{x}_0 = (St_a, \beta)$. The amplitudes were kept constant at $A_a = 0.025$ and $A_h = 0.05$ and the fitness value was calculated at $t_0 = 1.6$.

The starting points for the optimization procedure were chosen from a contour plot of the fitness landscape, shown in Fig. 4. They were close to the global maximum, close to a local maximum and far away from both. Using simulated annealing, the $(1 + 1)$ and the $(2, 5)$ evolution strategies, we have recorded the number of objective function evaluations necessary to reach the global optimum. This number determines the required CPU time which is the limiting factor for our calculations. We assume that the optimization has converged when the final fitness value is 98% of the maximal value at the global optimum or higher and if the actuation parameters are within the corresponding range as described in Sec. . The results of the optimization are summarized in table 1. In all cases, the global optimum was found. The listed numbers are lower than the total number of function evaluations carried out for each run: When the optimum has been reached the

63

procedure continues searching for better solutions and stops only if no improvement has been made for a large number of iterations. Note that for the $(2,5)$ strategy each generation corresponds to 5 evaluations of the objective function. On average, simulated annealing and the $(2,5)$ evolution strategy with covariance matrix adaption of the steplength were able to find the global optimum using a comparable number of function evaluations, the number being slightly lower for simulated annealing. The $(1+1)$ strategy on the other hand needed in general a larger number of steps. The fact that the number of function evaluations for the $(2,5)$ evolution strategy is not lower than that for simulated annealing indicates that the number of search steps that can be achieved for this computationally expensive problem is too small to allow efficient use of the information gathered on the search path. We have therefore used this method mainly for the less expensive optimization at low Reynolds numbers and simulated annealing for the optimization at higher $Re$ which will be presented in the next section.

For the start location $\mathbf{x}_0 = (0.65, 1.6)$ close to the global optimum, the $(2,5)$ ES and simulated annealing required 56 and 60 objective function evaluations. The reason for this is that a large initial step size was chosen for all strategies such that the vicinity of the initial point is not necessarily searched first. For the start location $\mathbf{x}_0 = (0.5, 2.5)$, both evolution strategies had difficulties finding the global optimum, requiring 201 fitness function evaluations even for the $(2,5)$ ES. Simulated annealing on the other hand needed 102 function evaluations when it was started from $\mathbf{x}_0 = (0.9, 2.8)$, in contrast to 31 evaluations for the $(2,5)$ ES.

Figure 5 gives an example for the convergence of the three optimization strategies. For the $(2,5)$ ES, the fitness value of the best offspring is shown as a function of the generation number. The resulting curve is not monotonic because the offspring are obtained by random mutation of the average parent vectors and therefore may have lower fitness values. For simulated annealing and the $(1+1)$ ES on the other hand, the best solution is kept until it is replaced by a better one. the best value found so far is shown as a function of the generation number.

| $\mathbf{x}_0$ | $(0.45, 3.1)$ | $(0.5, 2.5)$ | $(0.65, 1.6)$ | $(0.9, 2.8)$ | $(1.0, 2.0)$ | $(1.0, 3.2)$ |
|---|---|---|---|---|---|---|
| sim. annealing | 52 | 42 | 60 | 102 | 41 | 25 |
| (2,5) ES | 61 | 201 | 56 | 31 | 41 | 51 |
| (1+1) ES | 153 | 262 | 58 | 111 | 71 | 62 |

Table 1: Comparison of the optimization strategies: number of objective function evaluations required to reach the global optimum

## Simulation at higher Reynolds number using LES

For many applications of turbulent jet control, the Reynolds number of the flow is much higher than that used for the simulation presented so far. For the control of jets at higher Reynolds numbers we included a subgrid scale model in our simulation to keep the computational cost affordable. The idea of large eddy simulation (LES) is to resolve only the large scales of the flow while modeling the contribution of the small (subgrid) scales. The LES equations are obtained by applying a spatial filter to the momentum equations. In order to account for the subgrid-scale contribution to the flux of momentum the molecular viscosity is augmented by an eddy viscosity $\nu_t = C\Delta^2|\mathbf{S}|$, where $\mathbf{S}$ is

the subgrid strain tensor and $C$ the Smagorinsky constant. We have used a large eddy simulation (LES) based on the dynamic procedure by Germano *at al.* [36], which determines the constant $C$ as a function of space and time. The dynamic procedure does not contain any model constants.

We have used the combination of optimization algorithm and LES to search for actuation that maximizes mixing in a $Re = 6000$ turbulent jet. The simulations are more expensive than the DNS at $Re = 1500$ such that a numerical estimate of the fitness landscape is impossible. Instead, we use the conclusions drawn from our test case: We confine the search to the space of the two Strouhal numbers, assuming that they are the relevant parameters for control of jet mixing. The parameters were varied in the range $St_a \in [0.2, 1.2]$ and $\beta \in [1.6, 3.2]$ and the amplitudes were kept constant at $A_a = 0.025$ and $A_h = 0.075$. The optimization was performed with the simulated annealing algorithm, which on average needed the lowest number of objective function evaluations for the test case.

First, we compared simulations on grids with different resolution. We found that a grid with $160 \times 120 \times 32$ points in the radial, tangential and azimuthal direction respectively is small enough to allow repeated calculation of the objective function, while being sufficiently large to give a reliable estimate of the jet dynamics. Comparing the objective function (6) as a function of time for different parameter values, we have chosen the time for the evaluation of the function as $t_0 = 1.8$. The CPU time for one evaluation of the objective function was 32 node hours, as compared to 1800 node hours for the full LES on a $192 \times 128 \times 64$ grid.

Starting the search at $\mathbf{x}_0 = (St_a, \beta) = (0.66, 2.1)$ (the optimum for $Re = 1500$), the best value was reached at $\mathbf{x} = (0.79, 2.18)$ which corresponds to $(St_a, St_h) = (0.79, 0.36)$ after 52 evaluations of the objective function. Comparing the absolute fitness values we found that the maximum value reached at this Reynolds number is approximately 1.5 times higher than that for $Re = 1500$, suggesting that the spreading of the jet is larger for the $Re = 6000$ jet. Apart from the maximum at $\mathbf{x} = (0.79, 2.18)$ with fitness value $f = 5.0$ we found parameters with comparably high value at $\mathbf{x} = (0.90, 2.0)$ with $f(\mathbf{x}) = 4.9$ and $\mathbf{x} = (0.58, 2.6)$ with $f(\mathbf{x}) = 4.8$. The lowest value found was $f = 3.8$. In general the objective function values were higher for $St_a > 0.5$ than for lower Strouhal numbers. Apparently the fitness landscape has a structure that is different from that found for $Re = 1500$. In particular, high fitness values do not only appear at $St_h \approx 0.33$. Since we are only able to determine a small number of points on the fitness landscape, a guess of its structure is difficult. Like in most optimization problems there is no certainty about whether the global optimum has been reached. However, we have found a good solution within reasonable time.

## Discussion of the results

For the best actuation parameters found by the evolution strategies we have repeated the DNS of the jet on the fine grid described in the second section. Figs. 6 and 7 show the passive scalar concentration obtained when the helical actuation (2) is applied at the orifice. For the best Strouhal number $St_h \approx 0.36$, Fig. 6 shows snapshots taken at time $t = 9$ (on the normalized time scale of the jet). Different shades of grey denote different concentration $C$ of the scalar. The concentration is approximately one in the inner (dark) region and zero far outside (white region). The figure shows the jet in the plane of the actuation, $\varphi = 0$ (left), and in the plane $\varphi = \pi/2$ (right). The jet spreads rapidly in the plane of the actuation and contracts in the orthogonal plane. Although the

65

amplitude of the actuation is small ($A_h = 0.05$), the jet spreads at a large angle and the jet column shows a strong flapping motion. The jet column disintegrates towards the end of the computational domain, but regions of high concentration $C \approx 1$ remain near the centerline of the jet. Fig. 7 shows the best result obtained by maximizing the spreading in half of the computational domain. Since the optimal Strouhal number is smaller in this case, the jet spreads further downstream from the orifice than in the previous case.

Figure 8 shows a snapshot of the jet actuated with the parameters $\mathbf{x}_{best} = (St_a, St_h, A_h) = (0.66, 0.31, 0.075)$ and $A_a = 0.025$. This dual-frequency actuation leads to an impressive spreading of the jet. The center of the jet shows a strong flapping motion, which is due to the large amplitude of the helical forcing. Comparing Figs. 8, 6 and 7 we find that the shape of the jet differs for the three types of actuations. The overall spreading, i.e. the area, to which a significant amount of the tracer is transported, is comparable, although the total amplitude is smaller for the jets with single-frequency forcing. The flapping motion of the jet column however is most pronounced for the dual-frequency actuation. The jet column is completely dispersed near the end of the domain, indicating that the jet bifurcates. Although a clear spreading in two branches is not visible, there are areas on both sides of the centerline with much higher concentration of the scalar and much lower radial velocity (not shown) than on the centerline. For comparison we also show a natural jet, calculated for a slightly higher Reynolds number, in Fig. 9. A larger domain is chosen since the potential core is much longer in this case. The spreading angle of the jet is approximately $10°$. A quantitative comparison of the jets obtained by our simulation with the experimental results by Parekh *et al.* (1996) is difficult because the Reynolds numbers differ. In addition, different types of perturbation are used in the experiment and simulation, and hence spreading angles will always be slightly different.

In Fig. 10 a snapshot of the scalar concentration is plotted for a jet at $Re = 6000$ which was obtained using the actuation with the best Strouhal numbers $St_a = 0.79$ and $St_h = 0.36$ found for this Reynolds number. The flow was calculated on a grid with $192 \times 160 \times 64$ points. Again, a strong flapping motion of the jet column is visible. Apart from the large spreading of the jet it can be seen that the jet column disintegrates soon after the initial pairing. Further downstream the values of the scalar concentration are low, indicating good mixing in the jet.

The streamwise velocity and concentration of the scalar on the centerline of the jet is evaluated in order to obtain a more quantitative measure of turbulent mixing. It is known that the decay rate of round jets is proportional to $[z - z_0]^{-1}$ where $z_0$ is the virtual origin of the jet and $z$ the distance measured from the jet orifice [37]. The perturbations given by equations (2) and (3) are not axisymmetric and therefore linear decay of the jet is not expected. In Figure 11 (left) we show the centerline velocity obtained from the flapping and bifurcating jet computations. For comparison we include the profile for a round axisymmetric jet (standard jet) at comparable Reynolds number. For both the flapping and bifurcating jets the centerline velocity starts to drop near $z/D = 5$, which is much earlier than in the standard jet. The decay rate (slope of the curve in Fig. 11 (right)) of the flapping jet is comparable to that of the standard jet while the bifurcating jet decays much faster. For the flapping jet the decay is approximately linear, for the bifurcating jet superlinear.

In our simulation it can be assumed that for values of the scalar concentration $C \approx 0.5$ the flow is well mixed. In Fig. 12 we show the centerline scalar concentration for the bifurcating, the flapping and the natural jets. The actuation leads to a much earlier decay of concentration than

for the natural jet. For the flapping actuation, the concentration reaches $C \approx 0.4$ on the centerline at the end of the domain. For the bifurcating jet, the decay starts even earlier and the mixing is very efficient. Towards the end of the domain, the average concentration reaches low values due to the bifurcation of the jet, which transports the scalar away from the centerline.

Fig. 13 shows the total turbulent flux of the scalar $\sqrt{\overline{u_r' C'}^2 + \overline{u_z' C'}^2}$ in the plane of the actuation for both the flapping and bifurcating jet. For the flapping jet the flux has high values near the centerline. The bifurcating actuation on the other hand directs the total flux outwards. The bifurcating jet therefore has by far the best mixing properties. From the figures presented in this section it is clear that there is a certain amount of scatter in the DNS data which is due to the limited size of the statistical sample.

The main results of our optimization are summarized in table 2. In all cases, the spreading of the jet is most pronounced at helical Strouhal numbers $St \approx 0.3...0.36$. It differs from the natural Strouhal number, for which linear instability analysis predicts the largest amplification of signals (Michalke 1984), but is in agreement with the preferred frequency of the jet found by Crow *et al.* [26] and Mankbadi [28]. The optimal axial Strouhal number found by the optimization procedure is approximately twice as large as the preferred frequency, as predicted by Mankbadi [28]. The Strouhal numbers found are in very good agreement with experimental results by Lee *at al.* [2].

In the optimization procedure described in this paper some arbitrary choices have been made that may influence the results. The optimal parameter vector depends on the choice of the time $t_0$, at which the objective function value is determined. It also depends on the domain that is chosen for the integration of $v_r^2$ or in general on the length of the computational domain. However, for each choice of the domain actuation parameters were found that lead to a large spreading of the jet.

| $Re = 1500$ | | | | |
|---|---|---|---|---|
| | $St_a$ | $St_h$ | $A_a$ | $A_a$ |
| single-freq. actuation, eq. (2) | - | 0.36 | - | 0.05 (fixed) |
| single-freq. actuation, penalty $C = 5$ | - | 0.29 | - | 0.08 |
| two-freq. actuation, eq. (3) | 0.66 | 0.31 | 0.025 (fixed) | 0.075 |
| two-freq. actuation, separate opt. of $St_a, St_h$ | 0.72 | 0.29 | 0.025 (fixed) | 0.075 (fixed) |
| $Re = 6000$ | | | | |
| | $St_a$ | $St_h$ | $A_a$ | $A_a$ |
| two-freq. actuation, eq. (3) | 0.79 | 0.36 | 0.025 (fixed) | 0.075 (fixed) |

Table 2: Best actuation parameters found by the optimization strategies.

## Conclusions

In this paper we have combined stochastic search programs and numerical simulation of a jet to search for actuation parameters (Strouhal numbers and amplitudes) that enhance mixing in the jet. We have used different objective functions that evaluate the performance of a given actuation and found that the integral of the squared radial velocity and the integral of the concentration

of a passive scalar are suitable measures. Since jet flows are governed by the dynamics of the large eddies, we have used a coarse grid for the DNS and LES in the optimization procedure. We have found that the spreading of the jet and hence the amount of mixing depends very much on the actuation Strouhal numbers and that it grows with the amplitudes. The main result is that a bifurcating perturbation gives better mixing and a faster decay of the center line velocity and scalar concentration than a flapping perturbation. We found the most pronounced spreading for helical and axial Strouhal numbers $St_h \approx 0.3...0.36, St_a \approx 2 \cdot St_h$ at Reynolds number $Re = 1500$ and $Re = 6000$. The spreading of the jet as measured by our objective function is larger at the higher Reynolds number. For applications, it is necessary to have a large spreading not only in one plane but in the whole three dimensional domain. This can be obtained by replacing the phase-locked helical forcing used in our simulation by a helical actuation that is rotating around the orifice.

Stochastic optimization techniques appear to be very efficient for optimization of the jet actuation. Comparing different methods we have found that multi-membered evolution strategies and in particular simulated annealing are well suited for this problem. Although convergence to a local optimum can never be completely excluded, it can be stated that our strategy is able to find a good solution within reasonable time. In a real experiment the perturbation is not described by a simple mathematical function like in our simulation, and therefore a one to one comparison between simulation and experiment is difficult. However, we expect that the frequency range found to be best in our simulations is similar to that for experiments under comparable conditions. We also expect that stochastic search strategies can be used to optimize physical experiments. Future work will concentrate on the use of more realistic actuators and on simulations at higher Reynolds numbers.

## References

[1] P. J. Juvet and W. C. Reynolds, "Coanda-Controlled Jet Flow", *Bull. Am. Phys. Soc* **34**, 10, 2316 (Nov. 1989); R. W. Wlezien and V. Kibens, "Influence of nozzle asymmetry on supersonic jets", AIAA Journal **26**, 27 (1988).

[2] M. Lee and W.C. Reynolds, "Bifurcating and blooming jets", Report No. TF-22, Department of Mechanical Engineering, Stanford University (1985).

[3] D. Parekh, A. Leonard, and W. C. Reynolds, "Bifurcating of round air jets by dual-mode acoustic excitation", AIAA 87-0164 (1987).

[4] D. Parekh, A. Leonard, and W. C. Reynolds, "Bifurcating jets at high Reynolds numbers", Report Nr. TF-35, Department of Mechanical Engineering, Stanford University (1988).

[5] J. M. Wiltse and A. Glezer, "Manipulation of Free Shear Layers Using Piezoelectric Actuators", J. Fluid Mech. **249**, 261 (1993).

[6] D. Parekh, V. Kibens, A. Glezer, J. M. Wiltse, and D. M. Smith, "Innovative Jet Flow Control: Mixing Enhancement Experiments", 34th Aerospace Science Meeting, Reno, AIAA 96-0308 (1996).

[7] J. B. Freund and P. Moin. "Mixing enhancement in jet exhaust using fluidic actuators: direct numerical simulations" ASME: FEDSM98-5235 (1998).

[8] J. B. Freund and P. Moin. "Jet mixing enhancement by high amplitude fluidic actuation", in preparation.

[9] I. Danaila and B. J. Boersma, "Mode interaction in a forced homogeneous jet at low Reynolds numbers", Proceedings of the 1998 Summer Program, Center for Turbulence Research, Stanford University, 141 (1998).

[10] G. Urbin, C. Brun and O. Métais, "Large eddy simulation of three-dimensional spatially evolving round jets," in *11th Symposium on Turbulent Shear Flows*, Grenoble (1997).

[11] P. Koumoutsakos, J. B. Freund and D. Parekh. "Evolution strategies for parameter optimization in jet flow control." Proceedings of the 1998 Summer Program, Center for Turbulence Research (1998).

[12] E. H. L. Aarts, "Local Search in Combinatorial Optimization", Wiley, New York (1997).

[13] L. Davis and M. Steenstrup, "Genetic Algorithms and Simulated Annealing: an Overview", in *Genetic Algorithms and Simulated Annealing*, Morgan Kaufman Publishers, San Mateo, CA, 1, (1987).

[14] S. Kirkpatrick, C. D. Gerlatt, and M. P. Vecchi, "Optimization by Simulated Annealing", *Science* 220, 671 (1983).

[15] P. J. M. van Laarhoven, E. H. L. Aarts, "Simulated Annealing: Theory and Applications", D. Reidel: Dordrecht, (1987).

[16] J. H. Holland, "Adaption in Natural and Artificial Systems", The University of Michigan Press, Ann Arbor (1975).

[17] Th. Bäck, U. Hammel, and H.-P. Schwefel, "Evolutionary Computation: Comments on the History and Current State," *IEEE Transactions on Evolutionary Computation*, Vol. 1, No. 1 (1997).

[18] L. J. Fogel, A. J. Owens, and M. J. Walsh, "Artificial Intelligence through Simulated Evolution", Wiley, New York (1966).

[19] I. Rechenberg, "Evolutionsstrategie - Optimierung technischer Systeme nach Prinzipien der biologischen Evolution" Fromann-Holzboog, Stuttgart (1994); I. Rechenberg, "Evolutionsstrategie '94", Fromann-Holzboog, Stuttgart (1994).

[20] P. Koumoutsakos, S. Müller, A. Hilgers, J. Freund, and D. Parekh, "Evolution Strategies for Jet Mixing Optimization", IEEE Transactions on Evolutionary Computation (submitted).

[21] B. J. Boersma, G. Brethouwer, and F. T. M. Nieuwstadt, "A numerical investigation on the effect of the inflow conditions on a self-similar region of a round jet", Phys. Fluids **10**, 899 (1998).

[22] I. Orlanski, "A simple boundary condition for unbounded hyperbolic flows", J. Comp. Physics **21**, 251 (1976).

[23] P. Huerre, and P. Monkewitz, "Local and global instabilities in spatially developing flows", Ann. Rev. Fluid Mech, **22**, 473 (1990).

[24] A. Michalke, "Survey on jet instability theory", Prog. Aerospace Sci. **21**, 159 (1984).

[25] C.-M. Ho and P. Huerre, "Perturbed Free Shear Layers", Ann. Rev. Fluid Mech. **16**, 365 (1984).

[26] S. C. Crow and F. H. Champagne, "Orderly structures in jet turbulence", J. Fluid Mech. **48**, 547 (1971).

[27] A. K. M. Z. Hussain and K. B. M. Q. Zaman, "The 'preferred mode' of the axissymmetric jet", J. Fluid Mech., **110** (1981).

[28] R. R. Mankbadi, "The mechanism of mixing enhancement and suppression in a circular jet under excitation conditions", Phys. Fluids **28**, 2062 (1985).

[29] B. Goffe, M. Ferrier, and N. Rogers, "Global Optimization of Statistical Functions with Simulated Annealing", *Journal of Econometrics* 60, 65 (1994).

[30] N. Hansen and A. Ostermeier, "Convergence Properties of Evolution Strategies with the Derandomized Covariance Matrix Adaptation: The $(\mu/\mu_I, \lambda)$-CMA-ES", Proceedings of the 5th European Congress on Intelligent Techniques and Soft Computing (EUFIT'97), 650 (1997).

[31] H.-P. Schwefel, "Evolution and Optimum Seeking", John Wiley and Sons, New York, (1995); H.-P. Schwefel and T. Bäck, "Artificial Evolution: How and Why?", in *Genetic Algorithms and Evolution Strategies*, Ed. D. Quagliarella, John Wiley and Sons, New York, (1998).

[32] N. Hansen and A. Ostermeier, "Adapting Arbitrary Normal Mutation Distributions in Evolution Strategies: The Covariance Matrix Adaptation", Proceedings of the IEEE International Conference on Evolutionary Computation (ICEC'96), 312, (1996).

[33] N. Metropolis, A. .W. Rosenbluth, M. N. Rosenbluth, A. H. Teller, and E. Teller, "Equations of State Calculations by Fast Computing Machines", *J. Chem. Phys.* 21, 1087 (1958).

[34] S. Kirkpatrick, C. D. Gerlatt, and M. P. Vecchi, "Optimization by Simulated Annealing - Quantitative studies", *J. Stat. Phys.* 34, 975 (1984).

[35] D. Bestle, "Analyse und Optimierung von Mehrkörpersystemen", Springer, Berlin, 1993.

[36] M. Germano, U. Piomelli, P. Moin, and W. Cabot "Dynamic subgrid-scale eddy viscosity model", *Proceedings of the 1990 Summer Program*, Center for Turbulence Research, NASA/Stanford Univ., 5 (1990).

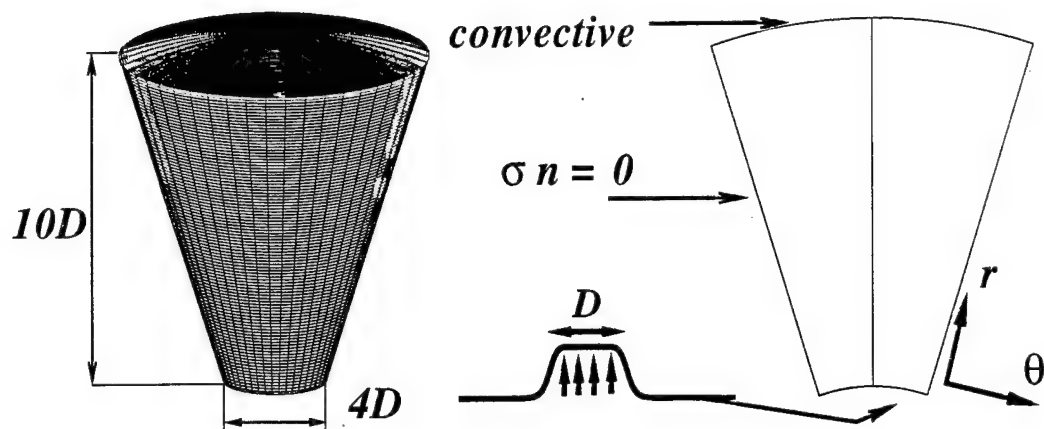[37] H. Schlichting, "Boundary Layer Theory", 7th. ed. (McGraw-hill, New York) (1979).
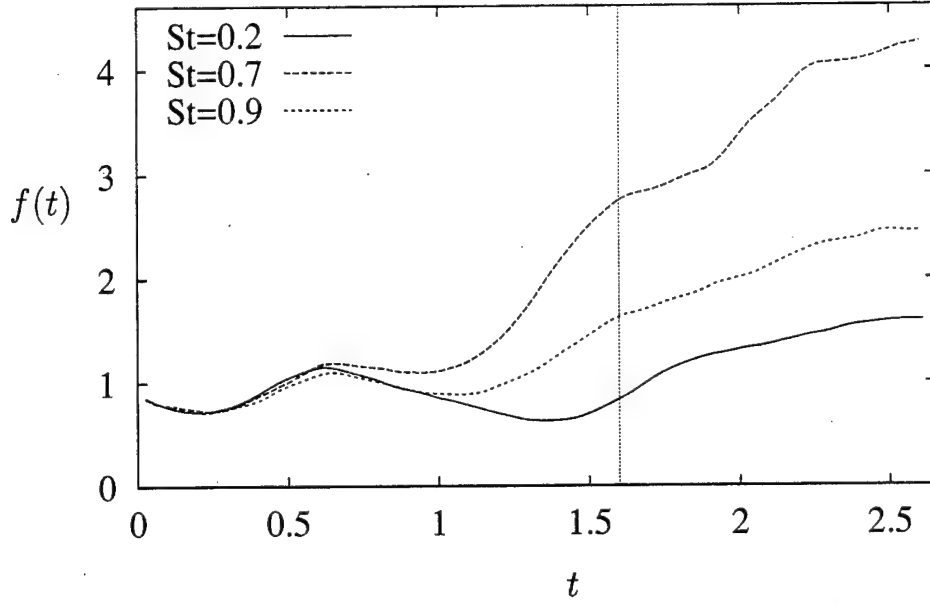
Figure 1: A sketch of the computational domain.

Figure 2: Objective function $f$ vs. time for a jet forced with dual-frequency excitation (2), $A_a = 0.025$, $A_h = 0.05$ and $\beta = 2$; the fitness value is determined at $t = 1.6$ ($128 \times 96 \times 64$ grid)
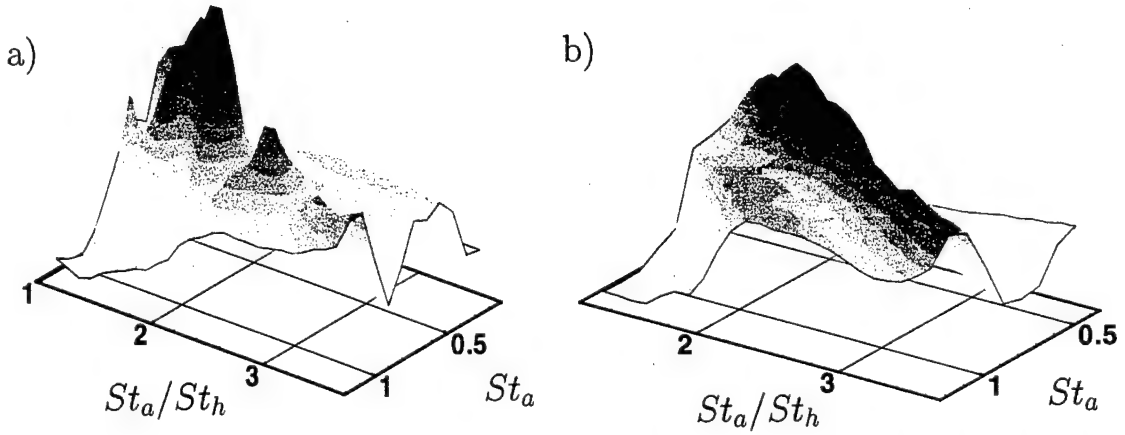


Figure 3: Fitness landscape for simulation on a a) $128 \times 96 \times 64$ and b) $64 \times 64 \times 32$ grid (fitness value in arbitraty units), $A_a = 0.025$, $A_h = 0.05$.
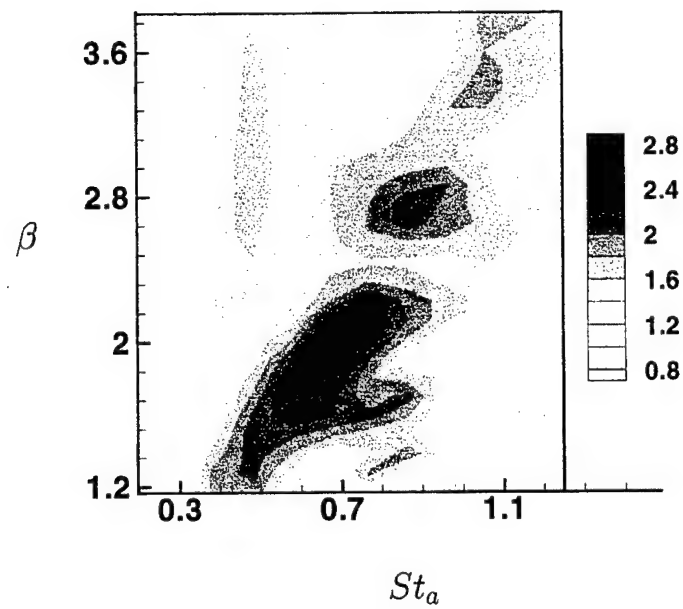
72

Figure 4: Contour plot of the fitness landscape for simulation on the $128 \times 96 \times 64$ grid, same parameter values as in Fig. 3
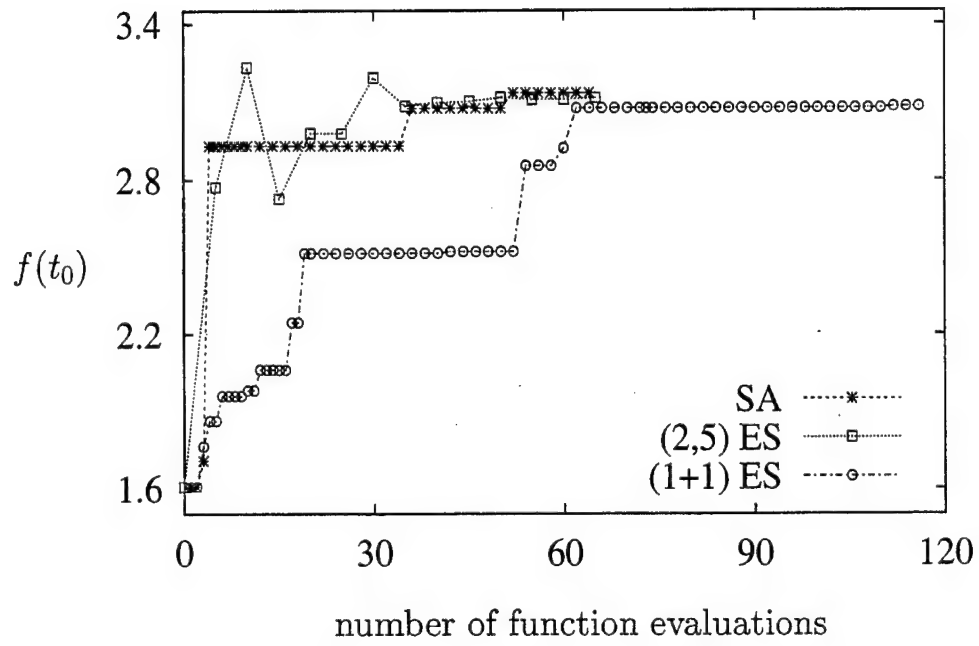
Figure 5: Convergence of the evolution strategies and simulated annealing (SA) for the parameter vector $\mathbf{x} = (St_a, \beta)$, $\mathbf{x}_0 = (0.45, 3.1)$, and $A_a = 0.025$, $A_h = 0.075$ fixed.
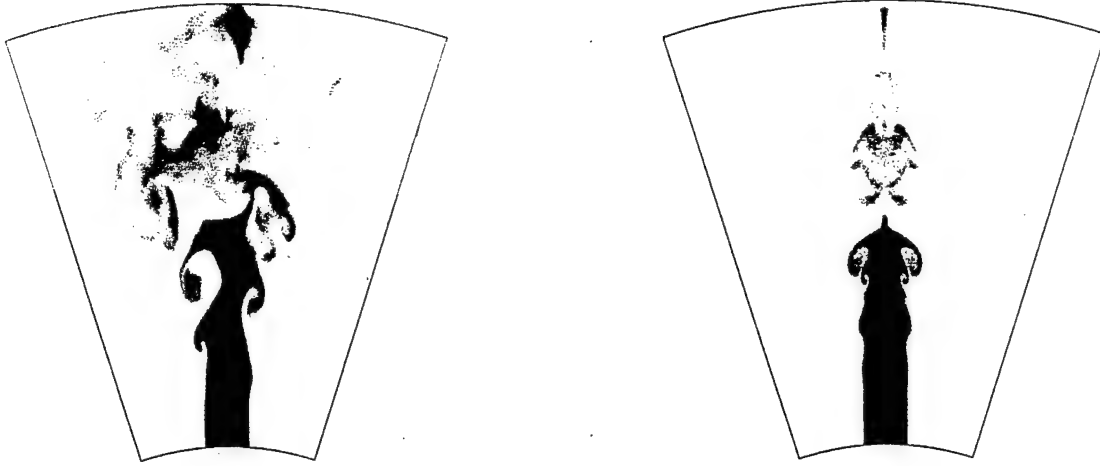
Figure 6: Snapshots of the passive scalar concentration at time $t = 9$ for a jet excited with the single-frequency actuation (2) in the plane of the actuation $\varphi = 0$ (left) and the plane $\varphi = \pi/2$ (right); $St = 0.036$ and $A_h = 0.05$; $Re = 1500$.
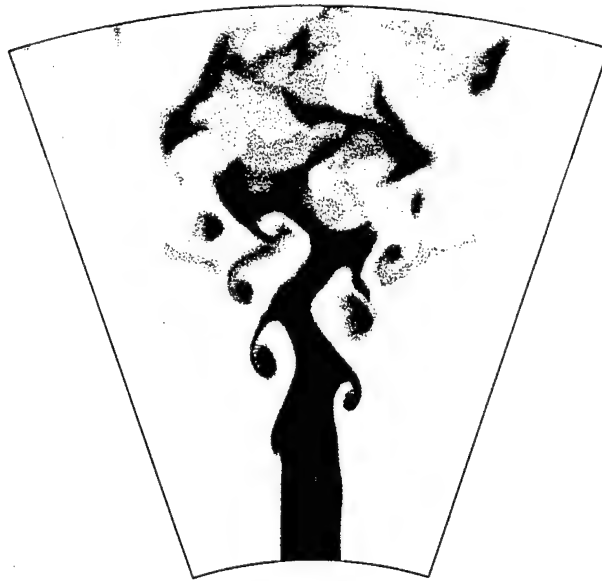


Figure 7: Snapshot of the scalar concentration at time $t = 7$ for a jet actuated with single-frequency actuation (2), $St = 0.028$ and $A_h = 0.05$; $Re = 1500$.

Figure 8: Snapshot of the scalar concentration at time $t = 7$ for a jet actuated with dual-frequency forcing (3) and $St_a = 0.66$, $St_h = 0.31$, $A_a = 0.025$, $A_h = 0.075$; $Re = 1500$.
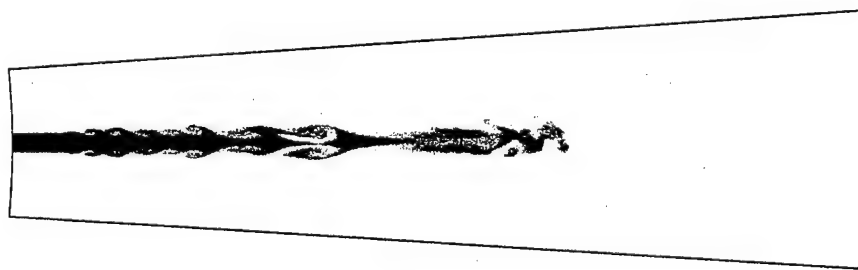


Figure 9: Snapshot of the scalar concentration of a natural jet without significant actuation, $Re = 2000$.
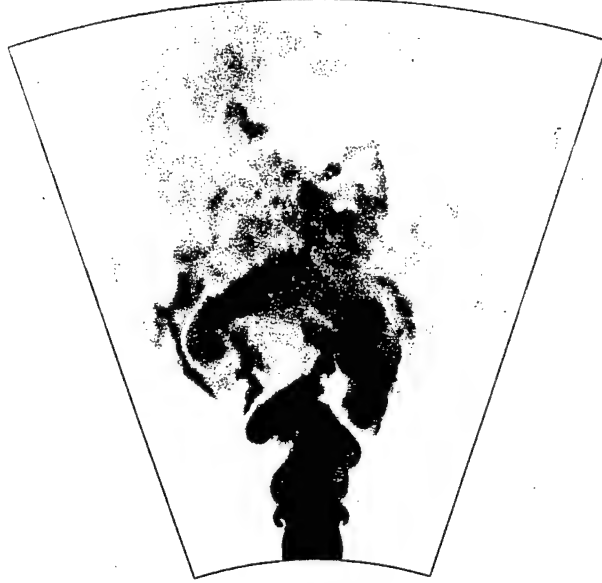
Figure 10: Snapshot of the scalar concentration at time $t = 8$ for a jet at $Re = 6000$, $St_a = 0.79$, $St_h = 0.36$, $A_a = 0.025$ and $A_h = 0.075$.
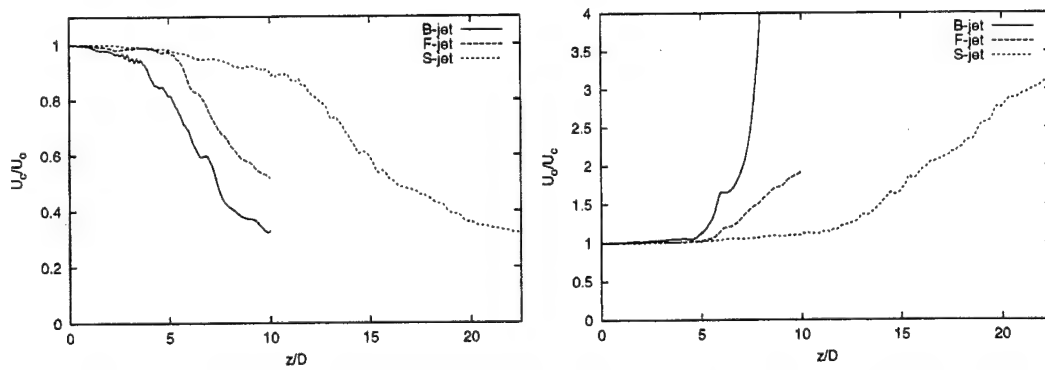


Figure 11: Left: The averaged centerline velocity for the bifurcating, flapping and standard jet. Right: The inverse of the centerline velocity for the flapping, bifurcating and standard jet.
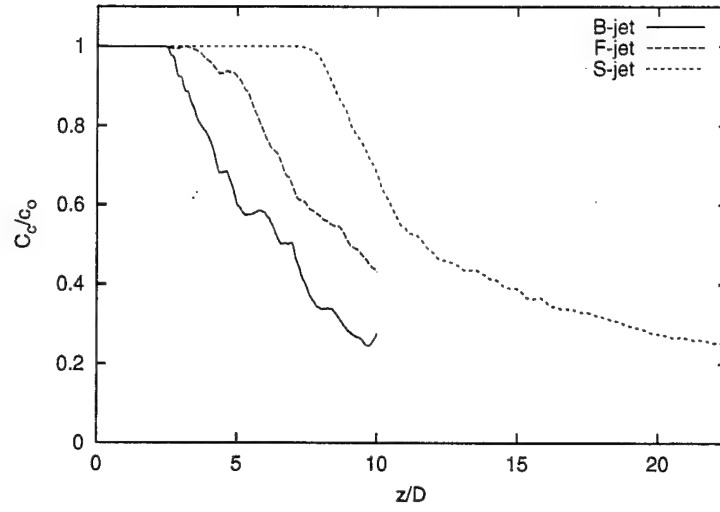
Figure 12: The averaged centerline scalar concentration for the flapping, bifurcating and standard jets.
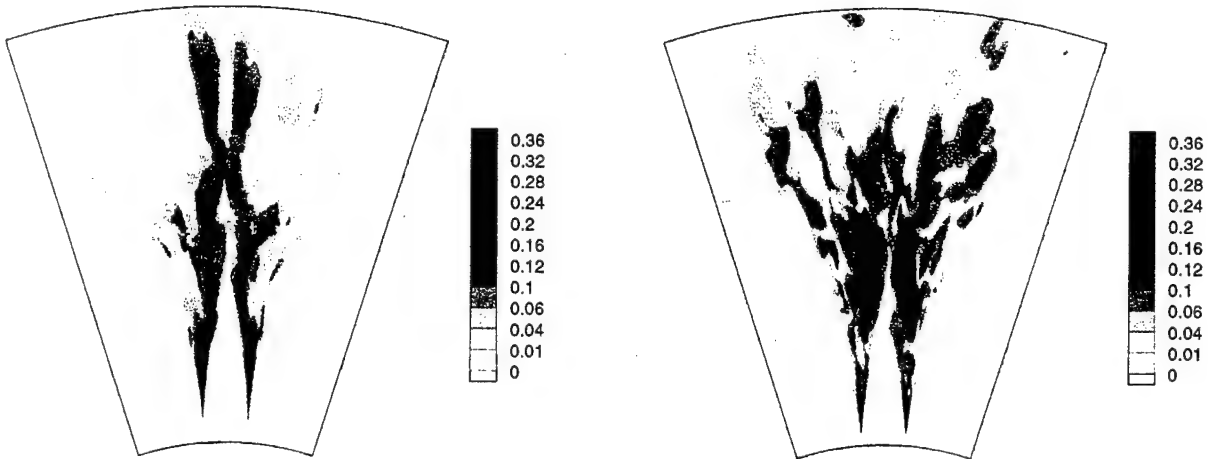


Figure 13: Isocontours of the turbulent flux ($\sqrt{\overline{u'_r C'}^2 + \overline{u'_z C'}^2}$) for the flapping and bifurcating jets in the plane of the actuation.

# Appendix D

## Instability Modes of Cylindrical Jet
## Based on Incompressible Inviscid Model:
## Piecewise Continuous Velocity Profile

### A. Pal

# Instability Modes of Cylindrical Jet
# Based on Incompressible, Inviscid Model;
# Piecewise Continuous Velocity Profile

Alex Pal[1]

Stability analysis of shear layers of parallel, incompressible, inviscid flows is discussed in Drazin and Reid.[2] For the solution of the resulting eigenvalue problem a numerical method is proposed by assuming a piecewise linear velocity profile. Even though the analysis assumes temporal instability, the method can be applied to the spatial instability problem as well. This memorandum proposes an analogous method for the axisymmetric jet.

In the axisymmetric case the stream function in the individual subregions of the flow (in the jet potential core, in the shear layer, outside the shear layer) can be expressed in closed form just as in the parallel flow case.

The resulting closed form dispersion equation connecting the normalized frequency $\omega$ and wave number $\alpha$ is in terms of modified Bessel functions of the radius. The use of these functions and the numerical approach recommended are discussed in the second half of this report.

## Governing equations

Similar to the planar case, discussed in Drazin and Reid, the following assumptions are made:

- The flow is incompressible, inviscid and axisymmetric.

- The flow is obtained by superposition of the mean flow consisting of a parallel flow of velocity $U(r)$ in the $x$-direction and an axially symmetric perturbation flow.

- The mean velocity is of the form

$$U(r) = \begin{cases} U_j & \text{if } 0 \leq r \leq r_1 \\ ar^2 + b & \text{if } r_1 < r \leq r_2 \quad {}^3 \\ U_\infty & \text{if } r_2 < r < \infty. \end{cases} \tag{1}$$

where the coefficients $a$, $b$ are determined so that $U(r)$ is continuous.

Let $\mathbf{Q} = U\mathbf{i} + \mathbf{q}$; $\mathbf{q} = u\mathbf{i} + w\mathbf{k}$ (i axial, k radial unit vector). Then

---

$$
\mathbf{Dq} = \begin{bmatrix} \dfrac{\partial u}{\partial t} + u\dfrac{\partial (U+u)}{\partial x} + w\dfrac{\partial (U+u)}{\partial r} \\[3mm] \dfrac{\partial w}{\partial t} + u\dfrac{\partial w}{\partial x} + w\dfrac{\partial w}{\partial r} \end{bmatrix}
$$

which leads to the momentum equations:

$$
\left( \frac{\partial}{\partial t} + U\frac{\partial}{\partial x} \right) u + w\frac{dU}{dr} = -\frac{\partial p}{\partial x} \tag{2}
$$

$$
\left( \frac{\partial}{\partial t} + U\frac{\partial}{\partial x} \right) w = -\frac{\partial p}{\partial r} \tag{3}
$$

Continuity equation in cylindrical coordinates

$$
\boxed{\frac{\partial u}{\partial x} + \frac{\partial w}{\partial r} + \frac{1}{r}w = 0.} \tag{4}
$$

Ansatz:

$$
u = \widehat{u}(r)\exp[i\alpha x - i\omega t]
$$

$$
p = \widehat{p}(r)\exp[i\alpha x - i\omega t]
$$

Stream function:

$$
\psi(t, x, r) = \widehat{\psi}(r)\exp[i\alpha x - i\omega t]
$$

The factor $\exp[i\alpha x - i\omega t]$ will be assumed and suppressed. The "$\widehat{\phantom{a}}$" notation will be omitted. The velocity components are then derivable for the stream function:

$$
u = \frac{1}{r}\frac{d(r\psi)}{dr} = \psi' + \frac{1}{r}\psi; \tag{5}
$$

$$
w = -i\alpha\psi \tag{6}
$$

Then (6) and (7) imply the continuity equation.

The pressure can be obtained directly from (2). Expressing $u$, $w$ in terms of $\psi$, (2) can be rewritten as

$$
\boxed{p = -(U-c)\left( \psi' + \frac{1}{r}\psi \right) + U'\psi} \tag{7}
$$

where $c = \omega/\alpha$

## Governing equation for the stream function

Substituting (6) and (7) into the momentum equation (3),

$$(U-c)\,\alpha^2\psi = -\frac{\partial}{\partial r}\left[-\left(U-\frac{\omega}{\alpha}\right)\left(\psi' + \frac{1}{r}\psi\right) + U'\psi\right]$$

or

$$(U-c)\left[\psi'' + \frac{1}{r}\psi'\right] - \left\{U'' + \alpha^2(U-c) - \frac{1}{r}U' + \frac{1}{r^2}(U-c)\right\}\psi = 0 \qquad (8)$$

## Matching conditions

### 1. Continuity of $w(r)$ :

From (8),

$$\frac{p}{(U-c)^2} = -\frac{d}{dr}\left(\frac{\psi}{U-c}\right) - \frac{1}{r}\frac{\psi}{U-c}$$

hence

$$\lim_{\epsilon\to 0}\left[\frac{\psi}{U-c}\right]_{r_i-\epsilon}^{r_i+\epsilon} = -\lim_{\epsilon\to 0}\int_{r_i-\epsilon}^{r_i+z}\left\{\frac{p}{(U-c)^2} + \frac{1}{r}\frac{\psi}{U-c}\right\}dr = 0$$

and therefore

$$\left[\frac{\psi}{U-c}\right]_{r_i-0}^{r_i+0} = 0 \qquad (9)$$

and since $U(r) - c$ is a continuous function of $r$,

$$[\,\psi\,]_{r_i-0}^{r_i+0} = 0 \qquad (9')$$

i.e., $\psi(r)$, and by (7), $w(r)$ must be continuous.

### 2. Continuity of $p(r)$ :

From Eq. (7)

$$\left[(U-c)\left(\psi' + \frac{1}{r}\psi\right) - U'\psi\right]_{r_i-0}^{r_i+0} = 0 \qquad (10)$$

or, considering the continuity of $\psi$,

$$\left[\frac{d}{dr}\left(\frac{\psi}{U-c}\right)\right]_{r_i-0}^{r_i+0} = 0 \qquad (10')$$

a relation similar to (6).

**Assumed velocity profiles:** Defined as in Eq. (1),

$U(r)$ is assumed continuous;

$U_j$, $U_\infty$ are known constants;

$a$, $b$ are constants determined from the continuity of the velocity profile $U(r)$. On the inner $(r = r_1)$ and outer $(r = r_2)$ boundaries of the shear layer

$$\left.\begin{array}{c} ar_1^2 + b = U_j, \\ ar_2^2 + b = U_\infty \end{array}\right\} \qquad (11)$$

respectively, from which

$$a = -\frac{U_j - U_\infty}{r_2^2 - r_1^2} \text{ and } b = \frac{r_2^2 U_j - r_1^2 U_\infty}{r_2^2 - r_1^2}. \qquad (12)$$

**Form of the perturbation $\psi(r)$ in the three subregions.** In each of the three subintervals $[0, r_1]$, $[r_1, r_2]$ and $[r_2, \infty]$, it was assumed that $U(r)$ is of the form

$$U = Ar^2 + B$$

where $A$ and $B$ are constant in each of the intervals. (In fact, $A = 0$ in the first and third intervals). Thus, the differential equation (8) incredibly simplifies to the same equation in the three intervals:

$$\psi'' + \frac{1}{r}\psi' + \left(-\alpha^2 - \frac{1}{r^2}\right)\psi = 0. \qquad (13)$$

This is Bessel's differential equation for the variable $i\alpha r$ and parameter value 1. The general solution of (13) is

$$\psi = C_1 \mathrm{J}_1(i\alpha r) + C_2 \mathrm{Y}_1(i\alpha r) = \widehat{C}_1 \mathrm{H}_1^{(1)}(i\alpha r) + \widehat{C}_2 \mathrm{H}_1^{(2)}(i\alpha r)$$

or, alternately,

$$\psi = c_1 \mathrm{I}_1(\alpha r) + c_2 \mathrm{K}_1(\alpha r)$$

where $\mathrm{I}_\nu(z)$ and $\mathrm{K}_\nu(z)$ are the modified Bessel functions defined by

$$I_\nu(z) \equiv e^{-i\nu\pi/2} J_\nu\left(e^{i\pi/2}z\right) \tag{14a}$$

$$K_\nu(z) \equiv \frac{i\pi}{2} e^{i\nu\pi/2} H_\nu^{(1)}\left(e^{i\pi/2}z\right) = -\frac{i\pi}{2} e^{-i\nu\pi/2} H_\nu^{(2)}\left(e^{-i\pi/2}z\right). \text{[4]} \tag{14b}$$

Since $\psi$ is bounded at $r = 0$ and is bounded and exponentially decaying as $r \to \infty$, and $\alpha$ is near real,

$$\psi(r) = \begin{cases} AI_1(\alpha r) & \text{if } 0 \le r \le r_1 \\ BI_1(\alpha r) + CK_1(\alpha r) & \text{if } r_1 \le r \le r_2 \\ DK_1(\alpha r) & \text{if } r_2 \le r < \infty \end{cases} \tag{15}$$

The functions $K_1(z)$ are many valued, but one branch of each is real if $z$ is real. These real branches will be used in the subsequent calculations.

**Application of the Matching Conditions.** Introducing Eqs. (15) into (6) and considering (11) yields

$$\left.\begin{aligned} AI_1(r_1\alpha) &= BI_1(r_1\alpha) + CK_1(r_1\alpha) \\ DK_1(r_2\alpha) &= BI_1(r_2\alpha) + CK_1(r_2\alpha) \end{aligned}\right\} \tag{16a,b}$$

Substituting (15) into (30) yields

$$\left.\begin{aligned} A(U_j - c) &\left[\left(\frac{d}{dr} + \frac{1}{r}\right) I_1(\alpha r)\right]_{r=r_1} \\ = B &\left[[U_m(r) - c]\left(\frac{d}{dr} + \frac{1}{r}\right) I_1(\alpha r) - 2ar I_1(\alpha r)\right]_{r=r_1} \\ + C &\left[[U_m(r) - c]\left(\frac{d}{dr} + \frac{1}{r}\right) K_1(\alpha r) - 2ar K_1(\alpha r)\right]_{r=r_1} \end{aligned}\right\} \tag{17a}$$

---

[4]    Encyclopedic Dictionary of Mathematics (EDM), V. 2, App. A, Table 19.IV,   Second Ed., MIT Press, 1993;  p. 1805.
Compare this with the only apparently more precise formuation of Abramowitz Stegun (A&S): Handbook of Mathematical Functions (Dover, 1965), Eq. 9.6.4.:

$$K_\nu(z) = \frac{i\pi}{2} e^{i\nu\pi/2} H_\nu^{(1)}\left(e^{i\pi/2}z\right) \qquad \left(-\pi < \arg z \le \frac{1}{2}\pi\right)$$

$$K_\nu(z) = -\frac{i\pi}{2} e^{-i\nu\pi/2} H_\nu^{(2)}\left(e^{-i\pi/2}z\right) \qquad \left(-\frac{1}{2}\pi < \arg z \le \pi\right)$$

$$D(U_\infty - c)\left[\left(\frac{d}{dr} + \frac{1}{r}\right)K_1(\alpha r)\right]_{r=r_2}$$

$$= B\left[[U_m(r) - c]\left(\frac{d}{dr} + \frac{1}{r}\right)I_1(\alpha r) - 2ar I_1(\alpha r)\right]_{r=r_2}$$

$$+ C\left[[U_m(r) - c]\left(\frac{d}{dr} + \frac{1}{r}\right)K_1(\alpha r) - 2ar K_1(\alpha r)\right]_{r=r_2} \qquad (17b)$$

where $U_m(r) = ar^2 + b$. The modified Bessel functions satisfy the recurrence relations

$$I_1'(z) + \frac{1}{z}I_1(z) = I_0(z)$$

$$K_1'(z) + \frac{1}{z}K_1(z) = -K_0(z) \qquad 5$$

Using these identities we find

$$\left(\frac{d}{dr} + \frac{1}{r}\right)I_1(\alpha r) = \alpha I_0(\alpha r); \quad \left(\frac{d}{dr} + \frac{1}{r}\right)K_1(\alpha r) = -\alpha K_0(\alpha r); \qquad (18a,b)$$

hence, one obtains from (17)

$$A(U_j - c)\left[\left(\frac{d}{dr} + \frac{1}{r}\right)I_1(\alpha r)\right]_{r=r_1}$$

$$= B\left[[U_m(r) - c]\left(\frac{d}{dr} + \frac{1}{r}\right)I_1(\alpha r) - 2ar I_1(\alpha r)\right]_{r=r_1}$$

$$+ C\left[[U_m(r) - c]\left(\frac{d}{dr} + \frac{1}{r}\right)K_1(\alpha r) - 2ar K_1(\alpha r)\right]_{r=r_1}$$

$$A(U_j - c)\alpha I_0(\alpha r_1)$$

$$= B[(U_j - c)I_0(\alpha r_1) - 2ar_1 I_1(\alpha r_1)] \qquad (19a)$$

$$+ C[-(U_j - c)\alpha K_0(\alpha r_1) - 2ar_1 K_1(\alpha r_1)]$$

where the identity $U_m(r_1) - c = U_j - c$ was used. Similarly,

---

5     EDM, same location

$$- D(U_\infty - c)\,\alpha K_0(\alpha r_2)$$

$$= B[(U_\infty - c)\alpha I_0(\alpha r_2) - 2arI_1(\alpha r_2)] \Bigg\}$$  (19b)

$$+ C[- \alpha(U_\infty - c)\,\alpha K_0(\alpha r_2) - 2ar_2 K_1(\alpha r_2)]$$

## The Dispersion Equation

Equations (16a,b) and (19a,b) can be written in the concise form

$$\mathbb{M}\mathbf{X} = 0$$  (20)

where $\mathbf{X} = [A\,B\,C\,D]^{\mathrm{T}}$ and

$$\mathbb{M} = \begin{bmatrix} I_1(r_1\alpha) & 0 & -I_1(r_1\alpha) & -K_1(r_1\alpha) \\ 0 & K_1(r_2\alpha) & -I_1(r_2\alpha) & -K_1(r_2\alpha) \\ V\alpha I_0(r_1\alpha) & 0 & -V\alpha I_0(\alpha r_1) + 2ar_1 I_1(\alpha r_1) & V\alpha K_0(\alpha r_1) + 2ar_1 K_1(\alpha r_1) \\ 0 & W\,\alpha K_0(\alpha r_2) & W\alpha I_0(\alpha r_2) - 2ar_2 I_1(\alpha r_2) & -W\,\alpha K_0(\alpha r_2) - 2ar_2 K_1(\alpha r_2) \end{bmatrix}$$

Here the abbreviations $(U_j - c) = V$ and $(U_\infty - c) = W$ have been used. The system
(20) has a nonzero solution if and only if the dispersion equation

$$\Delta(\omega, \alpha) \equiv \det[\mathbb{M}] = 0$$  (21)

is satisfied. The matrix $\mathbb{M}$ can be simplified by elementary row operations. $\mathbb{M}$ is found to
be row-equivalent to the matrix

$$\mathbb{M}' = \begin{vmatrix} I_1(r_1\alpha) & 0 & 0 & -\dfrac{1}{r_1\alpha I_0(r_1\alpha)} \\ 0 & K_1(r_2\alpha) & -\dfrac{1}{r_2\alpha K_0(r_2\alpha)} & 0 \\ V\alpha I_0(r_1\alpha) & 0 & 2ar_1 I_1(\alpha r_1) & 2ar_1 K_1(\alpha r_1) \\ 0 & W\alpha\,K_0(\alpha r_2) & -2ar_2 I_1(\alpha r_2) & -2ar_2 K_1(\alpha r_2) \end{vmatrix}$$  (22)

where the Wronski determinant identity

$$I_0(z)K_1(z) + I_1(z)K_0(z) = \frac{1}{z} \quad ^6$$

have been used. (Abel's theorem).

The dispersion equation $\det \mathbb{M} = \det \mathbb{M}' = \Delta(\omega, \alpha)$ is obtained by multiplying both sides by $r_1 r_2 \alpha^2 I_0(r_1 \alpha) K_0(r_2 \alpha)$, expanding the determinant and finally, simplifying by the same factor.

$$\tilde{\Delta}(\omega, \alpha) \equiv -r_1 r_2 \Delta(\omega, \alpha) \equiv$$

$$\left[ U_j - c + 2ar_1^2 I_1(r_1\alpha)K_1(r_1\alpha) \right] \left[ U_\infty - c - 2ar_2^2 I_1(r_2\alpha) K_1(r_2\alpha) \right] \qquad (23)$$

$$+ \left[ 2ar_1 r_2 I_1(r_1\alpha)K_1(r_2\alpha) \right]^2 = 0.$$

where the coefficient $a$ can be obtained in terms of $\alpha$ from (12), and $c = \omega/\alpha$.

Note that $\det(\mathbb{M})$ is a quadratic function of $c$, and therefore, one may express $\omega$ as a function of $\alpha$ explicitly. Again, the dispersion diagram is much easier to construct for the time-unstable case then for spatial instability. Recommendations about the numerical methods available to solve the dispersion relation will be presented at the end of this report.

In order to obtain the stream function $\psi(x, r, t)$ corresponding to a given $(\omega, \alpha)$ pair we first need to determine the coefficients $A$, $B$, $C$, $D$. These coefficients are the columns of the $4 \times 4$ matrix $\mathbf{M'}$ of Eq. (22) and satisfy the equation.

$$\mathbf{M'X=0}$$

The components of $\mathbf{X}$ have been obtained as the minors of $\mathbf{M'}$ belonging to its fourth row. Thus, up to an arbitrary nonzero constant of proportionality,

$$\begin{aligned}
A &= \quad 2ar_1 r_2 I_1(\alpha r_1)K_0(r_2\alpha)K_1(r_2\alpha), \\[2mm]
B &= \quad -I_0(r_1\alpha)\left\{ 2ar_1^2 I_1(r_1\alpha)K_1(r_1\alpha) + U_j - c \right\}, \\[2mm]
C &= \quad r_2\alpha K_0(r_2\alpha)K_1(r_2\alpha)B, \\[2mm]
D &= \quad r_1\alpha I_0(r_1\alpha)I_1(r_1\alpha)A.
\end{aligned} \qquad (24)$$

The stream function $\psi(r)$ can be obtained from Eqs. (15a,b,c). The functions $u(r)$, $.w(r)$ and $p(r)$ are obtained from (5), (6) and (7), respectively:

---

6      A&S, Eq. 9.6.15, p. 375

$$u(r) = \begin{cases} A\alpha I_0(\alpha r) & \text{if } 0 \le r \le r_1 \\ B\alpha I_0(\alpha r) + C\alpha K_0(\alpha r) & \text{if } r_1 \le r \le r_2 \\ D\alpha K_0(\alpha r) & \text{if } r_2 \le r < \infty \end{cases} \qquad (25)$$

$$w(r) = \begin{cases} -i\alpha A I_1(\alpha r) & \text{if } 0 \le r \le r_1 \\ -i\alpha B I_1(\alpha r) - i\alpha C K_1(\alpha r) & \text{if } r_1 \le r \le r_2 \\ -i\alpha D K_1(\alpha r) & \text{if } r_2 \le r < \infty \end{cases} \qquad (26)$$

$$p(r) = \begin{cases} -A(U_j - c)\alpha I_0(\alpha r) & \text{if } 0 \le r \le r_1 \\[2ex] \left.\begin{array}{l} B[-(ar^2 + b - c)\alpha I_0(\alpha r) + 2ar I_1(\alpha r)] \\ + C[-(ar^2 + b - c)\alpha K_0(\alpha r) + 2ar K_1(\alpha r)] \end{array}\right\} & \text{if } r_1 \le r \le r_2 \\[2ex] -D(U_\infty - c)\alpha K_0(\alpha r) & \text{if } r_2 \le r < \infty \end{cases} \qquad (27)$$

## Proposed numerical approach

Equations (23), (25), (26) and (27) define the solution of the jet flow problem. All these equations are defined in terms of the modified Bessel functions $I_0(z)$, $I_1(z)$, $K_0(z)$ and $K_1(z)$. Therefore, the first problem is the evaluation of these functions for real values of $z$ to analyze the temporal instability problem, and for complex $z$ to analyze spatial instability. These functions are pretty common; in fact, for real arguments their values are tabulated in Abramowitz and Stegun[7] The function values and the functional relations can be also easily accessed by MATHEMATICA; in fact, access is no more difficult than to the exponential function, say. The following table gives the applicable notations:

| Math. notation | MATHEMATICA |
|---|---|
| $I_n(z)$ | BesselI$(n, z)$ |
| $K_n(z)$ | BesselK$(n, z)$ |

Alternately, these functions are not hard to evaluate in FORTRAN. There is a subroutine package available at Boeing, written by Rick Whitaker, and (to my understanding) first developed at the Argonne National Laboratories in the 1970's. The relevant subroutines are ZBESI and ZBESK. Their usage is thoroughly documented by comment lines of the source code.

---

[7]    A&S, Modified Bessel Functions – Orders 0, 1 and 2 – Table 9.8, pp. 416–422.

# Numerical Solution of the Dispersion Equation

## Newton's method

The application is straightforward: For the solution of $\tilde{\Delta}(\omega, \alpha) = 0$ for a fixed value of $\omega = \omega_0$, we set up the recursion

$$\alpha_{n+1} = \alpha_n - \frac{\tilde{\Delta}(\alpha_n, \omega_0)}{\tilde{\Delta}_\alpha(\alpha_n, \omega_0)} \, .$$

The partial derivative in the denominator is a simple, but many-term expression constructed of the values of the modified Bessel functions $I_n(z)$, $K_n(z)$, $(n = 0, 1)$ and is anyway needed. Newton's method will work well, if a good initial guess is available.

Other iterative algorithms, such as **Muller's method,** are also available. The latter uses a quadratic extrapolation scheme based on three initial points, rather than the linear extrapolation of Newton's method from a single initial point. The convergence of Muller's algorithm is somewhat slower than that of Newton's. The advantage of Muller's method is that it does not require evaluation of derivatives.

## Method based on Gaster's Theorem

In many cases, the dispersion equation is easier to solve for $\omega$ than for $\alpha$. As a result, it is easier to find the complex values of $\omega$ for given real $\alpha$ than the complex solutions for $\alpha$ if the real $\omega$ is specified. Consequently, the temporal instability problem may be easier to solve numerically than the spatial one. This is indeed the case for the dispersion equation (23), quadratic in terms of $\omega$. Thus, $\omega = \Omega(\alpha)$ can be obtained by application of the quadratic solution formula.

Gaster's theorem[8] allows the approximate evaluation of the complex valued function $\alpha = A(\omega)$ if $\Omega(\alpha)$ is known for real $\alpha$, provided that $\omega$ and $\alpha$ are both small and $\partial(\Im\alpha)/\partial\omega$ is small for real $\omega$, conditions which may be valid near neutral stability. Thus, if the circumstances are right, the spatial instability function $\alpha_S = A_S(\omega_S)$ ($\omega_S$ real) can be obtained from the function $\omega_T = \Omega(\alpha_T)$ describing temporally unstable modes ($\alpha$ real) by the relationships

$$\left.\begin{array}{rcl} \alpha'_S &\approx& \alpha'_T \\[2em] \alpha''_S &\approx& -\dfrac{\omega''_T}{\left(\frac{\partial\omega'}{\partial\alpha'}\right)_T} \end{array}\right\} \tag{28}$$

---

[8]    M. Gaster: A note on the relationship between temporally increasing and spatially increasing disturbances in hydrodynamic stability. JFM Vol. 14, pp. 222–224. (1962)

where single primes $(')$ denote real and double primes $('')$ imaginary parts. Note that $\alpha_T' = \alpha$, hence

$$\left(\frac{\partial \omega'}{\partial \alpha'}\right)_T = \frac{\partial \omega'}{\partial \alpha} = \mathfrak{Re}\left(\frac{d\omega}{d\alpha}\right)_T.$$

The latter expression can be evaluated with reasonable effort. From (24) by implicit differentiation

$$\widetilde{\Delta}_\alpha(\omega, \alpha) + \widetilde{\Delta}_\omega(\omega, \alpha)\frac{d\omega}{d\alpha} = 0$$

or

$$\left(\frac{\partial \omega'}{\partial \alpha'}\right)_T = -\mathfrak{Re}\left\{\frac{\widetilde{\Delta}_\alpha(\omega, \alpha)}{\widetilde{\Delta}_\omega(\omega, \alpha)}\right\}_T. \tag{29}$$

Here, the denominator is easy to find, and the numerator is a simple but a many-term expression constructed of the modified Bessel function values anyway needed.

Discussion. The method outlined gives only an approximation valid in the vicinity of $\alpha = 0$. Its result has to be refined by some other method, such as Newton's. In other words, the result can serve as the initial guess for an iterative method, and therefore it is probably not our method of choice.

**Tracing $\alpha = A(\omega)$ in the complex $\alpha$-plane.** Analogously to (29), we may derive a differential equation for $\alpha = A(\omega)$:

$$\frac{d\alpha}{d\omega} = -\frac{\widetilde{\Delta}_\omega(\omega, \alpha)}{\widetilde{\Delta}_\alpha(\omega, \alpha)}, \tag{30}$$

where $\omega$ is a real variable, but $\alpha$ is complex. Thus, we have the system of real, coupled differential equations

$$\left.\begin{aligned}
\frac{d\alpha'}{d\omega} &= -\mathfrak{Re}\left\{\frac{\widetilde{\Delta}_\omega(\alpha', \alpha'', \omega)}{\widetilde{\Delta}_\alpha(\alpha', \alpha'', \omega)}\right\} \\[2mm]
\frac{d\alpha''}{d\omega} &= -\mathfrak{Im}\left\{\frac{\widetilde{\Delta}_\omega(\alpha', \alpha'', \omega)}{\widetilde{\Delta}_\alpha(\alpha', \alpha'', \omega)}\right\}
\end{aligned}\right\} \tag{30'}$$

with the real unknowns $\alpha'$, $\alpha''$. The system (30) can be solved numerically with a Runge-Kutta method or any predictor-corrector method such as the Adams-Moulton or Milne-Thompson method. Excellent programs are available as canned programs in packages such as the IMSL routines. This method has been tested before by the author in the solution of the dispersion equation stemming from another problem. The method depends on the knowledge of an initial solution $\{\omega_0, \alpha_0\}$.

90

## Rectangle bisection method.

      This method, developed by the author and tested on dispersion relations from other fluid flow problems, is based on the connection between the winding number and the number of zeros of a function analytic in the closure of an open domain $\mathcal{D}$ with a smooth boundary in the complex plane. If $f(z)$ is analytic in the closure of $\mathcal{D}$ and the winding number of the map of the boundary of $\mathcal{D}$ by $f(z)$ is $\nu$, then $f(z)$ has $\nu$ zeros in $\mathcal{D}$. (Argument principle)

      Here only a sketch of the method can be given. The argument principle is applied to a rectangular domain $\mathcal{R}$ of the $\alpha$-plane which does not contain any singularity or branch cut of the function $\tilde{\Delta}(\omega_0, \alpha)$. Suppose that by the argument principle it is determined that $\mathcal{R}$ contains a positive number of zeros of $\tilde{\Delta}(\omega_0, \alpha)$. Then, $\mathcal{R}$ is divided by a horizontal (or vertical) center line into the rectangles $\mathcal{R}_1$ and $\mathcal{R}_2$. Apply the argument principle to $\mathcal{R}_1$ and $\mathcal{R}_2$. If the function values of $f$ on the boundary of $\mathcal{R}$ are saved, we need to determine only the function values on the center line segment used in the sepration of $\mathcal{R}_1$ and $\mathcal{R}_2$. The distribution of the sampling points for the evaluation of $f$ is optimized by an adaptive method. Roughly, the step size of function evaluations is halved and doubled if the argument variation gets too large and too small, respectively. If the rectangle $\mathcal{R}_1$ contains a positive number of zeros we save the coordinates of $\mathcal{R}_1$ and the number of zeros it contains, otherwise we discard the information. The rectangle $\mathcal{R}_2$ is treated the same way. Now the algorithm is repeated on each of the remaining rectangles involving bisection of the rectangles, finding numbers of zeros contained in the new rectangles, and discarding any empties. The direction of the bisection is, in general, alternating between horizontal and vertical. We continue the iteration until the rectangle diagonals are smaller than a specified error tolerance. (See Fig. 1).

      The method has been coded by the author and applied to several unrelated problems   The method is always convergent and convergence is surprisingly fast (though, of course not comparable to the speed of convergence of Newton's algorithm, *if* it converges). The speed of convergence depends on the time required for a single function evaluation. Roughly, each new "generation" of rectangles requires 4 to 10 function evaluations and the number of generations can be obtained from the error formula

$$E = \frac{d_0}{2^{n/2}}$$

where $d_0$ is the initial rectangle size and $n$ is the number of generations.

      <u>Discussion.</u> It was found in the planar case that if $\alpha$ is plotted in the complex $\alpha$-plane and the real $\omega$ is a parameter, the resulting dispersion diagram has infinitely many branches starting from points $\alpha_k^0$ corresponding to $\omega = 0$. It was found that $\alpha_0 = 0$, but

91

$\mathfrak{Re}[\alpha_k] \to -\infty$ [9] and $\mathfrak{Im}[\alpha_k] \to \infty$ as $k \to \infty$. (See Fig. 2) Clearly, Gaster's theorem cannot be used to find initial points on the higher branches. On each branch, a starting point is needed. This can be obtained by a "lucky guess", or a few steps of the rectangle bisection method. Whichever method we used to find an initial guess, it must be followed by refinement by Newton's method, or some other similar iterative algorithm.

---

[9]    The calculation was based on the dispersion relation

$$\omega^2 = (1 - 2\alpha)^2 - e^{-4\alpha}$$

of Drazin and Reid. They base this on the assumption that $U_\infty = +1$ and $U_{-\infty} = -1$, hence, $U_\infty > U_{-\infty}$. In our present model the opposite is the case. This accounts for the sign difference of $\mathfrak{Re}[\alpha]$
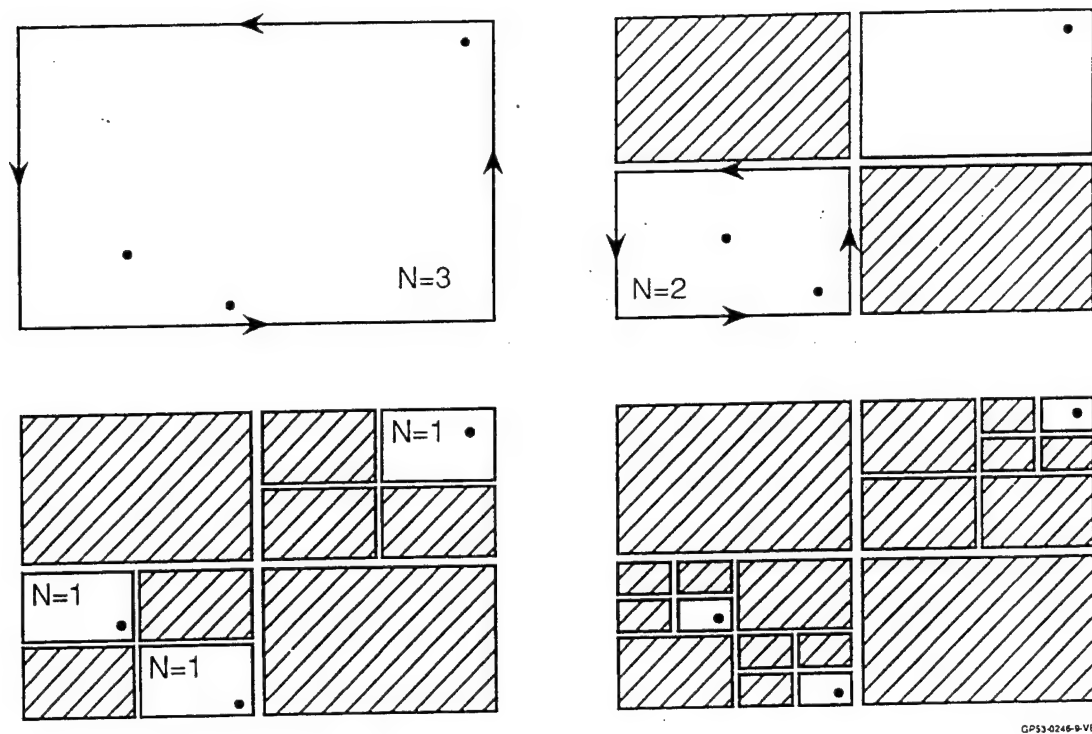
**Figure D-1.** Numerical solution of the dispersion equation $\chi(\alpha) = 0$.
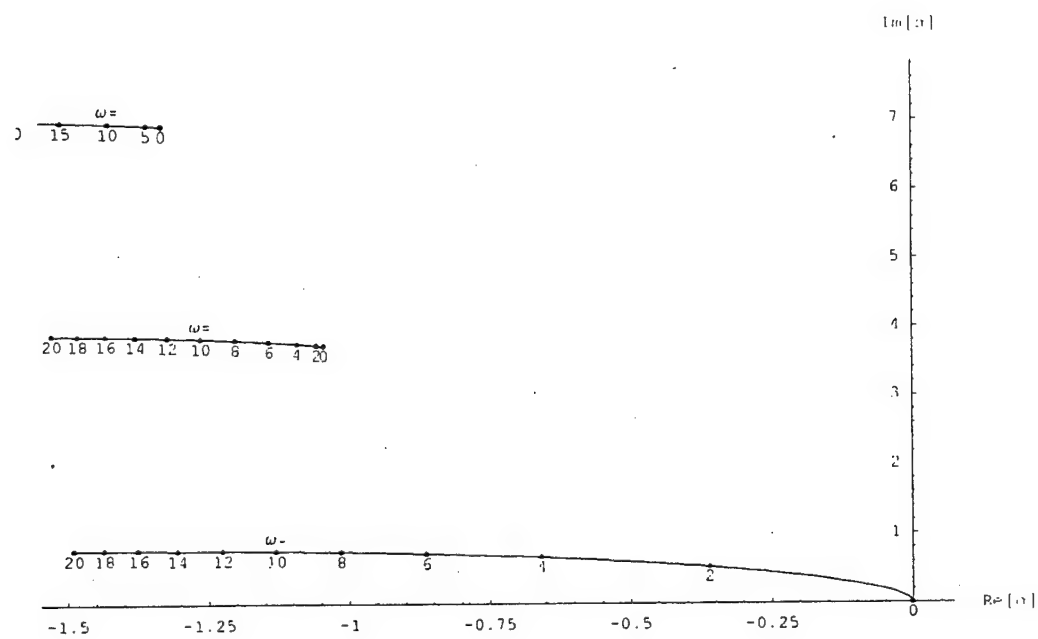


**Figure D-2.** Dispersion diagram of Drazin-Reid parallel jet.

# Appendix E

## Evolution Strategies for Parameter Optimization in Jet Flow Control

**P. Koumoutsakos, J. B. Freund, and D. E. Parekh**

# Evolution strategies for parameter optimization in jet flow control

## By P. Koumoutsakos, J. Freund[1] AND D. Parekh[2]

We present results from the application of evolution strategies for parameter optimization in direct numerical simulations and vortex models of controlled jet flows. It is shown that evolution strategies are a portable, highly parallel method that can complement our physical intuition in the parameter optimization of such flows.

## 1. Introduction

For centuries engineers have taken inspiration from nature in designing efficient aerodynamic configurations. It is no coincidence that the shape of an aircraft's wing resembles a bird's. We wish to approach the problem of flow control, not from the perspective of imitating existing natural forms, but from the perspective of developing efficient control algorithms, by employing techniques inspired by biological processes. These techniques, which we will refer to as "machine learning algorithms", are gaining significance in the areas of modeling and optimization for fluid dynamics problems as a technology that could help reduce cost and time to market of new designs.

### 1.1 Evolution strategies

Some of the seminal work in this field (Rechenberg 1971, Schwefel 1974, Hoffmeister 1991) actually was aimed at improving aerodynamic shapes. As stated in (Schwefel, 1974):

*"In 1963 two students at the Technical University of Berlin met and were soon collaborating on experiments which used the wind tunnel of the Institute of Flow Engineering. During the search for the optimal shape of bodies in a flow, which was then a matter of laborious intuitive experimentation, the idea was conceived of proceeding strategically. However, attempts with the coordinate and simple gradient strategies were unsuccessful. Then one of the students, Ingo Rechenberg, now professor of Bionics and Evolutionary Engineering, hit upon the idea of trying random changes in the parameters defining the shape, following the example of natural mutations. The evolution strategy was born."* (The second student was Hans Paul Schwefel).

Since this pioneering work, stochastic optimization techniques have gained recognition and popularity in several fields of engineering, but this has not been the case

1 University of California, Los Angeles

2 Georgia Institute of Technology

in the field of fluid dynamics in the last three decades. Recent work by Rechenberg (1994) focuses on the shape optimization approach with the construction and experimental testing of shapes that have been produced via evolutionary strategies using computer simulations. Evolution strategies have also been implemented in order to optimize the motions of an artificial tuna (M. Triantafyllou, private communication).

Here, we report preliminary results from the application of evolution strategies in the optimization of actuator parameters in active jet flow control and in the optimization of bifurcating and blooming jets.

### 1.2 Jet flow control

It is desirable in many circumstances to enhance mixing in the exhaust from aircraft engines. Applications include lift enhancement, signature reduction, and temperature reduction on blown flaps. This work focuses on the latter case. The blown flap on a C-17 (Fig. 1) is currently made out of titanium to avoid melting. If mixing can be significantly enhanced so that the plume temperature is reduced, the flap could be constructed from aluminum, a much less heavier and expensive alternative.
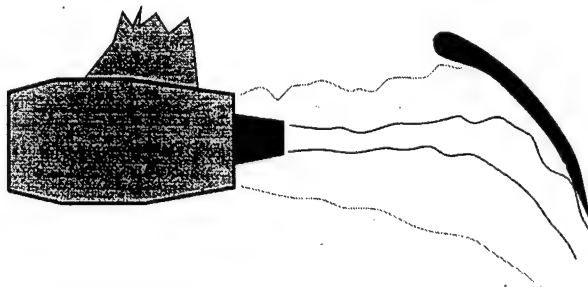
FIGURE 1. Blown flap as on a C-17.

Recently, actuators have been developed and tested on a full-scale engine which have the control authority to accomplish this objective. The goal of this work is to optimize their parameters to maximize their effectiveness. This is being undertaken as a joint experimental, numerical, and control theory effort. The discussion here is limited to the simulations and the application of evolution strategies to the problem.

### 1.3 Optimization of bifurcating and blooming jets

The proper combination of axial and helical excitation at different frequencies generates the unique class of flows known as bifurcating and blooming jets (Lee and Reynolds 1985, Parekh *et al.* 1987). The axial forcing causes the shear layer to roll up into distinct vortex rings at the forcing frequency. The helical excitation perturbs the rings radially, producing a small eccentricity in the ring alignment. This initial eccentricity is amplified by the mutual ring interactions leading to dramatic changes in jet evolution. When the axial frequency is exactly twice that of the helical excitation, the jet bifurcates into two distinct jets, with successive rings moving alternately on one of two separate trajectories. This Y-shaped jet spreads at angles

over 80 degrees, depending on forcing frequency and amplitude. The relative phase, $\phi$, between the axial and helical forcing signals determines the plane in which the jet bifurcates. When the ratio, $\beta$, of axial to helical excitation frequency is non-integer, the vortex rings scatter along a conical trajectory. When viewed from downstream, the vortex ring pattern often resembles a bouquet of flowers, hence the name"blooming jet."

In applying the evolution strategies to this class of flows, we are exploring whether the phenomena discovered experimentally could also be obtained in our simulations via an "evolutionary process" and whether new phenomena could be found. Here a vortex model describes the jet dynamics. The optimization algorithm is tuned to maximize jet spreading by varying the excitation parameters.

## 2. Evolution strategies for optimization

We discuss first the formulation of evolution strategies for the optimization of N-dimensional functions:

$$F(\mathbf{x}) = F(x_1, x_2, ..., x_M)$$

We define a vector in the parameter space as an *individual*. The whole discrete parameter space can then be considered as a *population* of individuals. Evolution strategies try to identify the *best* individual from this population based on the *fitness value*, prescribed by the function $F$. The optimization proceeds by following to a certain extent models of biological evolution.

### 2.1 Two membered evolution strategies

The simplest (and earliest) form of evolution strategies is based on populations that consist of two competing individuals ( *"a two-membered strategy"*). The evolution process consists of the two operations that Darwin (1859) considered as the most important in natural evolution: *mutation* and *selection*. Each individual (i.e. vector in the parameter space) is represented using a pair of floating point valued vectors:

$$\mathbf{u} = \mathbf{u}(\mathbf{x}, \boldsymbol{\sigma})$$

where $\boldsymbol{\sigma}$ is an M-dimensional vector of standard deviations.

Following Rechenberg (1971) and using terminology from biology, the optimization algorithm may be described as follows:

a - *Initialization:* A parent genotype consisting of M-genes is specified initially ($\mathbf{x}^0$). At each generation an individual $\mathbf{u}_p^n = (\mathbf{x}_p^n, \sigma_p^n)$ is identified.

b - *Mutation:* The parent of generation-n produces a descendant, whose genotype differs slightly from that of the parent. The operation of mutation is then realized by modifying $\mathbf{x}$ according to:

$$\mathbf{x}_c^n = \mathbf{x}_p^n + \mathcal{N}(0, \sigma_p^n) \qquad\qquad 2.1$$

where $\mathcal{N}(0, \boldsymbol{\sigma})$ denotes an M-dimensional vector of random Gaussian numbers with zero mean and standard deviations $\boldsymbol{\sigma}$.

c - *Selection:* Due to their different genotypes the two individuals of the population can have a different fitness for survival. This fitness is evaluated by the function $f$. Only the fittest of the two individuals is allowed to produce descendants at the following generation. Hence to *minimize F* we write:

$$\mathbf{x}_p^{n+1} = \begin{cases} \mathbf{x}_p^n, & \text{if } F(\mathbf{x}_p^n) \leq F(\mathbf{x}_c^n); \\ \mathbf{x}_c^n, & \text{otherwise.} \end{cases} \qquad 2.2$$

Note that in this two-membered algorithm the vector $\boldsymbol{\sigma}$ of standard deviations remains unchanged throughout the evolutionary process.

For *regular optimization problems* (see Michalewicz, 1996 for a definition) it is possible to prove the convergence of the method to a global minimum. However, this theorem does not provide a convergence rate of the method.

In this work we have implemented the *1/5 success rule* proposed by Rechenberg (1971). According to this rule: *During the optimum search the frequency of successful mutations is checked periodically by counting the ratio of the number of successes to the total number of trials. The variance is increased if this ratio is greater than 1/5 and it is decreased if it is less than 1/5.* The period over which this performance is being checked depends on the number of parameters that are being optimized. We refer to Schwefel (1995) for further details on the implementation of the two-membered evolution strategies.

### 2.2 Multi-membered evolution strategies

One of the drawbacks of the 1/5 rule for the two-membered strategy is that it may lead to premature convergence, as the step lengths can be reduced to zero, thus not improving the progress towards a global optimum. There are several possible remedies to this drawback. Of particular interest are those that can be constructed by further developing the model of evolution to resemble natural processes. In that context, a higher level of imitation of an evolutionary process can be achieved by increasing the number of members in a population. Such multi-membered strategies are usually formulated in terms of $\mu$-parents and $\lambda$-descendants. The most common strategies are then described as $(\mu, \lambda)$ and $(\mu + \lambda)$. In the $(\mu, \lambda)$ case at each generation the $\mu$-fittest individuals are selected only among the $\lambda$ children of the generation, whereas in the $(\mu+\lambda)$ case the parents are also included in the evaluation process. Schwefel (1995) presents an extensive comparison of multi-membered and two-membered evolution strategies for a series of optimization problems.

### 2.3 Handling of constraints

One of the advantages of evolution strategies is the ease and simplicity by which they can handle problem constraints. Such constraints are usually formulated as inequalities. For example in the case of $q$ constraints of the parameters $\mathbf{x}$ we require that:

$$C_j(\mathbf{x}) \geq 0 \qquad \text{for all } j = 1, ..., q$$

Descendants of a certain parent that do not satisfy the constraints are accounted as results of unsuccessful mutations. Occasionally the boundaries of the constrained
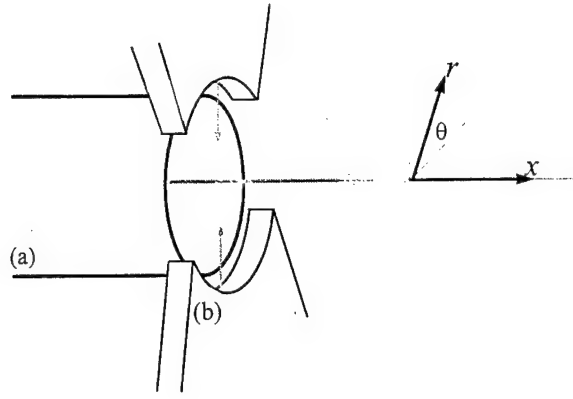
FIGURE 2.    Schematic shows the nozzle (a) and actuators (b).

regions are smoothed out in order to facilitate the convergence of the method in highly constrained problems.

## 3. Jet flow control

The compressible flow equations were solved with direct numerical simulation using a combination of sixth order compact finite differences, spectral methods, and fourth order Runge Kutta time advancement. Further details of the numerical algorithm and techniques for including actuators into the calculations were recently reported by Freund & Moin (1998). Naturally, in a direct numerical simulation we are restricted to highly simplified geometries (Fig. 2); nevertheless, the actuators were able to reproduce the effects observed in experiments by Parekh *et al.* (1996). Figure 3 shows a visualization of a jet forced into a flapping mode and an unforced jet. Clearly, the mixing is enhanced downstream.

For this preliminary study, only three types actuation parameters were varied: the amplitude, frequency, and phase. The actuation was a simple waveform sum of harmonic waveforms:

$$v_r = \sum_{i=1}^{N} A_i \left( 1 + \sin\left( \frac{USt_i}{D} t + \phi_i \right) \mathrm{sgn}(\cos(\theta)) \right), \qquad 3.1$$

where $v_r$ is the radial velocity at the actuator exit and $A_i$ are the amplitudes, $St_i$ are the Strouhal numbers, and $\phi_i$ are the phases of the different modes. The $\mathrm{sgn}(\cos(\theta))$ causes each waveform to excite a flapping mode in the jet. Note that the phases, $\phi_i$, are the relative phases of the different modes setting the two actuators always at $180^o$ out of phase. The flow rate out of either actuator was constrained to be less than $U/2$ where $U$ is the jet velocity. This was accomplished by simply "clipping" the velocities to be below this level.

The only constraint on $A_i$ was that they be non-negative. Strouhal numbers were restricted to be $0 \le St \le 0.8$ and the phases were constrained to be $\phi_i \in [0, 2\pi]$.

A very low Reynolds number ($Re = 500$) jet at Mach 0.9 was simulated in this preliminary effort to minimize the computational expense. The computational mesh
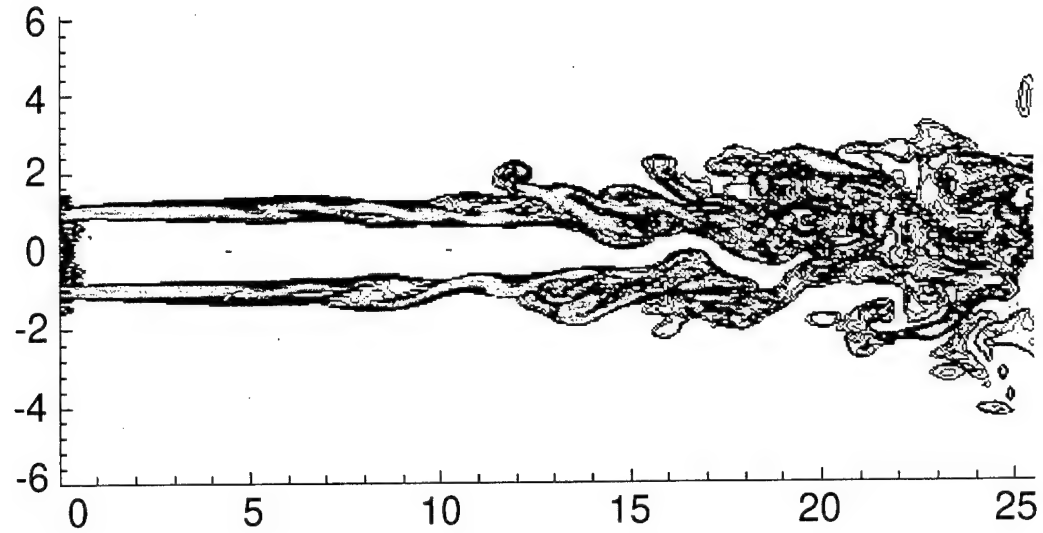
FIGURE 3A. Unforced turbulent jet. Visualization of vorticity magnitude.



FIGURE 3B. Forced turbulent jet. Visualization of vorticity magnitude.

was $112 \times 42 \times 16$ in the streamwise, radial, and axial direction respectively and the computational domain extended to 16 radii downstream and 5 radii in the radial direction. A stretched-mesh boundary zone was positioned outside of the region to cleanly absorb fluctuations convecting out of the domain. In each iteration of the evolution strategy, the jet was simulated starting from an unforced case for several periods of forcing after the passing of initial transients. Because the flow becomes quasi-periodic, this was sufficient to provide a measure of the long-time actuator effectiveness. Each iteration required approximately 10 minutes and in total 200 iterations were made (the best case was found after approximately 150 iterations).

Three wave forms ($N = 3$) where used and the initial control parameters were
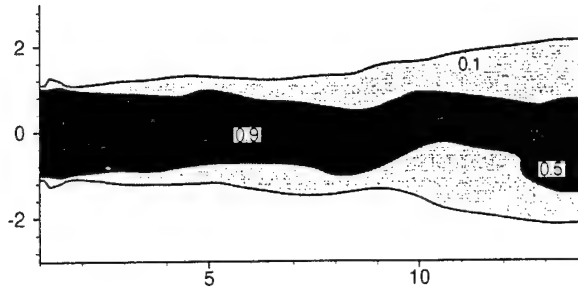
FIGURE 4A.Jet mixture fraction for the first guess parameters.
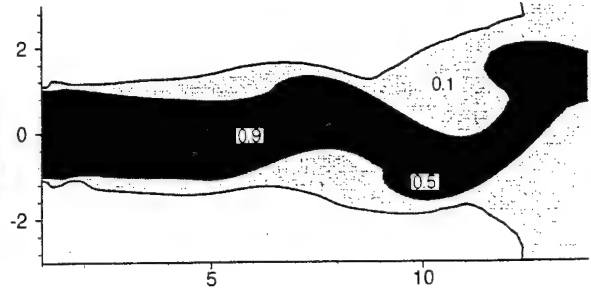
FIGURE 4B. Jet mixture fraction with the best case parameters after 200 iterations.

| $A_i/U$ | $St_i$ | $\phi_i$ |
|---------|--------|----------|
| 0.45 | 0.5 | 0.0 |
| 0.40 | 0.2 | 0.7 |
| 0.35 | 0.5 | 1.0 |

The goal set for the evolution strategy was to maximize

$$Q = \int_0^\infty \int_0^{2\pi} \int_{4r_o}^{8r_o} v_r^2 r \, dr \, d\theta \, dx.$$

This metric Q, was increased by over a factor of 10 from the initial case by the best case parameters:

| $A_i/U$ | $St_i$ | $\phi_i$ |
|---------|--------|----------|
| 0.04 | 0.33 | 0.54 |
| 0.42 | 0.17 | 0.31 |
| 0.07 | 0.45 | 1.57 |

It is interesting to note that the evolution strategy "chose" to reduce the amplitude of two of the wave modes to a very low level. Effectively, it found the same *ad hoc* scheme that was shown to be successful by Parekh *et al.* (1996) and Freund & Moin (1998). A forced and unforced case are visualized in Fig. 4. The best case clearly shows a high amplitude flapping mode which would greatly enhance mixing downstream.

## 4. Vortex model of bifurcating and blooming jets

In this work we model a circular jet by the combination of discrete vortex filaments and a semi-infinite cylindrical sheet of vorticity. The cylindrical sheet models the nozzle source flow whereas the ring filaments model the vortex rings generated by the axial excitation of the shear layer.

The semi-infinite sheet of vorticity extends from $-\infty$ to the origin. Its axis defines the jet centerline, and the end of the sheet is identified with the jet exit. The helical excitation used in the experiments of Lee and Reynolds (1985) is modeled

by rotating the axis of the vortex cylinder about the nominal jet centerline. The displacement, $A_h$, of the jet centerline from the nominal centerline corresponds to the amplitude of excitation, and $\bar{A}_h \equiv A_h/R$. The rotation frequency is given by:

$$f_h = \frac{f_a}{\mathcal{R}_f},$$ 

4.1

where the orbital frequency is defined as:

$$f_a = St_a \frac{\gamma}{D},$$

4.2

The frequency $f_a$ is the rate at which filaments are generated at the origin.

The interaction of the vortex sheet with the filaments is assumed to be such that the sheet influences the motion of the filaments but the filaments do not influence the sheet. The velocities induced by each filament and by the jet function are superimposed to determine the trajectory of each filament. The Strouhal number sets the time between creation of new ring filaments at the origin.

The circulation of each filament is identical and is determined from circulation conservation constraints. Assuming the thickness of the cylindrical sheet to be much smaller than its radius, the vorticity flux (per unit of circumference) within the sheet through any plane perpendicular to the jet's axis is given by $U^2/2$. By the assumption of a perfect fluid, the vorticity convected from the cylindrical sheet must equal the vorticity convected by the discrete filaments. This conservation relation can be expressed in terms of $\Gamma$ and $\gamma$ as

$$\frac{\Gamma}{\Delta t} = \frac{\gamma^2}{2},$$

4.3

where $\Gamma$ is the circulation of each ring filament, $\gamma$ is the circulation per unit length of the cylindrical vortex sheet, and $\Delta t$ is the time between generation of ring filaments. By Eqs. 4.8 and 4.9, one obtains

$$\gamma = St_a \frac{\Gamma}{R}.$$

4.4

Further details concerning the applicability of this model and its numerical implementation are reported in Parekh *et al.* (1988).

### 4.1 Parameter optimization using evolution strategies

The primary parameters that govern the jet evolution $St_a$, $\beta$ (frequency ratio of axial and orbital excitation), $A_a$, $A_h$, and $\phi$. The effect of the axial excitation, $A_a$, is approximated by generating distinct vortex rings at the axial forcing frequency. The sensitivity to axial forcing amplitude is not modeled. In these simulations the other four parameters are allowed to vary over the following ranges: $0 \leq A_a \leq 1$, $0.1 \leq St_a \leq 1$, $0.2 \leq \beta \leq 5$, $0 \leq \phi \leq 2\pi$. Different flow patterns can be observed with variations in $\beta$ for fixed values of the other parameters. The simulation is able

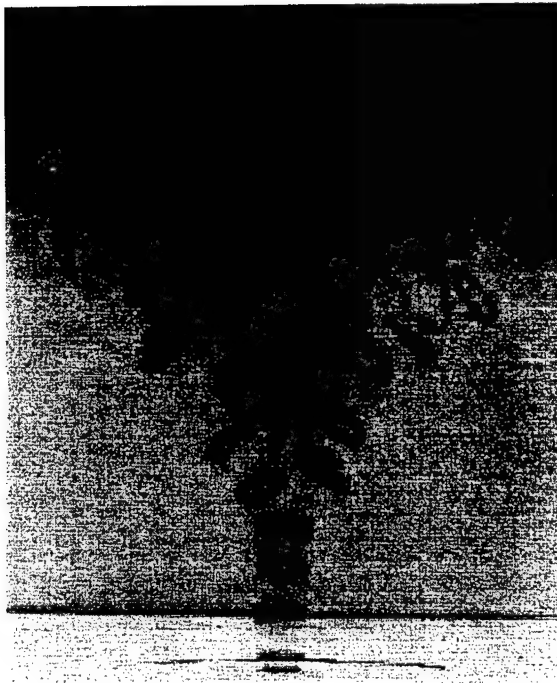FIGURE 4.1A. Blooming jets: Experimental Results of Lee and Reynolds (1985): $\beta = 1.7, A_h = 0.04, St_a = 0.46, Re = 4300$.
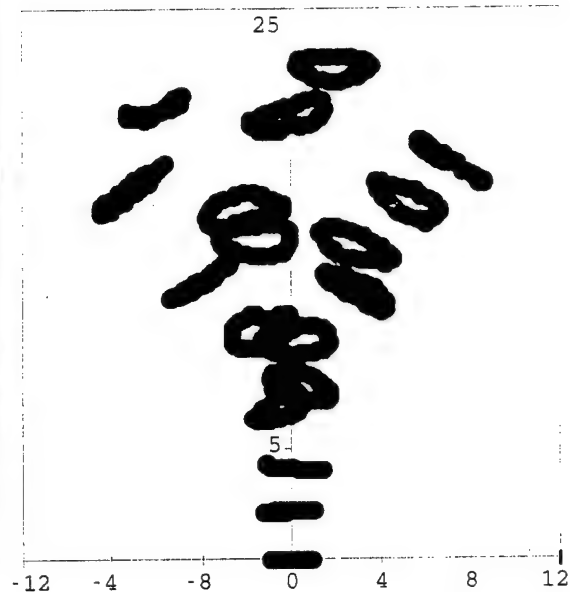
FIGURE 4.1B. Blooming Jets: Simulations $\beta = 1.7, A_h = 0.05, St_a = 0.55$.

to represent qualitatively the full range of jet phenomena observed in experiments, including bifurcating and blooming jets (Fig. 4.1).

For the optimization, several metrics for jet spreading angle were considered, including the average radial displacement of the vortex elements, jet spreading angle, and ring trajectory angles. We also considered amplitude normalized formulations of these metrics to account for the cost of excitation. The metrics were evaluated over a broad range of test cases to check if they would be robust enough to provide the proper relative rating over the parameter space considered. Some metrics are artificially biased by the initial displacement of the rings or by normalization with very small excitation amplitudes. One metric that is both simple and effective for this simulation is the average angle of the nominal ring trajectories. For each case, this metric is evaluated after the same number of periods (typically, eleven) of axial excitation. The nominal ring trajectory angle, $\theta$, is defined as the angle between the jet centerline and the line that connects the center of the jet exit to the centroid of the vortex ring nodes.

Starting with an initial guess for each of these parameters and constraints on the range of values allowable for each parameter, the genetic algorithm searches to optimize jet spreading. The scope of this work did not allow for an exhaustive investigation of the parameter space and convergence characteristics, but even these preliminary simulations yielded promising results. With all four parameters varied simultaneously, the genetic algorithm selects a blooming jet similar to what has
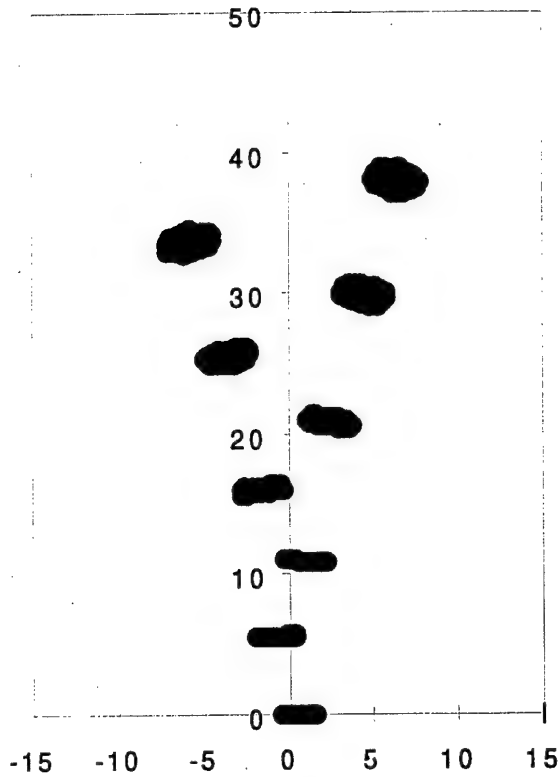
FIGURE 4.2A. Hybrid bifurcating jet with $St_a = 0.28, A_h = 0.63, \beta = 2,$ and $\phi = 0$ (side view).
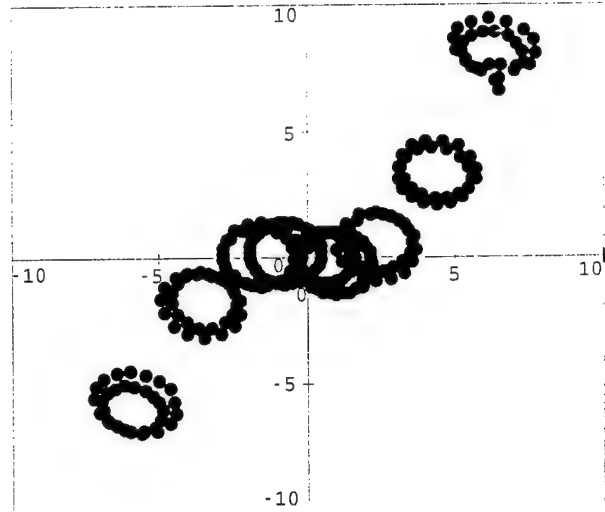
FIGURE 4.2B. End view. Each ring's 32 nodes are plotted as solid circle.

been observed in experiments.

The most striking result was found when we constrained $\beta = 2$ and kept $\phi$ fixed. Initially we expected the algorithm to select a bifurcating jet similar to Fig. 4.1A with values of $St_a$ and $A_h$ that maximize the spreading angle. Instead, a unique jet flow (Fig. 4.2) was found that had never been observed in previous experiments or calculations. This jet flow initially resembles a bifurcating jet. Several diameters downstream, however, the two branches of the jet exhibit a secondary bifurcation in which the rings change direction along a path with an azimuthal angle about $\pi/4$ different from their original trajectory. This results in a wide spreading angle as seen in Fig. 4.2B.

The simulation often has difficulty providing valid solutions for $St_a > 0.4$ since the initial ring filaments get tangled together and quickly degrade to an unrealistic state. This constraints were implemented in the evolution strategy by simply considering these cases as unsuccessful tries for the optimization algorithm.

## 5. Summary and conclusions

These preliminary results from the application of evolution strategies to the problem of flow control suggest that stochastic optimization can be a valuable tool that can complement physical understanding and deterministic optimization techniques.

As a closing remark, we quote from Schwefel:

*Since according to the "No-Free-Lunch" (NFL) theorem (Wolpert and Macready, 1996) there cannot exist any algorithm for solving all optimization problems that is on average superior to any competitor, the question of whether evolutionary algorithms are inferior/superior to any alternative approach is senseless. The NFL theorem can be corroborated in the case of EA versus many classical optimization methods insofar as the latter are more efficient in solving linear, quadratic, strongly convex, unimodal, separable, and many other problems. On the other hand, EA's do not give up so early when discontinuous, nondifferentiable, multimodal, noisy, and otherwise unconventional response surfaces are involved. Their robustness thus extends to a broader field of applications, of course with a corresponding loss of efficiency when applied to the classes of simple problems classical procedures have been specifically devised for."*

Hence, in the realm of flow control, the key issue is the identification of a suitable optimization method for the specific problem in hand. The portability, ease of parallelization, and the results reported herein and in (Müller et al. 1999), suggest that EA's present a powerful technique for parameter optimization in problems of flow control.

## REFERENCES

DARWIN, C. 1859 *The origin of species by means of natural selection.*

FREUND, J. B. & MOIN, P. 1998 *Mixing enhancement in jet exhaust using fluidic actuators: direct numerical simulations,* ASME FEDSM98-5235.

HOFFMEISTER F. & BÄCK T. 1991 Genetic algorithms and evolution strategies: Similarities and differences. Proc. of 1st International Conference on Parallel Problem Solving from Nature, Berlin. *Springer.*

LEE, M. & REYNOLDS, W. C. 1985 Bifurcating and blooming jets. *Fifth Symp. on Turbulent Shear Flows,* Ithaca, New York. 1.7–1.12.

MICHALEWICZ, Z. 1996 *Genetic Algorithms + Data Structures = Evolution Programs.* Springer-Verlag Berlin.

MÜLLER, S. MILANO, M. & KOUMOUTSAKOS, P. 1999 Evolution strategies for turbulent channel flow control using rotors. (in preparation).

PAREKH, D. E., REYNOLDS, W. C. & MUNGAL, M. G. 1987 Bifurcation of round air jets by dual-mode acoustic excitation. *AIAA 87-0164.*

PAREKH, D. E. 1988 Bifurcating jets at high Reynolds numbers. *PhD thesis.* Department of Mechanical Engineering, Stanford University.

PAREKH, D. E., KIBENS, V., GLEZER, A., WILTSE, J. M. & SMITH, D. M. 1996 Innovative jet flow control: mixing enhancement experiments. *AIAA Paper 96-0308.* 34th Aerospace Sciences Meeting and Exhibit

RECHENBERG, I. 1971 *Evolutionsstrategie - Optimierung technischer Systeme nach Prinzipien der biologischen Evolution.* Fromman-Holzboog.

RECHENBERG, I. 1994 *Evolution Strategy '94*, Frommann-Holzboog, Stuttgart.

SCHWEFEL, H. P. 1974 *Numerische Optimierung von Computer-Modellen*. Birkhäuser, Basel.

SCHWEFEL, H. P. P. E. 1995 *Evolution and Optimum Seeking*. Wiley Interscience.

WOLPERT, D. H. & MACREADY, W. G. 1996 No Free Lunch Theorem for Search. *Technical Report SFI-TR-95-02-010,*Santa Fe Institute.

# Appendix F

## Key Results from Small-Scale Engine Experiment

**D. E. Parekh**

# Appendix F

## Key Results from Small-Scale Engine Experiment

This appendix provides summary plots representative of the key results from the experimental demonstration on the small-scale engine. Figure F-1 presents the centerline temperature decay of the baseline flow at two different Mach numbers. The axial distance is normalized by the nozzle exit diameter. Figures F-2 through F-4 provide the corresponding Strouhal number dependence of centerline temperature at a fixed location of $X/D = 4$. From a feedback control standpoint, one would like to be able to average over a short time when measuring the temperature sensor data to shorten the feedback loop time. This, however, results in significant uncertainty and variability in the information being fed back to the control loop (see Figures F-3 and F-4). Consequently, a gradient search technique would be impractical to implement because of the difficulty of computing meaningful derivatives from the measured discrete data. In contrast, the genetic algorithms are able to handle this uncertainty with little difficulty.

Optimization experiments are presented in Figures F-5 through F-7 for a pair of Mach numbers and varying initial guesses. Comparison of different experiments initiated with an identical guess (Figure F-5) illustrates the variability of the convergence due to the inherent randomness in the process. Figure F-6 compares optimization when the initial guess is close to the global or local minimum. The simple approach implemented here can get trapped in a local minimum for a period of time; with more iterations, the algorithm would eventually find the global minimum. Figure F-7 provides a representative optimization experiment at a higher Mach number of 0.32.

Finally, we explore the robustness of the technique to changes in the system that are not known by the algorithm. This is simulated by varying the engine speed several times during a single optimization experiment. No information about the engine speed nor even the fact that a change occurred is monitored by the controller. Without any knowledge of the plant, the nature of the algorithm enables it inherently to adapt. While much can be done to improve the efficiency of this adaptation, Figure F-8 demonstrates the ability of even this simple algorithm to adapt to major changes in the plant. Suitability of this adaptation for real-time control in an operational mode (in contrast to real-time optimization in a test mode) would depend on the acceptability of running the actuation at random points in the parameter space during operations.
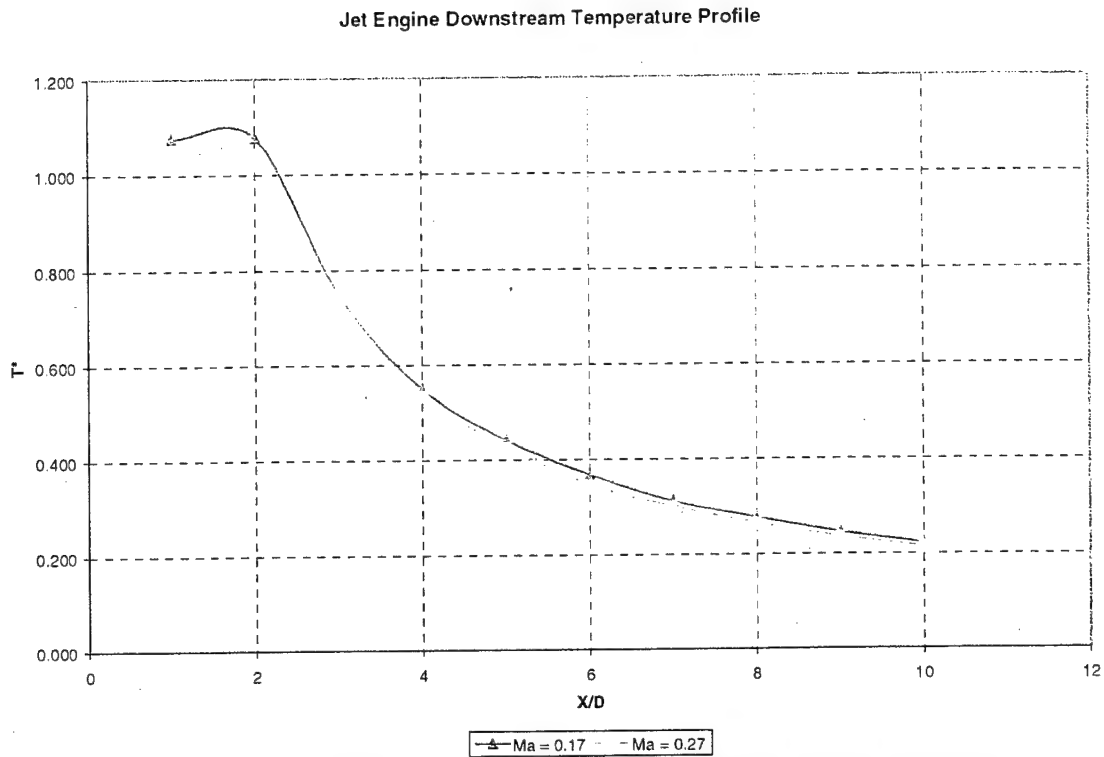
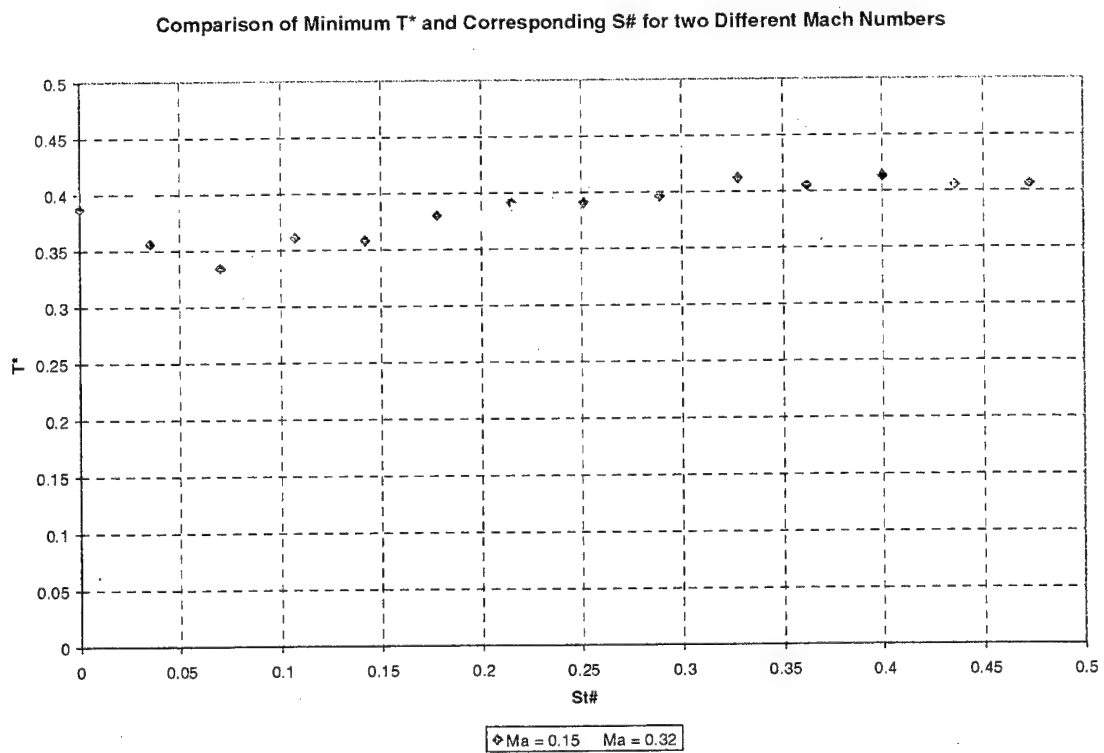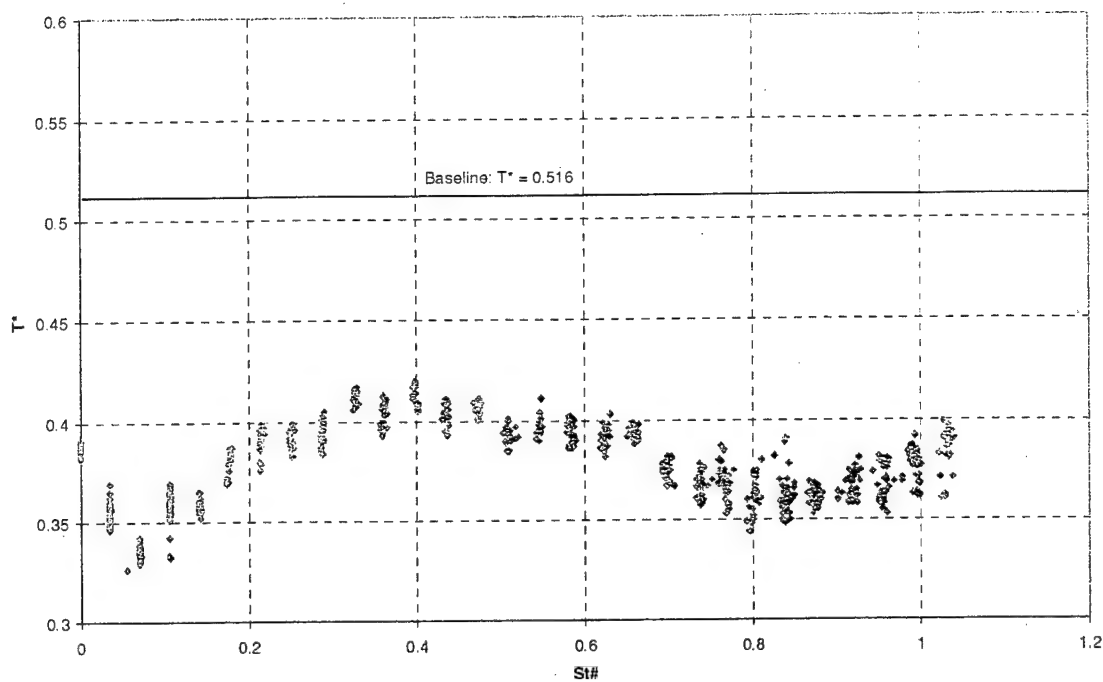**Figure F-1. Centerline temperature profile of baseline engine exhaust.**

Comparison of Minimum T* and Corresponding S# for two Different Mach Numbers



**Figure F-2. Strouhal number dependence of T\*, at X/D = 4 and for 5% mass flow injection through a single actuator.**

109

**Data Spread for Characterization of Strouhal Dependance (Ma = 0.15, 5% MFR)**

Baseline: T* = 0.516

T*

St#
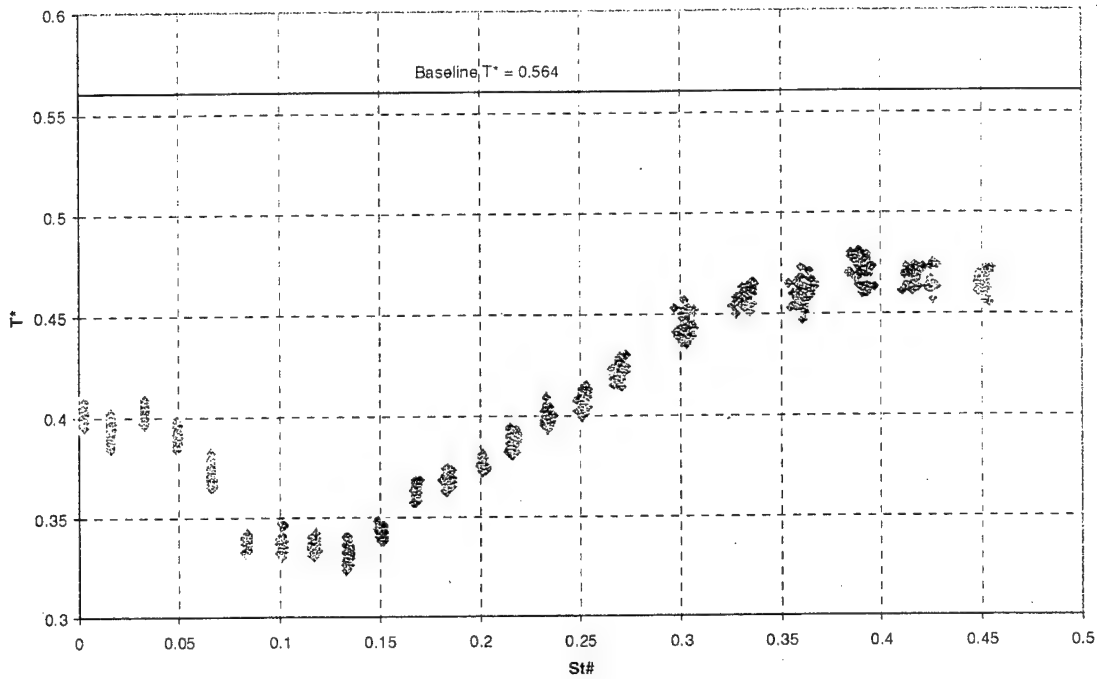
**Average T* Values for Characterization of Strouhal Dependance (Ma = 0.15, 5% MFR)**

Baseline: T* = 0.516

6th Order Polynomial Curve Fit
$R^2 = 0.905173$

T*

St#

Figure F-3. Data scatter for short-time (0.5-1s) average measurements of T* variation with temperature (upper plot) and the corresponding average profile and polynomial fit (lower plot) for M= 0.15 with 5% mass injection, measured at X/D = 4.

110
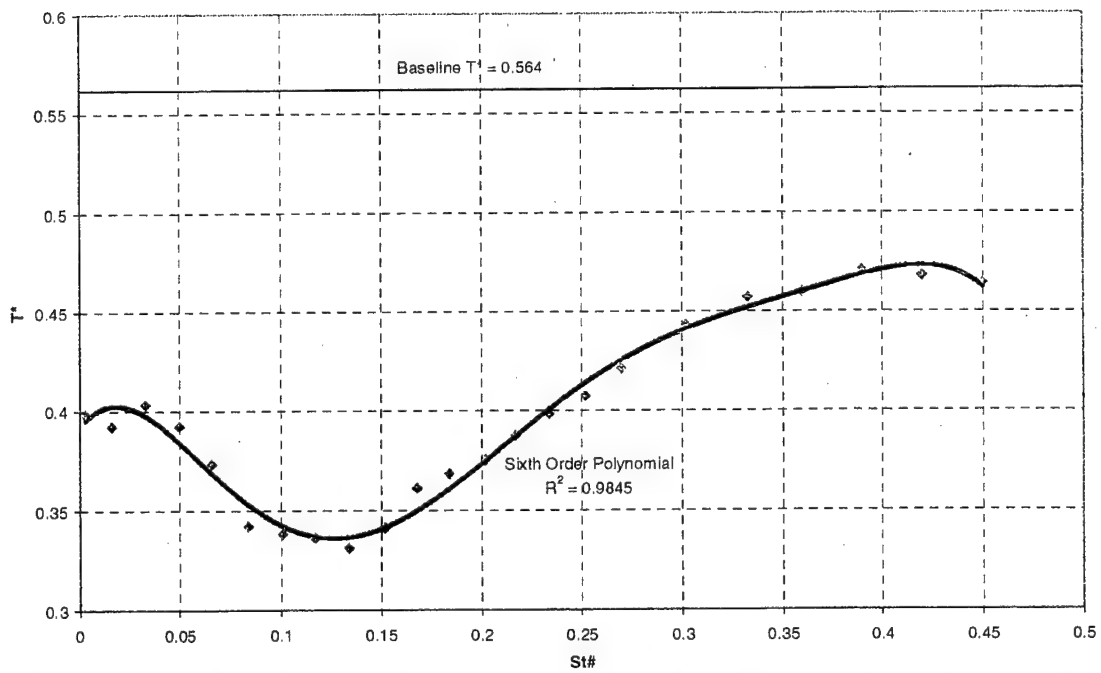
Figure F-4. Data scatter for short-time (0.5-1s) average measurements of T* variation with temperature (upper plot) and the corresponding average profile and polynomial fit (lower plot) for M= 0.32 with 5% mass injection, measured at X/D = 4.

Genetic Algorithm Convergence (Ma = 0.15, 5% MFR, 10 Generations/cycle)
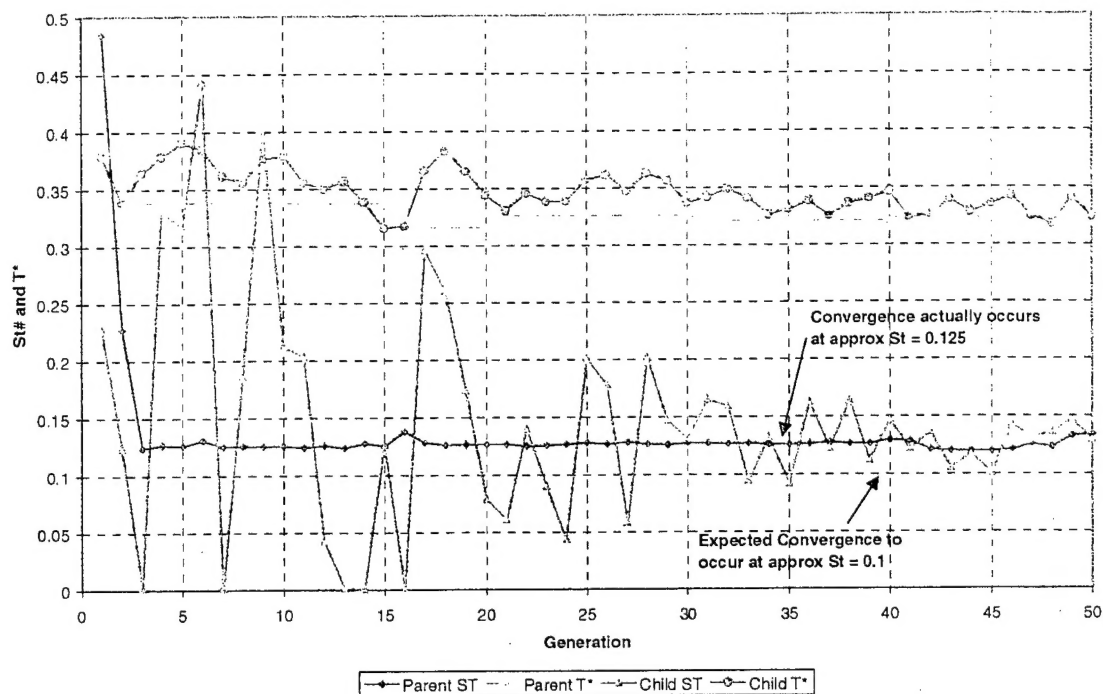


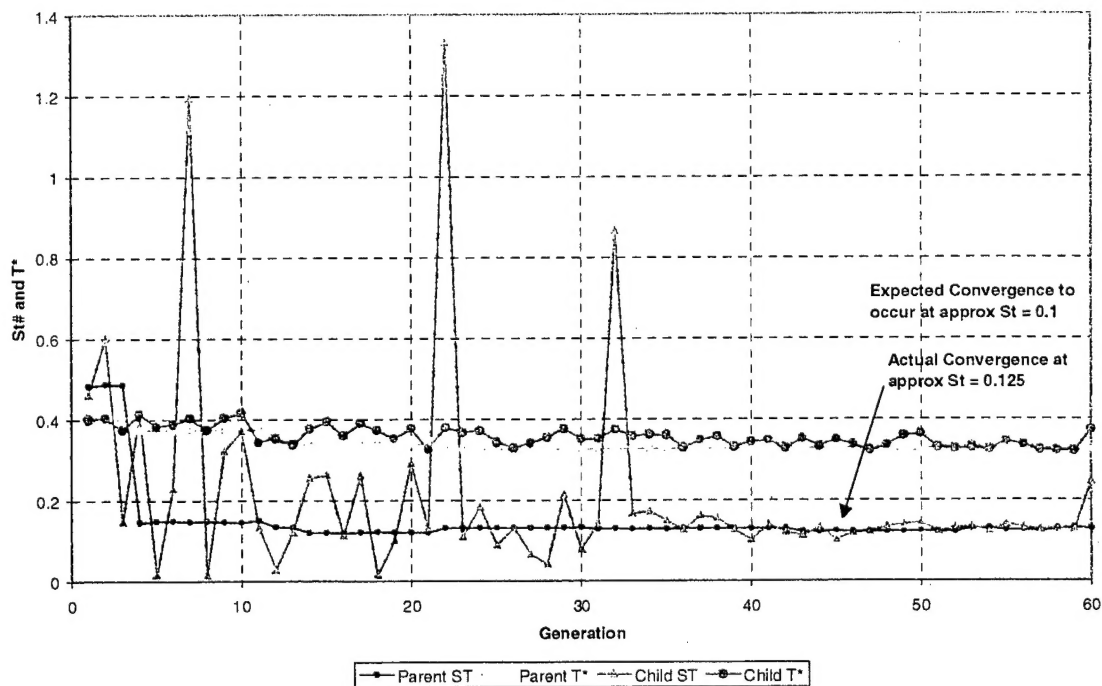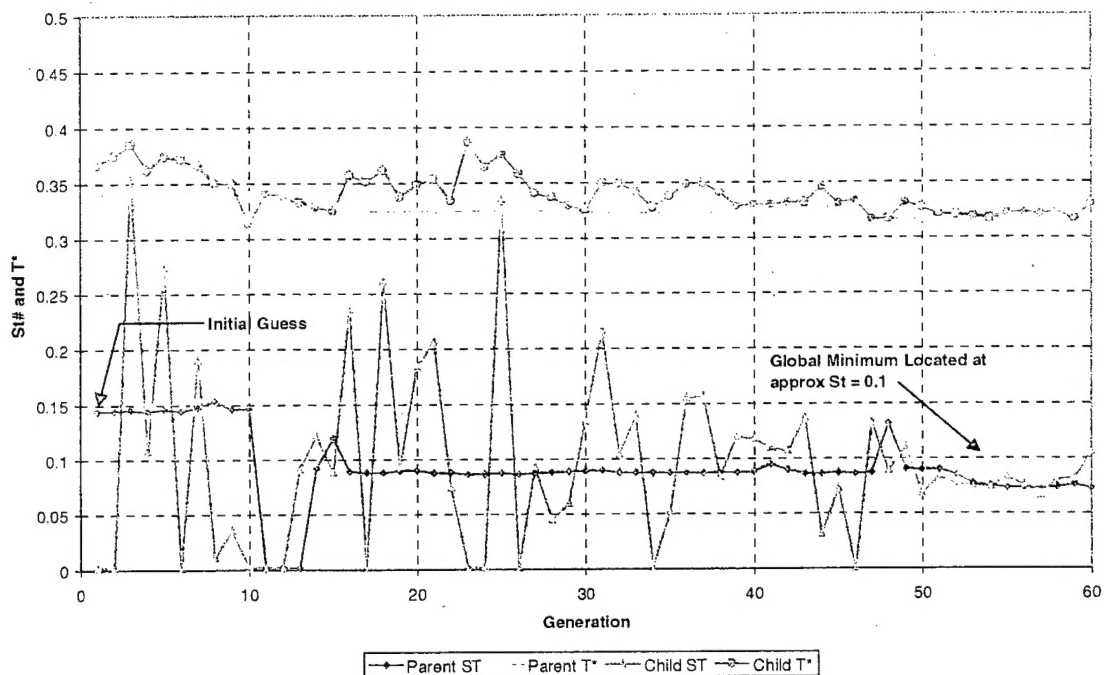Genetic Algorithm Convergence (Ma = 0.15, 5% MFR, 10 Generations/cycle)



**Figure F-5.** **Comparison of two optimization experiments run at the same conditions with the identical initial guess for Strouhal number.**

112

Genetic Algorithm Convergence when Initial Guess is close to Global Minimum
(Ma = 0.15, 5% MFR, 10 Generations/cycle)



Genetic Algorithm Convergence when Initial Guess is close to Local Minimum
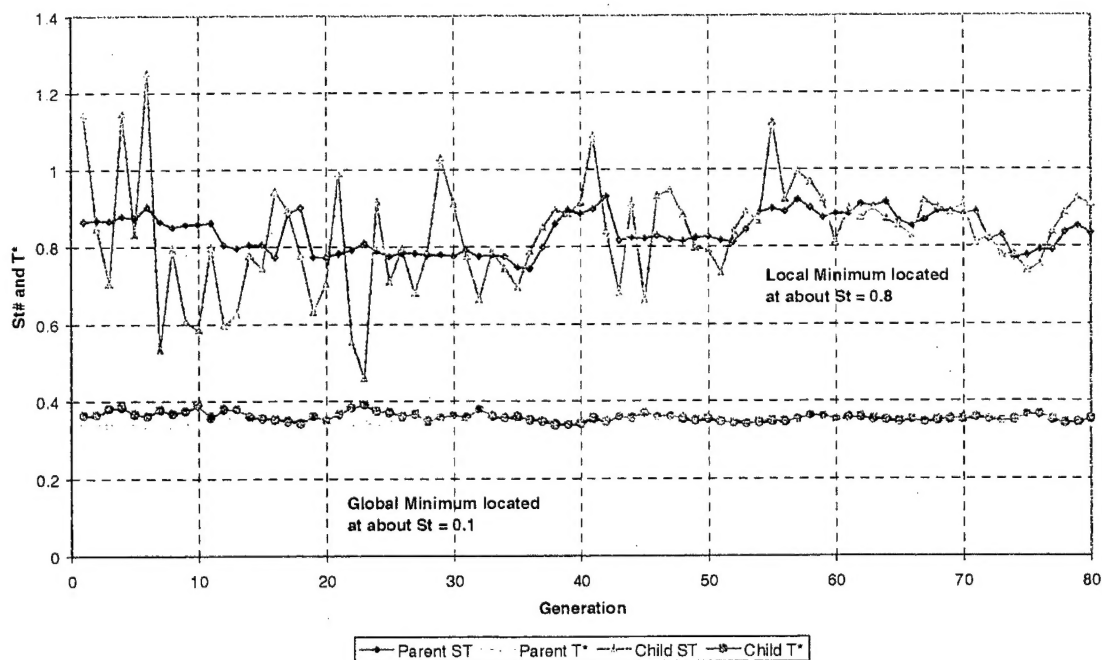(Ma = 0.15, %MFR = 5%, 10 Generations/cycle)

Figure F-6.  Comparison of optimization experiments run at the same conditions but with differing initial guesses:  close to global minimum (upper plot) and close to local minimum (lower plot).

113

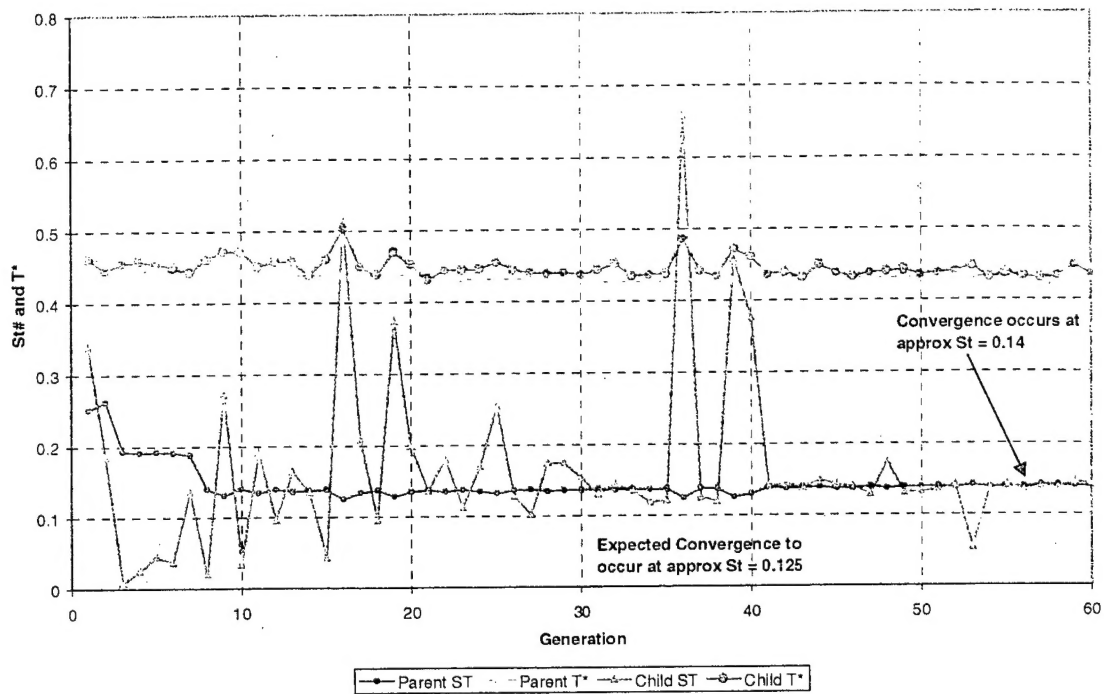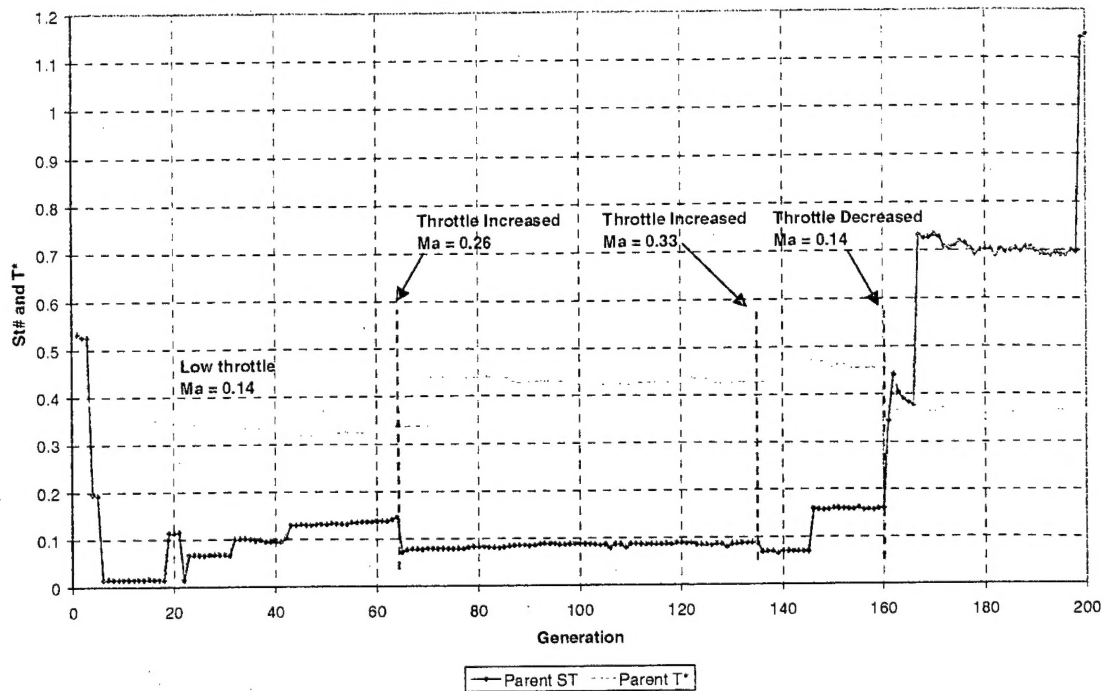Genetic Algorithm Convergence (Ma = 0.32, 2.5% MFR, 10 Generations/cycle)



Figure F-7. Example of optimization at M=0.32.

## Genetic Algorithm Convergence for Changing Engine Speeds



Parent ST · · · · Parent T*

## Genetic Algorithm Convergence for Changing Engine Speeds
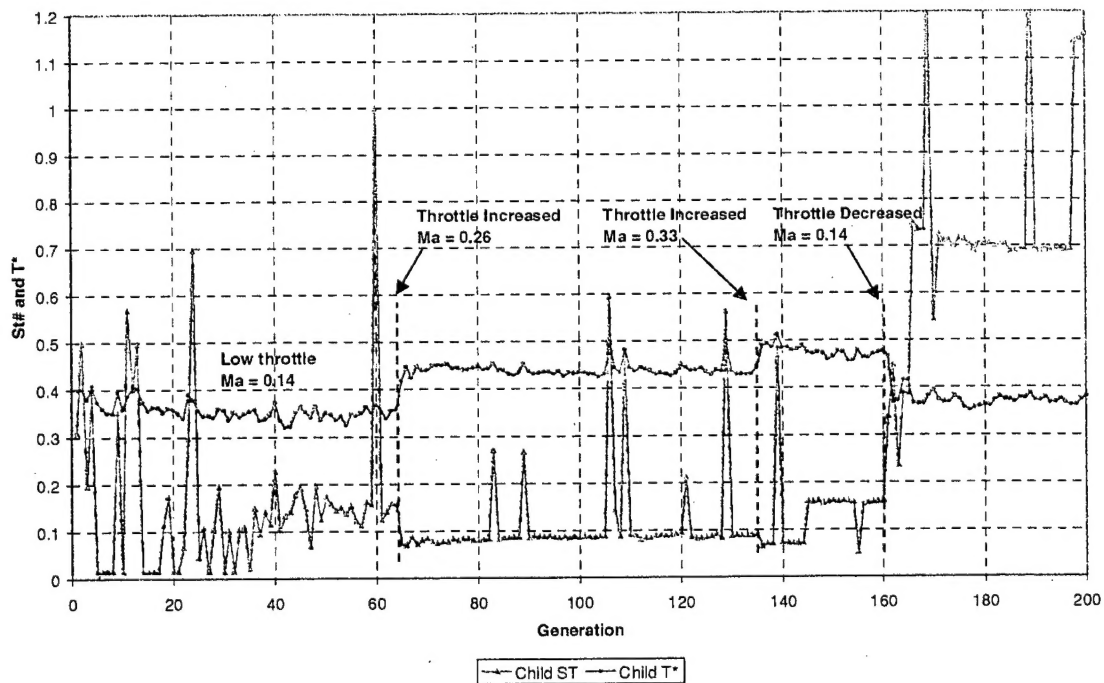


Child ST  Child T*

**Figure F-8. Optimization experiment in the presence of changing system conditions. Engine speed is varied at various points during the optimization process without any feedback to the algorithm that the engine speed has been changed.**

115